

Acknowledgements

This thesis would not have been possible without the help of my supervisor Mark Child, my partner Elaine Ewart, Christian Jungen, and the Engineering and Physical Sciences Research Council.

Particular thanks are also due to, in alphabetical order, Chris Cooper, James Davey, Helen Dickinson, Pat Dunn, Helen Fielding, Gonzalo García de Polavieja, Anne Goodgame, Miyabi Hiyama, Adam Kirrander, Dmitrii Shalashilin, Rob Smith, Tim Softley, J-P Stacey, Vas Stavros, Jan Verlet and Sarah Wilsey.

Contents

1	Introduction	5
2	Multichannel quantum defect theory	13
2.1	Bound states	17
2.2	The Beutler region	20
2.3	Measurable quantities	23
2.4	Radial matrix elements	25
3	Molecular MQDT	36
3.1	Determination of quantum defects	36
3.2	Angular momentum basis states	38
3.3	Frame transformations	43
3.4	Angular transition moments	46
3.5	Vibrational autoionization	48
3.6	Perturbations	50

4	Long-range-force model for the nf lines in Rydberg water	53
4.1	Theory	54
4.2	Fitting	62
4.3	Results and discussion	67
4.4	Conclusions	70
5	Threshold ionization spectroscopy of Rydberg water	72
5.1	Experiment	73
5.2	Theory	75
5.3	Results and discussion	79
5.4	Conclusion	82
6	Photoelectron spectroscopy of water	84
6.1	Experiment	85
6.2	Theory	86
6.3	Results	95
6.4	Discussion	99
6.5	Conclusions	104
7	Rydberg wave-packet dynamics	106
7.1	Theoretical background	108
7.2	The Ramsey method	110

7.3	Fringes and plateaux	113
7.4	The phase problem	127
7.5	Conclusion	133
8	Summary	134
9	Appendices	136
9.1	Spherical harmonics and multipoles	136
9.2	Useful expressions	137
9.3	Change of origin	141
9.4	Expectation values of r^n	143
9.5	Root finding	144
9.6	The Stark effect	145
9.6.1	Theory	145
9.6.2	Results	148
9.7	Full long-range-force model <i>nf</i> reactance matrix for water . . .	150

Chapter 1

Introduction

Low-energy spectroscopy of small molecules shows narrow rotational splittings in the microwave region (tens of cm^{-1}), wider vibration splittings in the infrared (hundreds of cm^{-1}) and much greater electronic splittings (tens of thousands of cm^{-1}) in the visible and ultraviolet. This is the observation with which Born and Oppenheimer open their classic paper [1], where they introduce the ‘clamped-nuclei’ approximation that bears their names.

Rydberg states of atoms and molecules are those where a single electron has enough energy to roam to distances where the rest of the molecule diminishes to a charged point-like object that can to some extent be treated independently. The German language uses the evocative word *Rumpf* to describe this ionic core. These apparently simple states have unusual physical properties. For example, because interactions with the core, and hence

opportunities for the electron to escape on the vibrational energy of the ion being converted to kinetic energy of the electron, become more and more infrequent and hence, unexpectedly, Rydberg states become more stable with increasing energy. The Kepler times, which as we shall see provide a good estimate of the orbital period of the electron, increase as the cube of the principal quantum number. In practice, it is found that lifetimes scale as the *fifth* power of the principal quantum number. This appears to be due to interactions with stray ions and the weak electric fields present in any experiment. High- n circular Rydberg states, where $|m| = \ell = n - 1$, of atomic hydrogen provide an almost perfect two-level system that can be used to explore cavity QED or even quantum computation [2]. A Rydberg atom in crossed electric and magnetic fields can show the same dynamics as a three-body system in celestial dynamics, where all gravitational interactions are attractive, and predict the existence of non-dispersing wave packets analogous to the stable Trojan asteroids at the Lagrange points on the orbit of Jupiter [3]. Finally, and most recently, so-called ‘trilobite’ atomic Rydberg states have been predicted in low-temperature gases [4, 5]. These are remarkable for being atoms with a permanent dipole moment, and are named after their distinctive spatial distribution.

The difference between a Rydberg and a non-Rydberg atom is obvious: Sandorfy and Lussier [6] suggest that for an atom if the principal quantum

number increases in a transition, then both the transition and the final state are Rydberg. The division is less clear for molecules. Rydberg series can be unambiguously identified in molecular spectra, but where do they begin? An effective principal quantum number can be defined for any electronic state, even the ground state (if the ionization energy is lower than the Rydberg constant), of the molecule by the Rydberg formula. The number of radial nodes n_r can always be evaluated for an atomic orbital, but not necessarily for a molecular Rydberg orbital, which is obviously non-atomic at short range. There are, indeed, orbitals that are Rydberg at the united-atom limit but not at usual molecular geometries, while other orbitals are Rydberg in both cases. Mulliken [7] compares hydrogenic atomic orbitals

$$R_{n\ell}^{\text{H}} = \left(\sum_{k=\ell}^{n-1} c_k r^k \right) e^{-\zeta r} \quad (1.1)$$

where the c_k can be obtained by expanding the relevant Coulomb function, with $n_r = n - \ell - 1$ radial nodes and $n - \ell$ loops in $R_{n\ell}$ with an approximate Slater-type form for core atomic orbitals:

$$R_{n\ell}^{\text{Slater}} \simeq \sum_{k=\ell}^{n-1} c_k r^k e^{-\zeta_k r}, \quad (1.2)$$

where $\zeta_k = (Z - s_k)/n$ (s_k is the screening term), and suggests this form

$$R_{n\ell}^{\text{Ry}} \simeq \sum_{k=\ell}^{n_c-1} c_k r^k e^{-\zeta_k r} + \left(\sum_{k=n_c}^{n-1} c_k r^{k-\mu} \right) e^{-\zeta_{\text{Ry}} r}, \quad (1.3)$$

where $\zeta_{\text{Ry}} = Z_c/(n - \mu)$, where Z_c is the charge on the core and n_c is the highest value of n for a core atomic orbital of the same ℓ as the Rydberg orbital. The 6s orbital of potassium, for instance, consists of 1s-, 2s- and 3s-like core loops, and 4s–6s hydrogenic loops. The 1s–3s core orbitals are *real precursors*, whereas the 4s and 5s orbitals, which are unoccupied in the ground state, are *virtual precursors*. By contrast the 6f orbital has no real precursors, little core character to its wavefunction, and is said to be non-penetrating. Its behaviour will be dominated by the long-range properties of the core. In a 1976 paper [8], Mulliken puts forward the following requirements of a molecular Rydberg state:

(i) That it has a stable equilibrium geometry, near which the potential surface is similar to that of the corresponding ion. We can then define a quantum-defect function parameterizing the difference between the Rydberg surface and that of the ion.

(ii) Rydbergization of the Rydberg MO near equilibrium geometries is nearly complete.

Finally, a practical definition of a Rydberg state might be that it is one

ill-modelled by conventional quantum chemical means on account of its spatial extent. High-quality *ab initio* calculations on Rydberg systems generally use special diffuse basis sets devised by Dunning [9]. The prohibitively large active spaces required restrict these calculations to low Rydberg states. However, the scaling properties of multichannel quantum-defect theory (MQDT) allow the results to be generalized throughout the spectrum, often with remarkable success.

The Born–Oppenheimer situation described above matches Hund’s coupling case (b) [10], where the electron orbital angular momentum ℓ is coupled to the molecular frame. Here the good quantum numbers for a diatomic molecule are J , the total angular momentum, ℓ and λ , the body-fixed projection of ℓ . For high Rydberg states the electronic spacing diminishes as n^{-3} and ℓ uncouples from the molecular frame. The system becomes more nearly diagonal in the core angular momentum N^+ (in some older work this is R , for *Rumpf*). This Hund’s case (d) situation, also known as pure precession, only holds exactly where all quantum defects are equal and the electronic wavefunctions are therefore in phase.¹

Chapter 2 introduces the theoretical background that will be needed. Hartree and Hargreaves in the late 1920s [11–15] showed how Eddington and

¹This is inhibited where two of the quantum defects differ by a half integer, and the wavefunctions are in antiphase, as we shall see later.

Nagaoka's treatment of the hydrogen atom could be generalized to alkali metal atoms. Then, at UCL, Bates and Damgaard [16] used a so-called Coulomb approximation to calculate oscillator strengths in atoms. In the 1960s Mulliken, in a series of three papers [7, 17, 18], described diatomic molecular Rydberg states, some of which is mentioned above. At the same time, Seaton [19] applied Ham's quantum-defect method (which had been originally developed to treat atoms in condensed phases) to free atoms, a treatment which Fano used for the hydrogen molecule in 1970 [20]. Since then (MQDT) has been adapted for Stark fields by Harmin [21–23] and Sakimoto [24, 25] and Zeeman fields by Monteiro and Taylor [26, 27] and applied to dissociative recombination and the competition between predissociation and ionization by Suzor-Weiner, Jungen and collaborators [28–31]. This thesis will use Child and Jungen's extension of MQDT to the asymmetric top [32], which is detailed in Chapter 3 along with the MQDT treatment of vibrational interactions [33, 34].

Having introduced the theoretical machinery, we then use it to explore recent experiments. Molecular Rydberg state studies have been revolutionized by the development of the laser and the molecular beam. Before the 1960s, only fragmentary Rydberg series had been detected in molecular absorption spectra, whereas now zero-electron-kinetic energy (ZEKE) spectroscopy and its ionic counterpart mass-analysed threshold ionization (MATI), which probe

the high Rydberg states close to threshold, are used almost routinely to determine ionization thresholds for molecules, for example by Müller-Dethlefs and co-workers, who have been using it extensively to explore conformations of organic molecules and clusters [35]. A combination of a molecular beam at 15 K or lower with tunable monochromatic radiation enables individual rotational states of Rydberg systems at low n to be efficiently selected, where at room temperature the spectrum would be impossibly congested. This state selection allows resonance-enhanced multiphoton ionization (REMPI), where the above states are used as intermediates. This again simplifies the Rydberg spectrum. Further, the vacuum and extreme ultraviolet areas of the spectrum become easily accessible using only visible-light lasers, without the need for synchrotron radiation. Finally, the different selection rules for multiphoton processes allow the measurement of previously dark molecular states.

In Chapter 4, we derive a long-range-force model (LRFM) for the asymmetric top and apply it to the nf multiphoton autoionization spectra of H_2O reported by Child and Glab [36]. First used for the early Rydberg spectra of NO in 1968 by Jungen and Miescher [37], this accounts for the behaviour of non-penetrating orbitals in terms of their interactions with the multipole moments and polarizabilities of the core. We then, in Chapters 5 and 6, apply it to the MATI experiments of the Softley group [38] and to the unpublished

PES measurements of Glab, again on H₂O.

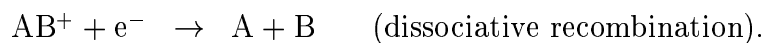
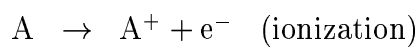
The transition from case (b) to case (d) dynamics mentioned above is not necessarily smooth. If, in the classical picture, the ionic core is in the same position relative to the electron on each encounter, then BO conditions and BO dynamics are, to some extent, restored. This is not unlike the phenomenon of a lathe or other piece of dangerous fast-moving machinery appearing stationary under a fluorescent light, and is known as the stroboscopic effect. Quantum mechanically this system corresponds to a degeneracy between electronic and rotational spacings in a Rydberg spectrum, and in more complicated cases, such as the asymmetric top, the simple classical picture is less relevant. Such a degeneracy is seen in the Rydberg spectra of nitric oxide, and has consequences for the for the molecular Rydberg wave-packet experiments of the Fielding group [39]. We develop a tentative explanation of the observed patterns in Chapter 7.

Chapter 2

Multichannel quantum defect theory

Multichannel quantum defect theory (MQDT) is a useful method for modelling rearrangement processes in atomic and molecular systems near threshold.

Examples include:



Each of the combinations $A^+ + e^-$, $A + B$ and AB is a channel; indeed each combination of allowed rotational state and angular momentum state of the

electron is a separate channel.

MQDT is applicable to both closed channels, which represent bound states of the system, and open channels, which are continua. Fig. 2.1 illustrates the “ladders” of bound states below the ionization thresholds, which are marked with dotted lines. (a) is an interaction between closed channels, (b) an interaction between a closed and an open channel, such as ionization or dissociation, and (c) is an interaction between open channels, or *bremstrahlung*. For the following notes, Greek letters denote short-range channels and Roman letters denote long-range channels. Script letters (\mathcal{K} , \mathcal{U}) mark quantities with a smooth dependence on energy and italic or bold letters ($K_{ij}(E)$, $D_i^{(-)}(E)$) those which contain poles at resonances.

Coulomb functions are solutions to the Coulomb wave equation

$$\frac{d^2\psi}{dr^2} + \left[\epsilon - \frac{V}{r} - \frac{\ell(\ell+1)}{2r^2} \right] \psi = 0, \quad (2.1)$$

where $-\infty < V < \infty$ and ℓ is a non-negative integer. The general solution is a linear combination of the regular [$f(r \rightarrow 0) \rightarrow 0$] Coulomb function $f(r)$ and its irregular [$g(r \rightarrow 0) \nrightarrow 0$] counterpart $g(r)$. A whole page of Abramowitz and Stegun [40] is devoted to the definition alone of these functions, which they call F_L and G_L . MQDT avoids this for the most part by dealing only with their asymptotic forms as $r \rightarrow \infty$. It is convenient

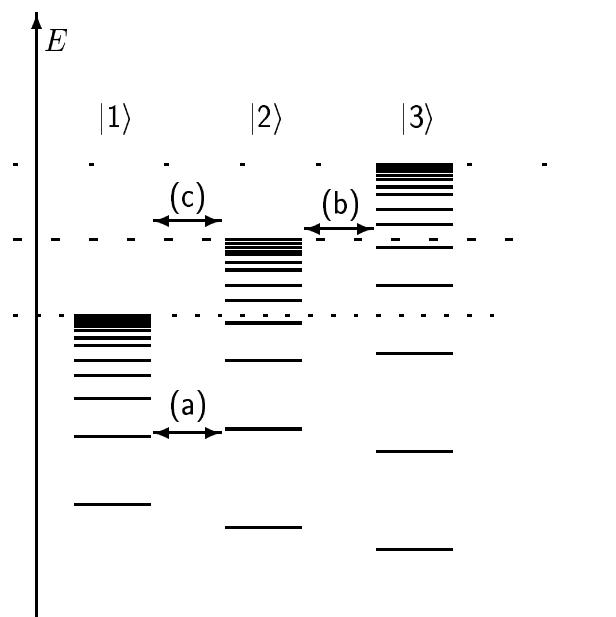


Figure 2.1: Illustration of closed and open channels. Dotted lines mark ionization thresholds. (a) interaction between closed channels (b) interaction between a closed and an open channel, for example ionization or dissociation, and (c) interaction between open channels, or *bremstrahlung*.

for programming to use a real reactance matrix \mathbf{K} instead of a complex scattering matrix \mathbf{S} . We need, therefore, a pair of Coulomb functions s and c that are sine-like and cosine-like at large r .

$$s(\epsilon, r) \xrightarrow[\epsilon > 0]{r \rightarrow \infty} \sqrt{2m/\pi k} \sin(kr + zmk^{-1} \ln r + \vartheta), \quad (2.2)$$

$$\xrightarrow[\epsilon < 0]{r \rightarrow \infty} \sqrt{m/\pi \kappa} (C^+ \sin \beta - C^- \cos \beta) \quad (2.3)$$

$$c(\epsilon, r) \xrightarrow[\epsilon > 0]{r \rightarrow \infty} -\sqrt{2m/\pi k} \cos(kr + zmk^{-1} \ln r + \vartheta), \quad (2.4)$$

$$\xrightarrow[\epsilon < 0]{r \rightarrow \infty} -\sqrt{m/\pi \kappa} (C^+ \cos \beta - C^- \sin \beta). \quad (2.5)$$

$g(\epsilon, r)$ is an approximation to the h_ℓ defined in Seaton [19]. Here m is the ratio of the reduced electron mass to the electron mass, z is the charge on the ion core. The effective quantum number ν is given by zm/k or $-(2\epsilon)^{-1/2}$.

The phase parameters ϑ and β are constants with respect to r :

$$\vartheta(\epsilon) = \frac{zm}{k} \ln 2k - \frac{\ell\pi}{2} + \arg \Gamma \left(\ell + 1 - \frac{izm}{k} \right), \quad (2.6)$$

$$\beta(\epsilon) = \pi(\nu - \ell). \quad (2.7)$$

The bound state coefficients C^+ and C^- go to infinity and zero respectively as $r \rightarrow \infty$. Their definitions are

$$C^+ = D^{-1} r^{-zm/\kappa} e^{\kappa r}, \quad C^- = 1/C^+. \quad (2.8)$$

D is a monotonic function of the energy that we shall not need in the following development. It is defined in Greene *et al.* [41]. In the reactance matrix representation, the wavefunction in fragmentation channel i' takes the form [33]

$$\Psi_{i'} = \sum_{i=1}^N |i\rangle [f_i(r)\delta_{ii'} - g_i(r)\mathcal{K}_{ii'}], \quad (r > r_0). \quad (2.9)$$

$|i\rangle$ is the wavefunction of the ionic core. Generally, the threshold is defined as the ionization energy of the atomic or molecular ground state plus the rotational, spin-orbit and vibrational energy of the ionic core.

2.1 Bound states

The condition that the exploding term C^+ in eqn. (2.8) vanish in all closed channels leads, *via* the definition of the wavefunction in eqn. (2.9) to the fragmentation channel quantization condition

$$\sum_{j=1}^N (\tan \pi \nu_i \delta_{ij} + \mathcal{K}_{ij}) Z_j = 0, \quad (2.10)$$

for which non-trivial solutions exist only where

$$\det(\mathcal{K} + \tan \pi \boldsymbol{\nu}) = 0. \quad (2.11)$$

In a single-channel system, the determinant is periodic in β . For the hydrogen atom, which has zero quantum defect, this leads to the Balmer series for integer ν . Where we have a non-zero quantum defect μ , as for alkali metals, $\mathcal{K} = \pi\mu$.

Fano [20] introduces the eigenchannel representation. The eigenchannels are obtained by diagonalizing \mathcal{K}

$$\mathcal{K}_{ij} = \sum_{\alpha=1}^N \mathcal{U}_{i\alpha} \tan \pi\mu_{\alpha} \mathcal{U}_{\alpha j}^{-1}. \quad (2.12)$$

Fano's eigenchannel solutions have the long-range form

$$\psi_{\alpha}(E) = \sum_i^N |i\rangle \mathcal{U}_{i\alpha} [f_i(r) \cos \pi\mu_{\alpha} - g_i(r) \sin \pi\mu_{\alpha}]. \quad (2.13)$$

The eigenchannel coefficients \mathbf{A} are defined by Fano's quantization condition

$$\sum_{\alpha=1}^N (\sin \pi\nu_i \mathcal{C}_{i\alpha} + \cos \pi\nu_i \mathcal{S}_{i\alpha}) A_{\alpha} = 0, \quad (2.14)$$

where $\mathcal{C}_{i\alpha} = \mathcal{U}_{i\alpha} \cos \pi\mu_{\alpha}$ and $\mathcal{S}_{i\alpha} = \mathcal{U}_{i\alpha} \sin \pi\mu_{\alpha}$. Comparison of eqns. (2.10) and (2.14) shows that the fragmentation channel Z_j and eigenchannel A_{α}

coefficients are connected by

$$Z_i = \sum_{\alpha=1}^N \mathcal{U}_{i\alpha} \cos \pi \mu_{\alpha} A_{\alpha}, \quad (2.15)$$

where N is the total number of channels. Where the energy of the system is lower than all of the ionization or dissociation thresholds, or where we neglect the coupling to these continua, we search for the energy levels E_{ν} given by eqn. (2.11).

To normalize eqn. (2.13) to the bound-state equivalent of a delta function of energy, Fano [20] derives the integral

$$N_n^2 = \frac{1}{\pi} \sum_{i,\alpha} A_{\alpha} \mathcal{U}_{i\alpha} \cos(\beta_i + \pi \mu_{\alpha}) \frac{d}{dE} \left[\sum_{\alpha'} A_{\alpha'} \mathcal{U}_{i\alpha'} \sin(\beta_i + \pi \mu_{\alpha'}) \right]_{E=E_n}. \quad (2.16)$$

If we neglect the energy dependence of all terms in eqn. (2.16) but β_i , we obtain

$$N_n^2 \simeq \frac{1}{\pi} \sum_i \frac{d\beta_i}{dE} \left[\sum_{\alpha} A_{\alpha} \mathcal{U}_{i\alpha} \cos(\beta_i + \pi \mu_{\alpha}) \right]^2. \quad (2.17)$$

Two observations are in order: first, that if we use wavenumber units, then the dimensions of $d\beta_i/dE$ are (energy)⁻¹, as

$$\pi \frac{d}{dE} \sqrt{\frac{\text{Ry}}{E_i^+ - E}} = \frac{\pi \nu^3}{2\text{Ry}}, \quad (2.18)$$

where ν is dimensionless; secondly, that this is π times the level spacing. Replacing $d\beta/dE = \nu^3/(2\text{Ry})$ and applying eqn. (2.15) yields the normalization constant

$$N^2 = \frac{1}{2\text{Ry}} \sum_i \nu_i^3 \left(\sum_j (\cos \beta_i \delta_{ij} - \sin \beta_i K_{ij}) Z_j \right)^2. \quad (2.19)$$

2.2 The Beutler region

Where some channels are open and some closed, we require that the electron have the same phase $\pi\tau$ in each open channel. There will clearly be as many solutions as there are open channels N_o , and these ‘collision eigenchannel’ solutions have the form

$$\psi_\rho(E) = \sum_{i=1}^{N_o} |i\rangle T_{i\rho} [f_i(r) \cos \pi\tau_\rho - g_i(r) \sin \pi\tau_\rho] \quad (2.20)$$

at large r . Eqn. (2.9) can be rewritten as

$$\Psi \xrightarrow[\epsilon > 0]{r \rightarrow \infty} \sum_{i,j}^{N_o} |i\rangle (\delta_{ij} \sin \pi\zeta_i - K_{ij} \cos \pi\zeta_i) Z_j, \quad (2.21)$$

which we can expand in $\sin \pi \zeta_i = \sin \pi(\zeta_i - \tau + \tau)$ to read

$$\begin{aligned} \Psi \xrightarrow[\epsilon > 0]{r \rightarrow \infty} \sum_{i,j} |i\rangle \{ \sin \pi(\zeta_i - \tau) [\delta_{ij} \cos \pi\tau + K_{ij} \sin \pi\tau] Z_j \\ + \cos \pi(\zeta_i - \tau) [\delta_{ij} \sin \pi\tau - K_{ij} \cos \pi\tau] Z_j \}, \end{aligned} \quad (2.22)$$

hence $[\delta_{ij} \sin(-\pi\tau) + K_{ij} \cos(-\pi\tau)] Z_j = 0$ and the open channel condition

$$\sum_i (\tan \pi(-\tau) \delta_{ij} + K_{ij}) Z_j = 0, \quad (2.23)$$

which leads to the overall equation

$$\begin{bmatrix} \tan \beta + \mathcal{K}_{cc} & \mathcal{K}_{co} \\ \mathcal{K}_{oc} & \tan(-\pi\tau) + \mathcal{K}_{oo} \end{bmatrix} \begin{bmatrix} \mathbf{Z}_c \\ \mathbf{Z}_o \end{bmatrix} = 0, \quad (2.24)$$

from which the closed channels can be eliminated by writing the closed channel coefficients \mathbf{Z}_c in terms of the open channel coefficients \mathbf{Z}_o , inserting them into the open-channel part of the matrix, and obtaining

$$\mathbf{K}(E) = \mathcal{K}_{oo} - \mathcal{K}_{oc} [\tan \beta + \mathcal{K}_{cc}]^{-1} \mathcal{K}_{co}. \quad (2.25)$$

We diagonalize to find the open-channel eigenvectors \mathbf{Z}_o and the N_o eigenphases $\tan(\pi\tau_\rho)$ labelled by ρ . The collision eigenchannel eigenvectors $T_{i\rho}$ are

[33]

$$T_{i\rho}(E) = \sum_{\alpha=1}^N \mathcal{U}_{i\alpha} \cos \pi(-\tau_\rho(E) + \mu_\alpha) A_{\alpha\rho}(E). \quad (2.26)$$

Expanding the trigonometric expressions, and multiplying eqn. (2.29) by $\sin \pi\tau_\rho$, and eqn. (2.26) by $\cos \pi\tau_\rho$, we find that

$$\begin{aligned} 0 &= \sum_{\alpha=1}^N \mathcal{U}_{i\alpha} (-\sin^2 \pi\tau_\rho \cos \pi\mu_\alpha + \cos \pi\tau \sin \pi\tau \sin \pi\mu_\alpha) A_\alpha, \\ \cos \pi\tau_\rho T_{i\rho} &= \sum_{\alpha=1}^N \mathcal{U}_{i\alpha} (\cos^2 \pi\tau_\rho \cos \pi\mu_\alpha + \cos \pi\tau \sin \pi\tau \sin \pi\mu_\alpha) A_\alpha \\ &= \sum_{\alpha=1}^N \mathcal{U}_{i\alpha} (\cos^2 \pi\tau + \sin^2 \pi\tau) \cos \pi\mu_\alpha A_\alpha = Z_{i\rho,0}. \end{aligned} \quad (2.27)$$

Now we have the matrix of fragmentation eigenchannels \mathbf{Z} , they are normalized to

$$\cos \pi\tau_\rho = \sum_{i \in \rho} Z_{i\rho}(E) \cdot Z_{i\rho}(E). \quad (2.28)$$

This also follows from the unitarity of the transformation between open fragmentation channels and collision eigenchannels. Given Fano's eigenchannel condition

$$\sum_{\alpha=1}^N \mathcal{U}_{i\alpha} \sin \pi(-\tau_\rho + \mu_\alpha) A_{\alpha\rho} = 0, \quad (2.29)$$

we can obtain the short-range eigenvectors \mathbf{A}

$$A_{\alpha\rho}(E) = \sec \pi\mu_\alpha \sum_i \mathcal{U}_{\alpha i}^{-1} Z_{i\rho}^o(E), \quad (2.30)$$

which is the Beutler region analogue of eqn. (2.15).

2.3 Measurable quantities

The oscillator strengths are determined by converting the fragmentation channel coefficients \mathbf{Z} into eigenchannel coefficients \mathbf{A} by inverting eqn. (2.15) and inserting \mathbf{A} into the oscillator strength expression

$$f_\nu = \frac{4\pi^2 E}{2(2J'' + 1)} \left| \sum_\alpha \mathcal{D}_\alpha A_\alpha \right|^2. \quad (2.31)$$

The collision eigenchannel transition matrix elements $D_\rho(E)$ are calculated separately for transitions from each component γ'' of the ground state by

$$D_\rho^{\gamma''}(E) = \sum_{\alpha=1}^N D_\alpha^{\gamma''} A_{\alpha\rho}(E). \quad (2.32)$$

The total cross section, such as would be measured in a photoionization experiment, is a properly-weighted sum over all open channels and all electronic and rotational components γ'' of the initial state

$$\sigma(E) = \frac{4\pi^2 E}{3(2J'' + 1)} \sum_{\rho, \gamma''} \left| c^{\gamma''} D_\rho^{\gamma''}(E) \right|^2. \quad (2.33)$$

Branching ratios into individual Hund's case (d) fragmentation channels are given in terms of the reduced dipole matrices in [33], calculated separately for each initial state component by

$$D_i^{\gamma''}(E) = \sum_{\rho=1}^{N_o} e^{i\theta_i(E)} T_{i\rho}(E) e^{i\pi\tau_\rho(E)} D_\rho^{\gamma''}(E), \quad (2.34)$$

which are then summed into the partial cross section σ_i , which is used in the calculation of branching ratios, photoelectron spectra and photoelectron angular distributions:

$$\sigma_i(E) = \frac{4\pi^2 E}{3(2J'' + 1)} \sum_{\gamma''} \left| c^{\gamma''} D_i^{\gamma''}(E) \right|^2. \quad (2.35)$$

Note that summing eqn. (2.35) over all channels i reduces to eqn. (2.33).

Bound state interactions, normalized by eqn. (2.19) and interactions with the continuum, normalized by eqn. (2.28) have dimensions of (intensity) and (intensity energy⁻¹) respectively. Hargreaves [42] addressed this problem first for the Coulomb potential, where he showed that $n^3 f_n$ and df/dE join smoothly at threshold, where f_n is the differential absorption strength. Allison and Dalgarno [43] generalize this result to arbitrary potentials, arguing that

$$\frac{\Delta f}{\Delta E} = \frac{f_n \Delta n}{\Delta E} \simeq f_n \frac{dn}{dE}. \quad (2.36)$$

As shown in eqn. (2.18), $d\nu/dE$ has the dimensions of $(\text{energy})^{-1}$. Where necessary, for instance for direct comparison of photoionization cross sections and photoabsorption oscillator strengths, we ensure continuity across thresholds by removing the $d\beta/dE$ term from the bound-bound normalization in eqn. (2.19) (thus multiplying each channel's contribution by the correct continuity factor) and obtain

$$N^2 = \sum_i \left[\sum_j (\cos \beta_i \delta_{ij} - \sin \beta_i K_{ij}) Z_j \right]^2. \quad (2.37)$$

2.4 Radial matrix elements

The initial development of MQDT followed from the Coulomb approximation of Bates and Damgaard [16], who neglected the effect of the core on $s \rightarrow p$ and $p \rightarrow d$ transitions between orbitals with $n = 2, 3$. Their treatment of only the outermost electron is more approximate than in the Rydberg-Rydberg case which we shall now consider.

If we solve eqn. (2.1) by assuming a solution of the form $r^{\ell+1} e^{-Zr/n} f(r)$, where $f(r)$ is a power series obtained by the method of Frobenius, the solution is the confluent hypergeometric function [40] $M(-n + \ell + 1, 2\ell + 1, 2Zr/n)$,

which is normalized as

$$\psi_{n\ell} = \sqrt{\frac{Z\Gamma(n+\ell+1)}{n^2\Gamma(n-\ell)} \frac{(Zr/n)^{\ell+1}}{\Gamma(2\ell+2)}} e^{-2Zr/n} M(-n+\ell+1, 2\ell+2, 2Zr/n). \quad (2.38)$$

The confluent hypergeometric function

$$M(a, b, x) = \sum_m \frac{(a)_m x^m}{(b)_m m!}, \quad (2.39)$$

where $(\alpha)_b$ is the Pochhammer symbol, converges where $x < 1$ and if a is a negative integer. For the hydrogen atom n is an integer and the function converges. In general, however, n is not necessarily an integer and the function does not converge for $r > n/2Z$.

These considerations point us at different solutions. First, Bates and Damgaard [16] treat the not-necessarily-convergent confluent hypergeometric function as an asymptotic series that terminates at its smallest value (though in practice they actually stopped a few terms before this because it was 1949 before computers were cheap and universally available).

A second approach is to ensure that the wavefunction is quantized by shifting the inner wall of the potential, which is $\ell(\ell+1)/2 a_0$ at threshold. An example is the quantum defect orbital (QDO) method of Simons [44], later elaborated by Martín and co-workers [45, 46], which has been justified

physically by Zon and co-workers [47–49]. Greene *et al.* [41, 50] observe that electron interactions with a core dipole vary as r^{-2} dependence, and write $\lambda(\lambda + 1) = \ell(\ell + 1) - a$, where a quantifies the effect of the dipole. Chernov *et al.* [49] then identify λ with $\ell - \mu^{\text{dip}}$, where μ^{dip} is a dipole-induced phase shift or quantum defect. Higher-order polarization terms in the potential are proportional to r^{-3} , r^{-4} and so on, and they chiefly affect the inner wall of the potential and shift the wavefunction inward or outward, contributing to the quantum defect. The QDO replaces the angular momentum variable ℓ in eqn. (2.38) with λ on purely phenomenological grounds, however:

$$\lambda = \ell - \mu + \text{Int}, \quad (2.40)$$

where Int is a function that gives the wavefunction the correct number of nodes. Martín and Simons [45] choose $\text{Int}_{\text{QDO}}(\mu)$, where Int_{QDO} is the integer *closest* to μ . A test of the QDO approximation is Fig. 2.2, showing the variation of transition moment against n for a d→f transition. The discontinuities are particularly obvious. This might not seem like a severe problem, given that any Rydberg series will have quantized n with roughly integer spacing. However, it is not uncommon for μ to be close to half-integer, and it is physically unreasonable for very small changes in the quantum defect to

have large effects on molecular properties. The number of radial nodes is

$$\tilde{n} = n - \ell - \text{Int} - 1. \quad (2.41)$$

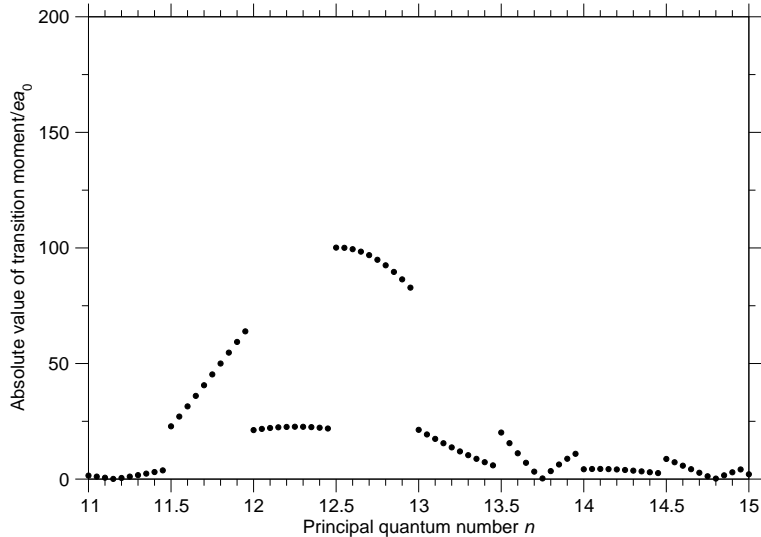
If we choose $\mu < 1$, then \tilde{n} will be discontinuous at integer ν . Regardless of our choice of μ or n , both \tilde{n} and λ will be discontinuous at half-integer ν . The *ansatz* of Chernov *et al.* [49], however, is based on

$$n_r = \nu - \tilde{l}(J\kappa) - 1, \quad (2.42)$$

the number of radial nodes. Again, the introduction of a short-range quantum defect imposes a choice of number of nodes, and different values for channels with the same n but different μ . We would expect a smooth function of n as calculated in Zimmerman *et al.* [51], showing Young's slit-like behaviour as the initial and final state wavefunctions move in and out of phase with increasing energy. In passing, we should mention *Cooper minima*, which are seen when the transition moment passes through zero. They are important in the case of dipole transitions from small- n states to the continuum. Their origin is the slow outward stretching of the continuum wavefunction with increasing energy.

A third approach approximates the long-range part of the functions with

Figure 2.2: Absolute value of the QDO transition moment for the $12.4d \rightarrow nf$ transition plotted against n .



Bessel functions and using the Weber–Schafheitlin-type analytical forms of the integrals [ref. [40], eqns. (11.4.33) and (11.4.34)] to $\langle nl | r^k | n'l' \rangle$ made in Gilbert and Child [52] and extended beyond dipole couplings to other negative powers of r^k by Bixon and Jortner [53]. However, they only hold for $k < 1$.

Method

In order to avoid the discontinuities and limited range of n of the present method, we take a fourth approach and integrate the Coulomb wavefunctions numerically. Note, however, that the expressions in Abramowitz and Stegun [40] for the Laguerre polynomial break down for $n > 30$ and large r (where

the wavefunction has the greatest amplitude).

Instead, following Zimmerman *et al.* [51], we use the Numerov–Cooley algorithm [54, 55], which is widely used to calculate bound state wavefunctions, for positive k , the irregular Coulomb function g by integrating inwards from $1.5r_+$, because the integrand will be largest for large r . The distance beyond r_+ at which g diminishes to insignificance depends on n : the closer to threshold, the flatter the potential at the outer turning point, and the faster (proportionally) it dies away within the barrier. g 's ill behaviour for non-half-integer n is restricted by the condition $r > 0$ and the relative unimportance of the core region to Rydberg wavefunctions where $\ell(\ell + 1) \ll n^2$, as we have fixed the core-induced phase shift by our choice of ν . Our code is based on Cashion [56] but borrows ideas from LeRoy's LEVEL [57] and Jungen's DENER [58]. We use a linear instead of the logarithmic basis in [51]. Finally, as the function belongs to a bound state, we obtain the normalization constant by integrating $\psi(r_i)\psi(r_i)^*$.

Examples

Fig. 2.3 shows a 16f wavefunction calculated by the above method. It consists of a long oscillatory section ending in a pronounced lobe at the outer turning point, which matches the classical picture of an electron on an elliptical orbit. Note that g does not go to zero as $r \rightarrow 0$.

Figure 2.3: A 16f $g(r)$ wavefunction calculated by Numerov–Cooley.

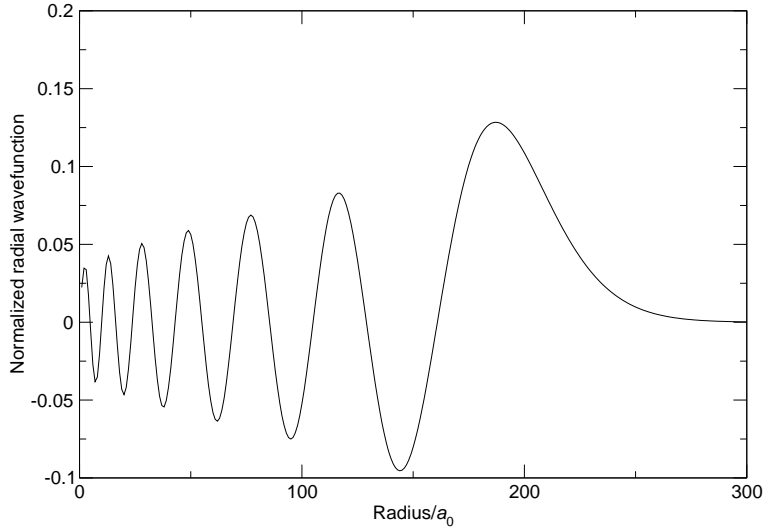


Fig. 2.4 is an example of a smooth dependence of transition moment on n , peaking (or in this case troughing) at $\Delta n = 0$. Figure 2.5, where we plot the square of the transition moment multiplied by n^3 shows that our results fit the expected behaviour for Rydberg–Rydberg transition moments in that the function is smooth, and for large n scales as $n^{-3/2}$. More interesting is Fig. 2.6, which shows that the transition moment falls off faster than $(\Delta n)^{-3}$, for $n' < n$. This is because the range of integration that contributes is only slightly larger than n'^2 . Finally, Fig. 2.7 shows two examples of matrix elements relevant to the long-range force calculations later in this thesis. The top panel shows dipole-coupling (r^{-2}) elements between s and p ZEKE states. These are qualitatively different from the integrals of r , which are dominated

Figure 2.4: Plot of the $12.1f \rightarrow ng$ transition moment against n . Note that this

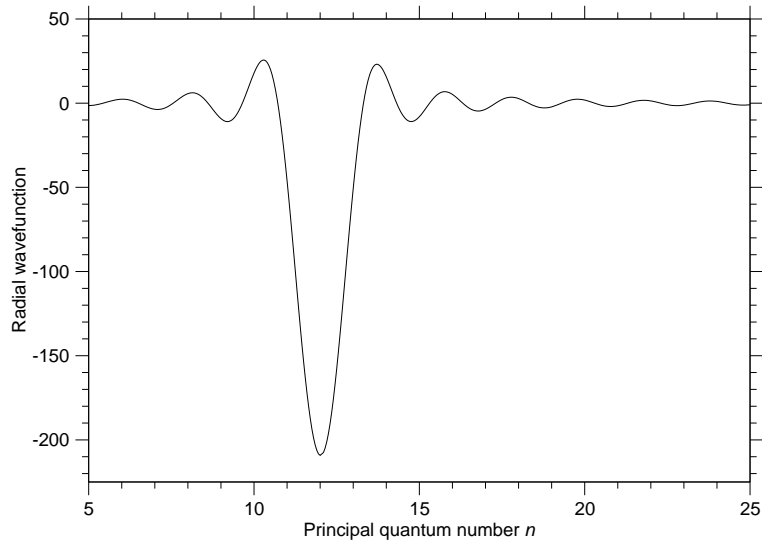


Figure 2.5: Plot of the $5.4f \rightarrow ng$ transition moment squared and scaled by n^3 , against n . Note that the n^3 scaling shifts the maxima of the transition moment.

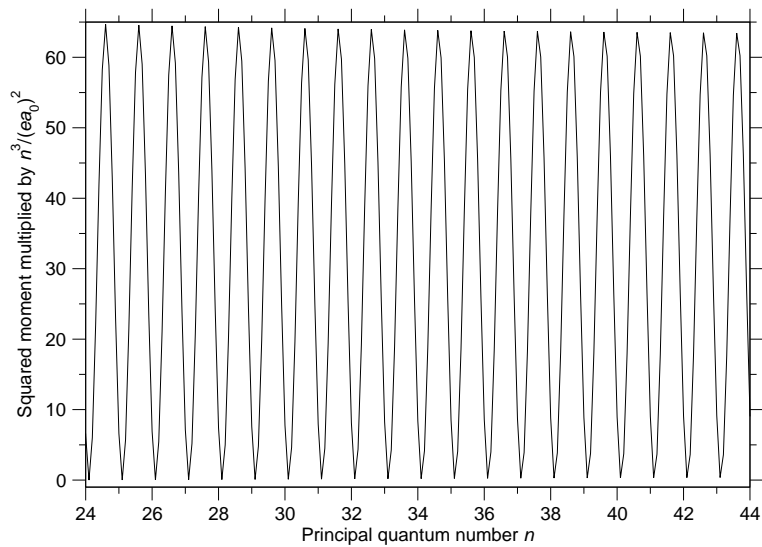
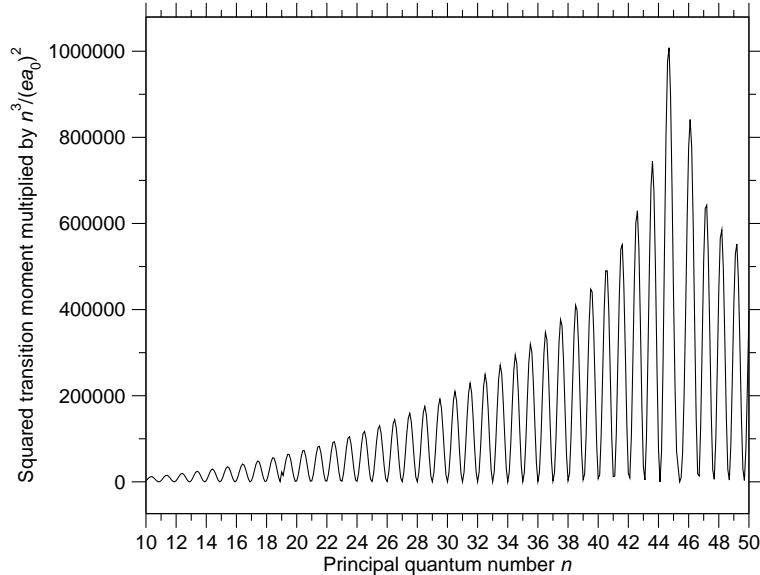


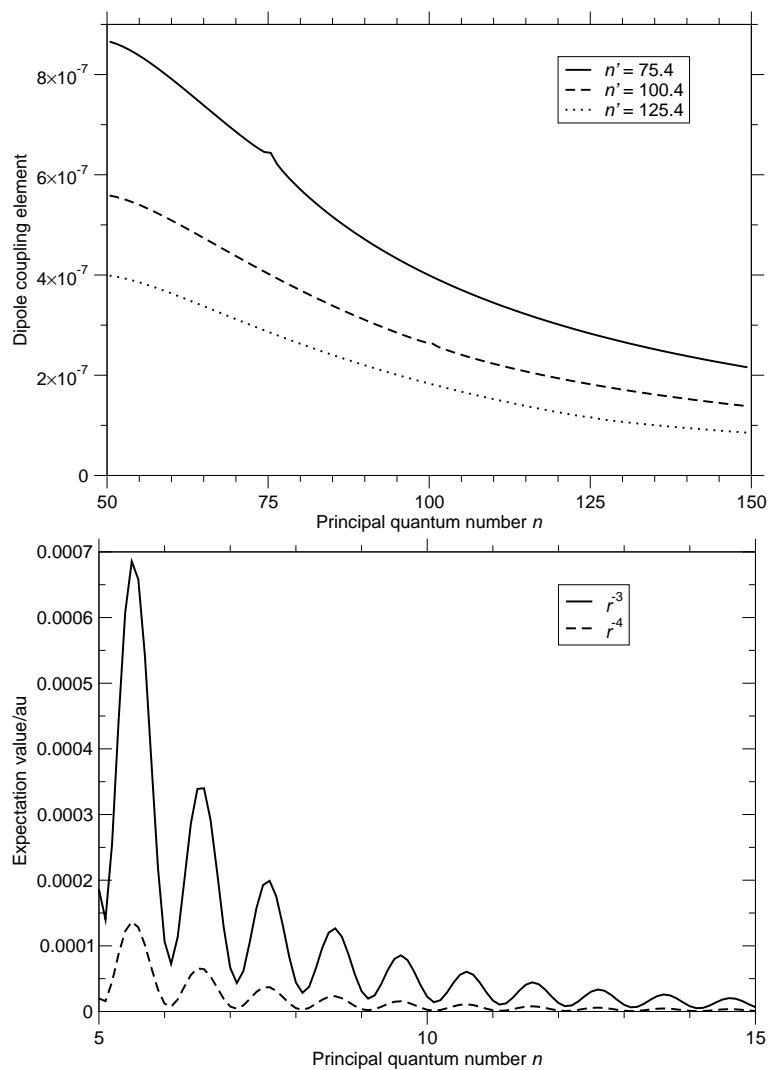
Figure 2.6: Plot of the $45.4f \rightarrow ng$ transition moment squared and scaled by Δn^3 against n . The zero at $n = 45.4$ is where $\Delta n = 0$; the transition moment reaches a maximum there.



by the lobe at the outer turning point, because negative powers of r are largest near the core.

Caution: The bottom panel in Fig. 2.7 shows the shortcomings of using the irregular Coulomb function for quadrupole-coupling (r^{-3}) and polarizability (r^{-4}) elements. Significant error has been introduced by the ill behaviour of $g(r \rightarrow 0)$. It is probably better in these cases to use its regular counterpart $f(r)$, being careful of its divergence where $r > r_+$.

Figure 2.7: Above: $\langle ns | r^{-2} | n'p \rangle$ for ZEKE states at constant quantum defect. This is chosen to hide the interference effect as the ZEKE states go in and out of phase. Below: Expectation values of r^{-3} and r^{-4} for small- nf Rydberg states calculated by Numerov–Cooley.



Expectation values

These are calculated by Bockasten [59] and listed in full in Appendix 9.4.

The dipole, quadrupole and polarizability contributions we need:

$$\left\langle \frac{1}{r^2} \right\rangle_{n\ell} = \frac{1}{n^3(\ell + \frac{1}{2})} \quad (2.43)$$

$$\left\langle \frac{1}{r^3} \right\rangle_{n\ell} = \frac{1}{n^3\ell(\ell + \frac{1}{2})(\ell + 1)} \quad (2.44)$$

$$\left\langle \frac{1}{r^4} \right\rangle_{n\ell} = \frac{3 - \ell(\ell + 1)n^{-2}}{2n^3(\ell - 1)\ell(\ell + \frac{1}{2})(\ell + 1)(\ell + \frac{3}{2})} \quad (2.45)$$

$$= \frac{3 + \ell(\ell + 1)\epsilon}{2n^3(\ell - 1)\ell(\ell + \frac{1}{2})(\ell + 1)(\ell + \frac{3}{2})}. \quad (2.46)$$

Chapter 3

Molecular MQDT

We shall review the theoretical background of the adaptation of MQDT to molecular problems, with particular attention paid to the asymmetric top treatment by Child and Jungen [32].

3.1 Determination of quantum defects

The quantum defect is sometimes thought of as an empirical parameter, but, as we have seen above, it is a phase shift induced by the molecular core. Molecular Rydberg systems have many degrees of freedom and hence many quantum defects that need to be disentangled to describe the dynamics. Here are the main methods used:

- (i) Fitting. This is trivial in the case of a single Rydberg series, but

becomes rapidly more complicated with increasing degrees of freedom. While a simple matrix-diagonalization approach involves a linear fit, MQDT, which requires a non-linear fit, is needed where several n -manifolds overlap. This means that for real molecular systems fitting is a slow and methodical process.

(ii) There are two main *ab initio* approaches: one is to determine the potential energy surface of low Rydberg levels and extrapolate upwards. The other is the **R**-matrix method, where the quantum defects are obtained by matching *ab initio* wave functions to Coulomb functions at a given radius. This approach has been ‘turned inside out’ by Taylor and co-workers [27, 60] to calculate the quadratic Zeeman effect on Rydberg atoms and molecules. Here the Rydberg electron wave functions at short range (where the Zeeman potential can be neglected compared to the Coulomb) are matched to Zeeman-adapted long-range solutions.

(iii) For non-penetrating Rydberg levels, simple perturbative expressions for the energies and therefore quantum defects can be generated by considering the electrostatic and inductive interactions between the multipole moments and polarizabilities of the core and the electron.

Table 3.1: Notation for angular momenta.

Angular momentum	Body-fixed projection	Space-fixed projection
Electronic (ℓ)	λ	m_ℓ
Ion core (N^+)	K^+ or Ω^+ or P^+	M^+
Total (J or N)	K or Ω or P	M_J or M_N

3.2 Angular momentum basis states

Table 3.1 lists the notation for angular momenta. $|JKM\rangle$ is a rotational wavefunction for an open-shell system such as H_2O , while $|N\Omega M_\Omega\rangle$ and $|NPM_P\rangle$ are its counterparts for a closed-shell linear and non-linear system, respectively.

Hund's case (b) basis states $|\alpha\rangle$ are products $|\ell\lambda JKM\rangle$ of electronic wavefunctions $|\ell m\rangle$, which are spherical harmonics $Y_{\ell m}$ or $Y_{\ell\lambda}$, with rotational wavefunctions $|JKM\rangle$ which are Wigner rotation matrices

$$\sqrt{2J+1/8\pi^2} [\mathcal{D}_{MK}^J(\alpha\beta\gamma)]^* .$$

The conversion between space-fixed and body-fixed spherical harmonics is [61]

$$Y_{\ell\lambda}(\theta', \phi') = \sum_{m=-\ell}^{\ell} \mathcal{D}_{m\lambda}^\ell(\alpha\beta\gamma) Y_{\ell m}(\theta, \phi). \quad (3.1)$$

In Hund's case (d), we generate the basis states $|i\rangle$ by considering the coupled angular momentum problem for $\mathbf{J} = \mathbf{N}^+ + \boldsymbol{\ell}$.

$$\begin{aligned}
|N^+\ell JM\rangle &= \sum_{M^+,m} |N^+M^+\rangle |\ell m\rangle \langle N^+\ell M^+ m|JM\rangle \\
&= \sum_{M^+,m} (-1)^{J-M} \sqrt{2J+1} \begin{pmatrix} \ell & N^+ & J \\ m & M^+ & M \end{pmatrix} |N^+M^+K^+\rangle |\ell m\rangle
\end{aligned} \tag{3.2}$$

by the proportionality of the 3- j symbol [61] to the Clebsch–Gordan coefficient. For closed-shell cores, such as in NO^+ , $K^+ = 0$, which means that $K = \lambda$.

In his landmark paper where he first uses MQDT for molecular problems, Fano [20] introduces the parity-adapted case (b) wave functions of the hydrogen molecule, which in our notation we shall write

$$|\ell 0 J 0 M\rangle = \sqrt{(2J+1)/4\pi} |\ell 0\rangle |J 0 M\rangle \tag{3.3}$$

$$|\ell \pm 1 J \pm 1 M\rangle = \sqrt{(2J+1)/8\pi} [|J 1 M\rangle + (-1)^{p_e} |J-1 M\rangle], \tag{3.4}$$

where the parity variable p takes into account the inversion symmetry of the rotational wavefunction. The selection rule on dipole transitions is $\Delta p = \pm 1$.

H_2O in its ground state, and the Rydberg states considered in this thesis, are asymmetric tops of C_{2v} symmetry (there are also linear Rydberg states that are Renner–Teller coupled to the bent states). The asymmetric top has three independent rotational axes, leading to six possible choices of basis. Fig. 3.1 shows the I^r, II^r and III^r ‘right-handed’ conventions applied to the

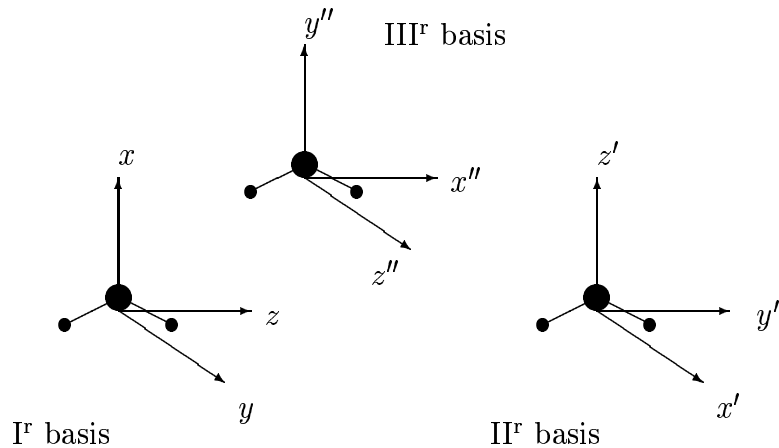


Figure 3.1: The III^r , II^r and I^r bases.

water molecule. The natural choice for the long-range force model is the ‘dipole’ II^r basis, where z' lies along the dipole axis, whereas the ‘spectroscopic’ choice [62, 63] is the I^r , where z lies along the a -axis. The a -, b - and c - axes are defined such that $I_a < I_b < I_c$ ($A > B > C$), where I_i are the moments of inertia and A , B and C are the rotational constants. Only rotations around the a - and c -axes are stable in phase space; an asymmetric top rotating around the b -axis will flop over repeatedly.

Asymmetric top eigenfunctions are sums of symmetric top eigenfunctions chosen to have the same symmetry properties as the rigid rotor Hamiltonian

$$H = AJ_a^2 + BJ_b^2 + CJ_c^2 \quad (3.5)$$

Table 3.2: C_{2v} symmetries of parity blocks for the asymmetric top.

p	p^*	C_{2v} symmetry
0	0	A ₁
0	1	B ₂
1	0	A ₂
1	1	B ₁

under the operations of D_2 . Note that this point group is not necessarily the same as that of the asymmetric top molecule itself. In addition to the exchange parity p defined above for the hydrogen molecule, the asymmetric top has another conserved parity p^* .

$$p = (p_e + p_r) \bmod 2 \tag{3.6}$$

$$p^* = (p_e + p_r + \lambda + K) \bmod 2,$$

where p_e and p_r are the Hund's case (b) electronic and rotational parities, respectively. Because the asymmetric top has two stable axes instead of only one, the rotational parity p_r is now 1 where $K_a \bmod 2 = K_c \bmod 2$ and 0 otherwise. The system is block diagonal in $\{J, p, p^*\}$, so the Hamiltonian and therefore the \mathbf{K} matrix can be partitioned and the properties of each symmetry block calculated separately. This is important because operations on an $N \times N$ matrix generally scale as N^3 . Gilbert *et al.* [63] give the C_{2v} symmetries for the parity component of each symmetry block (Table 3.2).

The parity-adapted rigid rotor and electronic eigenfunctions are

$$|JMK, p_r\rangle = \frac{|JMK\rangle + (-1)^{p_r+J} |JM-K\rangle}{\sqrt{2(1 + \delta_{K0})}} \quad (3.7)$$

$$|\ell\lambda, p_e\rangle = \frac{|\ell\lambda\rangle + (-1)^{p_e} |\ell-\lambda\rangle}{\sqrt{2(1 + \delta_{\lambda 0})}}, \quad (3.8)$$

respectively. In Hund's case (b), the total wavefunction is their product

$$\begin{aligned} |\lambda K, p_e p_r\rangle &= |\ell\lambda, p_e\rangle |JMK, p_r\rangle \\ &= \frac{(|\ell\lambda\rangle + (-1)^{p_e} |\ell-\lambda\rangle)(|JMK\rangle + (-1)^{p_r+J} |JM-K\rangle)}{\sqrt{(1 + \delta_{\lambda 0})(1 + \delta_{K0})}} \end{aligned} \quad (3.9)$$

which in terms of the total parity p is

$$|\lambda K, p\rangle = \frac{|JMK\ell\lambda\rangle + (-1)^{p+J} |JM-K\ell-\lambda\rangle}{\sqrt{2(1 + \delta_{\lambda 0}\delta_{K0})}} \quad (3.10)$$

while in Hund's case (d) we have

$$|N^+K^+, p\rangle = \frac{|JM\ell N^+K^+\rangle + (-1)^{p+N^++\ell} |JM\ell N^+-K^+\rangle}{\sqrt{2(1 + \delta_{K^+0})}} \quad (3.11)$$

p can also be defined as the parity under the permutation operation $\hat{P} = (12)^\wedge$, which rotates (x, y, z) by π about the x axis, and p^* is the parity under $\hat{P}^* = \hat{P}\hat{E}^* = \hat{E}^*\hat{P}$, where \hat{E}^* rotates by π about the y axis. Table 3.3 expresses $(12)^\wedge p$ and $\hat{E}^* p^*$ in different representations. A thorough descrip-

Table 3.3: Effect of $(12)^\wedge$ and \hat{E}^* on asymmetric top basis states

Wavefunction	$(12)^\wedge p$	$\hat{E}^* p^*$
Case (b _s)	$p_e + p_r$	$p_e + p_r + K + \lambda$
Case (b)	$p(\mathbf{b}_s) + \ell$	$p(\mathbf{b}_s) + K + \lambda$
Case (d)	$p(\mathbf{b}_s)\ell$	$p(\mathbf{b}_s) + K^+$

tion of molecular parities and their application to spectroscopy is given by Bunker and Jensen [64].

3.3 Frame transformations

To connect the short-range dynamics of the electron within the ionic core to the long-range dynamics, we need a frame transformation [20]. This must be unitary to preserve normalization. A simple physical interpretation of the matrix is that a pure $|\alpha\rangle$ state will ionize with branching ratios $|\langle\alpha|i\rangle|^2$ into long-range channels i .

The angular part, typically connecting Hund’s case (b) and (d) representations (neglecting spin), or (a) and (e) representations (including spin) will be a geometric quantity expressible in 3- j symbols. It is typically ‘square’, with most matrix elements $\mathcal{U}_{i\alpha}$ non-zero. The vibrational and electronic contributions are calculated by diagonalizing the short-range \mathbf{K} matrix to find the Fano eigenchannels.

An empirical justification for the frame-transformation technique is that

in many cases we expect the short-range dynamics to be nearly diagonal in the electronic and rotational basis states. If we are fitting parameters such as quantum defects to experiment, it is clearly easier to deal with N parameters than N^2 .

Fano [20] obtains the Hund's case (b)–(d) frame transformation for a closed-shell diatomic ion core.

$$\mathcal{U}_{i\alpha} = (-1)^{J-\lambda} \sqrt{2N^+ + 1} \left[\begin{pmatrix} \ell & N^+ & J \\ \lambda & 0 & \lambda \end{pmatrix} + (-1)^{p+J} \begin{pmatrix} \ell & N^+ & J \\ \lambda & 0 & -\lambda \end{pmatrix} \right] \quad (3.12)$$

Child and Jungen [32] derive the appropriate frame transformation for asymmetric top basis states. Expanding the case (d) basis state in eqn. (3.2) in terms of spherical harmonics and Wigner rotation matrices we obtain

$$\begin{aligned} |N^+ \ell J M K^+ \rangle = & (-1)^{J+M} \sqrt{2J+1} \sqrt{\frac{2N^+ + 1}{8\pi^2}} \\ & \times \sum_{m, M^+} Y_{\ell m}(\theta, \phi) \left[\mathcal{D}_{M^+ K^+}^{N^+}(\alpha\beta\gamma) \right]^* \begin{pmatrix} \ell & N^+ & J \\ m & M^+ & -M \end{pmatrix}, \end{aligned} \quad (3.13)$$

which in body-fixed angular momenta becomes

$$\begin{aligned} |N^+ \ell J M K^+ \rangle = & (-1)^{J+M} \sqrt{2J+1} \sqrt{\frac{2N^+ + 1}{8\pi^2}} \sum_{m, M^+, \lambda} Y_{\ell \lambda}(\theta, \phi) \\ & \times \left[\mathcal{D}_{m\lambda}^{\ell}(\alpha\beta\gamma) \right]^* \left[\mathcal{D}_{M^+ K^+}^{N^+}(\alpha\beta\gamma) \right]^* \begin{pmatrix} \ell & N^+ & J \\ m & M^+ & -M \end{pmatrix}. \end{aligned} \quad (3.14)$$

The contraction formula given by Brink and Satchler [61] in eqn. (9.9) reduces the expression to

$$\begin{aligned}
|N^+ \ell J M K^+\rangle &= (-1)^{J-K} \sqrt{\frac{(2J+1)(2N^++1)}{8\pi^2}} [\mathcal{D}_{MK}^J(\alpha\beta\gamma)]^* \\
&\quad \times \sum_{\lambda, K} Y_{\ell\lambda}(\theta', \phi') \begin{pmatrix} \ell & N^+ & J \\ \lambda & K^+ & -K \end{pmatrix} \\
&= \sum_{\lambda, K} (-1)^{J-K} \sqrt{2N^++1} |JKM\rangle |\ell\lambda\rangle \begin{pmatrix} \ell & N^+ & J \\ \lambda & K^+ & -K \end{pmatrix},
\end{aligned} \tag{3.15}$$

which, noting that $|i\rangle = \sum_{\alpha} \mathcal{U}_{i\alpha} |\alpha\rangle$, yields

$$\mathcal{U}_{i\alpha} = (-1)^{J-K} \sqrt{2N^++1} \begin{pmatrix} \ell & N^+ & J \\ \lambda & K^+ & -K \end{pmatrix}, \tag{3.16}$$

which becomes the Fano [20] expression for the hydrogen molecule frame transformation, eqn. (3.12) if we set $K = \lambda$ and apply the proper parity rules. The parity rules for asymmetric top basis functions in eqns. (3.9) and (3.11) applied to eqn. (3.16) lead to

$$\begin{aligned}
\langle \lambda K, p_e p_r | N^+ K^+, p \rangle &= \frac{(-1)^{J-K} \sqrt{2N^++1} (1 + (-1)^{p+p_e+p_r})}{2\sqrt{2}(1 + \delta_{\lambda 0})(1 + \delta_{K 0})(1 + \delta_{K+0})} \\
&\quad \times \left[\begin{pmatrix} N^+ & \ell & J \\ K^+ & \lambda & -K \end{pmatrix} + (-1)^{p_e} \begin{pmatrix} N^+ & \ell & J \\ K^+ & -\lambda & -K \end{pmatrix} \right. \\
&\quad \left. + (-1)^{p+N^++\ell} \begin{pmatrix} N^+ & \ell & J \\ -K^+ & \lambda & -K \end{pmatrix} + (-1)^{p_r} \begin{pmatrix} N^+ & \ell & J \\ -K^+ & -\lambda & -K \end{pmatrix} \right], \tag{3.17}
\end{aligned}$$

which is the result in ref. [32].

3.4 Angular transition moments

Dill [65] defines the dipole transition moment operator as a sum over space-fixed contributions $\sum_m r C_{1m}(\theta, \phi) \mathcal{D}_{m0}^{(1)}(\alpha\beta\gamma)$, where (θ, ϕ) are the angular coordinates of the Rydberg electron and $(\alpha\beta\gamma)$ the Euler angles of the ionic core. He only considers transitions from the $s\sigma$ states of the hydrogen molecule, but we shall consider the general case of $\ell\lambda \leftarrow \ell'\lambda'$ transitions for the asymmetric top. The integral factorizes into the radial contribution $\langle \ell\lambda | r | \ell'\lambda' \rangle$, the calculation of which is described in detail in section 2.4, and angular contributions from the electron and ion core discussed below. The matrix elements of C_{1m} are given in Appendix B by eqn. (9.6), and those of $\mathcal{D}_{KM}^{(J)}(\alpha\beta\gamma)$ by eqn. (9.8). We can follow Child and Jungen [32] and apply the apparatus given above to obtain the matrix elements for the angular part of the general operator $\hat{O}_{\text{ang}} = C_{kq} \mathcal{D}_{q0}^{(k)}(\alpha\beta\gamma)$.

$$\begin{aligned}
\langle \lambda' K', p'_e p'_r | \hat{O}_{\text{ang}} | \lambda'' K'', p''_e p''_r \rangle &= \frac{1}{2} \sqrt{\frac{(2J''+1)(2J'+1)(2\ell''+1)(2\ell'+1)}{3(1+\delta_{\lambda''0})(1+\delta_{\lambda'0})(1+\delta_{K''0})(1+\delta_{K'0})}} \\
&\times \begin{pmatrix} \ell' & k & \ell'' \\ 0 & 0 & 0 \end{pmatrix} \left[\frac{1 + (-1)^{p'_e + p''_r + p'_e + p'_r + 1}}{2} \right] \\
&\times \left[\begin{pmatrix} J'' & k & J'' \\ K' & q & -K'' \end{pmatrix} + (-1)^{p'_r + J'} \begin{pmatrix} J' & k & J'' \\ -K' & q & -K'' \end{pmatrix} \right] \\
&\times \left[\begin{pmatrix} \ell' & k & \ell'' \\ \lambda' & q & -\lambda'' \end{pmatrix} + (-1)^{p'_e + p''_e} \begin{pmatrix} \ell' & k & \ell'' \\ -\lambda' & q & \lambda'' \end{pmatrix} \right. \\
&\quad \left. + (-1)^{p'_e} \begin{pmatrix} \ell' & k & \ell'' \\ -\lambda' & q & -\lambda'' \end{pmatrix} + (-1)^{p''_e} \begin{pmatrix} \ell' & k & \ell'' \\ \lambda' & q & \lambda'' \end{pmatrix} \right]. \tag{3.18}
\end{aligned}$$

They [32] also determine a propensity rule for asymmetric top transitions

$$|N^+ - J''| \leq \ell'' \tag{3.19}$$

based on the Hund's case (d) transition amplitudes

$$\langle 0 | \hat{d} | i \rangle = \langle 0 | \lambda'' K'', p''_e p''_r \rangle \langle \lambda'' K'', p''_e p''_r | \hat{d} | N^+ K^+, p' \rangle \langle N^+ K^+, p' | i \rangle. \tag{3.20}$$

It is a propensity rule rather than a firm selection rule because it only holds where all radial matrix elements are equal, and disregards quantum defects.

Rewritten in terms of the fragmentation channel eigenvectors $Z_{i\rho,0}$, the col-

lision eigenchannel [33] transition moments are

$$D_{\rho}^{\gamma''}(E) = \sum_{\alpha,i} D_{\alpha}^{\gamma''} \sec \pi \mu_{\alpha} \mathcal{U}_{\alpha i}^{-1} Z_{i\rho,o}(E). \quad (3.21)$$

If all quantum defects are zero, $\sum_{\alpha} D_{\alpha}^{\gamma''} \sec \pi \mu_{\alpha} \mathcal{U}_{\alpha i}^{-1}$ reduces to eqn. (3.20).

3.5 Vibrational autoionization

Vibrational interactions arise from the variation in the energy of a molecule with its geometry, and as such are examples of non-Born–Oppenheimer behaviour. Berry [66] studied vibrational autoionization in the 1960s by considering the Hamiltonian matrix elements left out of the BO approximation, and came up with the selection rule $\Delta v = -1$. Just as vibrational Hamiltonian matrix elements can be obtained by taking the integral of the Hamiltonian operator with vibrational wavefunctions over all coordinates, so can we obtain the \mathbf{K} matrix [33]:

$$K_{\alpha v, \alpha' v'} = \int \chi_v(\mathbf{Q}) \tan \pi \mu_{\alpha \alpha'}(\mathbf{Q}) \chi_{v'}(\mathbf{Q}) d\mathbf{Q}. \quad (3.22)$$

The ingredients we need, therefore, for a treatment of vibrational autoionization, are an idea of how the quantum-defect function varies with the motion of the molecular framework, and a reliable potential-energy surface for the

molecule. The quantum-defect function for a diatomic molecule can be determined from the potential energy curves of the Rydberg state and the molecular ion

$$U_{n\ell\lambda}(R) = U^+(R) - \frac{\text{Ry}}{[n - \mu_{\ell\lambda}(R)]^2}, \quad (3.23)$$

and a common literature approximation for diatomic molecules is to take them as harmonic oscillators. Herzberg and Jungen [67] use a perturbation theory treatment (see below) to study the vibrational autoionization rates of H_2 . They expand the quantum-defect function about the equilibrium point R_e^+ of the molecular ion

$$\mu(R) = \mu(R_e^+) + (R - R_e^+) \left. \frac{\partial \mu}{\partial R} \right|_{R_e^+} + (R - R_e^+)^2 \left. \frac{1}{2} \frac{\partial^2 \mu}{\partial R^2} \right|_{R_e^+} + \dots, \quad (3.24)$$

$$\therefore U_{n\ell\lambda}(R) = U^+(R) - \frac{\text{Ry}}{\nu^2} - \frac{2\text{Ry}}{\nu^3} \left. \frac{\partial \mu}{\partial R} \right|_{R_e^+} (R - R_e^+) + \frac{6\text{Ry}}{\nu^4} \left. \frac{\partial^2 \mu}{\partial R^2} \right|_{R_e^+} (R - R_e^+)^2 + \dots. \quad (3.25)$$

The Franck–Condon factor for harmonic oscillator basis states $\langle v|v' \rangle$ vanishes through the orthonormality of Hermite polynomials. As $\hat{R} = \hat{a}^\dagger - \hat{a}$, terms in \hat{R}^n couple states with the selection rule $\Delta v = -n$. The off-diagonal quantum defects from the linear and quadratic terms in eqn. (3.25) are

$$\langle v | \mu | v - 1 \rangle = \left. \frac{\partial \mu(R)}{\partial R} \right|_{R_e^+} \left[\frac{h}{8\pi^2 \mu_{\text{reduced}} \omega_C} \right]^{1/2} (v)^{1/2}, \quad (3.26)$$

$$\langle v | \mu | v - 2 \rangle = \left. \frac{\partial^2 \mu(R)}{\partial R^2} \right|_{R_e^+} \frac{h}{8\pi^2 \mu_{\text{reduced}} \omega c} \sqrt{v(v-1)}. \quad (3.27)$$

Jungen and Pratt [34] extend this formulation to polyatomic molecules. Indeed, as they treat the vibrational modes of a polyatomic molecule as simple harmonic oscillators, then very similar terms to eqn. (3.26) apply. In this thesis we shall use eqn. (3.22) to generate the quantum defects.

Having obtained the full reactance matrix, we need an eigenchannel basis $\{\gamma\}$ which we obtain by calculating the eigenvalues $\tan \pi \mu_\gamma$ and eigenvectors $\mathcal{U}_{\beta\gamma}^{(\text{short})}$ of the Hund's case (b) reactance matrix $\mathcal{K}^{(b)} = \tan \pi \boldsymbol{\mu}$. The transition moments \mathcal{D}_β are calculated in the unmixed Hund's case (b) basis and transformed into the short-range basis

$$\mathcal{D}_\gamma = \sum_{\beta} \mathcal{U}_{\beta\gamma}^{(\text{short})} \mathcal{D}_\beta. \quad (3.28)$$

3.6 Perturbations

Reactance matrix elements, and hence quantum defects, calculated by perturbation theory are useful for

- (i) Long-range polarization effects where $\ell \geq 3$, and
- (ii) Rydberg–valence interactions.

Taking a two-channel case of eqn. (2.10) to illustrate how to obtain off-

diagonal \mathcal{K} matrix elements from Hamiltonian matrix elements, we write

$$\det \begin{pmatrix} \mathcal{K}_{11} + \tan \beta(E) & \mathcal{K}_{12} \\ \mathcal{K}_{21} & \mathcal{K}_{22} + \tan \beta(E) \end{pmatrix} = 0, \quad (3.29)$$

and take $\tan \beta$ as the first two terms of a Taylor expansion about E_n :

$$\begin{aligned} \tan \beta(E) &\simeq \tan \beta(E_n) + \frac{d\beta}{dE} \sec^2 \beta(E_n)(E - E_n) + \dots \\ &= \frac{d\beta}{dE}(E - E_n), \end{aligned} \quad (3.30)$$

where $\beta = \pi \sqrt{\text{Ry}/(\text{IP} - E)} = \pi n$, so $(d\beta/dE) = \pi n^3/2\text{Ry}$. Comparing the condition for the existence of a bound state

$$\det \left[(E - E_n)\delta_{\alpha\alpha'} - \frac{2\text{Ry}\mathcal{K}_{\alpha\alpha'}}{\pi n^3} \right] = 0, \quad (3.31)$$

with the Schrödinger equation we obtain

$$\mu_{\alpha\alpha'} = \frac{1}{\pi} \arctan \frac{\pi n^3 \mathcal{H}_{\alpha\alpha'}}{2\text{Ry}} \quad (3.32)$$

which in the small angle approximation becomes [37]

$$\mu_n = \frac{n^3 E_n}{2\text{Ry}}, \quad (3.33)$$

which can be also obtained from the binomial expansion

$$\begin{aligned} E &= \text{IP} - \frac{\text{Ry}}{(n - \mu)^2} \simeq \text{IP} - \frac{\text{Ry}}{n^2} (1 - \mu/n)^{-2} \\ &= \text{IP} - \frac{\text{Ry}}{n^2} - \frac{2\mu\text{Ry}}{n^3} + O(n^{-4}). \end{aligned} \tag{3.34}$$

Having assembled the MQDT apparatus, we shall now apply it to some problems involving the water molecule and the nitric oxide molecule.

Chapter 4

Long-range-force model for the *nf* lines in Rydberg water

Child and Glab [36] report vibrational ionization spectra from two-photon transitions from the $\tilde{C}^1A_1(100)$ 0_{00} , 1_{01} , 1_{11} and 2_{02} levels of water, and fit them to a model where the five d and seven f quantum defects are individually adjustable parameters.

We shall derive a long-range-force model (LRFM) Hamiltonian for the interaction of the Rydberg electron with the ionic core in H_2O and use its parameters to refit the quantum defects to the lines in the spectra, and compare the parameters with quantities calculated *ab initio*.

4.1 Theory

To find the inner turning point of the Coulomb potential in eqn. (2.1) at threshold ($n = \infty$), we multiply through by r^2 to obtain $r_- = \ell(\ell + 1)/2$. Rydberg states of molecules with $\ell \geq 3$ will have an inner turning point outside typical ion core radii of $5 a_0$. They are *non-penetrating* and have, in the language of Mulliken, no precursors. The multipole and polarization interactions between the core and the Rydberg electron therefore dominate.

In 1926, Waller [68] derived an expression for the polarization-induced quantum defect of atomic ions. Later, Jungen and Miescher [37], Eyler and Pipkin [69], Watson [70] and Chang *et al.* [71] used perturbation theory to calculate multipole- and polarization-induced quantum defects for diatomic molecules. While the other authors concentrate on the quadrupole contribution, Watson considers the perturbation as a second-order dipole effect.

Stone [72] writes the first-order perturbation as an expansion in multipole moments:

$$\begin{aligned}
 H^{(1)} = & qV + \mu_\alpha V_\alpha + \frac{1}{3} \Theta_{\alpha\beta} V_{\alpha\beta} + \frac{1}{3 \cdot 5} \Omega_{\alpha\beta\gamma} V_{\alpha\beta\gamma} \\
 & + \frac{1}{3 \cdot 5 \cdot 7} \Phi_{\alpha\beta\gamma\delta} V_{\alpha\beta\gamma\delta} + \cdots + \frac{1}{(2n-1)!!} \xi_{\alpha\beta\dots\nu}^{(n)} V_{\alpha\beta\dots\nu} + \cdots,
 \end{aligned}
 \tag{4.1}$$

where $(2n-1)!! = (2n-1)(2n-3)\cdots 5 \cdot 3 \cdot 1$. The subscripts are in the Einstein convention, and only those terms that are totally symmetric enter

the Hamiltonian. For axially symmetric molecules, these transform as the even- m spherical harmonics $C_{\ell m}$ (Table 4.1). The n -pole- m -pole, or field-gradient, polarizabilities enter in second order

$$H^{(2)} = -\frac{1}{2}\alpha_{\alpha\beta}V_{\alpha}V_{\beta} - \frac{1}{3}A_{\alpha,\beta\gamma}V_{\alpha}V_{\beta\gamma} - \frac{1}{6}C_{\alpha\beta,\gamma\delta}V_{\alpha\beta}V_{\gamma\delta} - \dots \quad (4.2)$$

β_{zzz} is the dipole-dipole-dipole first hyperpolarizability, and γ_{zzzz} is the dipole-dipole-dipole-dipole second hyperpolarizability, which appear in the third and fourth order Hamiltonians respectively. Table 4.2 lists the n -pole- n -pole polarizabilities up to fourth order that enter the perturbation Hamiltonian for axially-symmetric molecules.

Disregarding the field-gradient polarizabilities, the Hamiltonians for the axially-symmetric point groups are

$$H^{D_{(n>2)h}} = H_{\parallel}^{\alpha} + H_{\parallel}^Q + H_{\parallel}^{\Phi} + H_{\parallel}^{\gamma} \quad (4.3)$$

$$H^{C_{(n>2)v}} = H^{D_{(n>2)h}} + H^{\mu} + H_{\parallel}^{\Omega} + H_{\parallel}^{\beta} \quad (4.4)$$

$$H^{D_{2h}} = H^{D_{(n>2)h}} + H_{\perp}^{\alpha} + H_{\perp}^Q + H_{\perp}^{\Phi} + H_{\perp}^{\gamma} \quad (4.5)$$

$$H^{C_{2v}} = H^{D_{2h}} + H^{\mu} + H_{\parallel}^{\Omega} + H_{\perp}^{\Omega} + H_{\parallel}^{\beta} + H_{\perp}^{\beta}. \quad (4.6)$$

Jungen and Miescher [37] use the $D_{\infty h}$ Hamiltonian in eqn. (4.3) as far as the terms in $C_{2m,m=0,\pm 2}$ (the quadrupole and the polarizability) to model the

Table 4.1: Explicit spherical tensor expressions for multipole terms in the LRFM Hamiltonian.

$$\begin{aligned}
H_{\parallel}^{\mu} &= \mu_z \frac{C_{10}}{r^2} \\
H_{\parallel}^Q &= Q_{zz} \frac{C_{20}}{r^3} \\
H_{\perp}^Q &= \sqrt{\frac{1}{3}}(Q_{xx} - Q_{yy}) \frac{C_{22c}}{r^4} \\
H_{\parallel}^{\Omega} &= \Omega_{zzz} \frac{C_{30}}{r^4} \\
H_{\perp}^{\Omega} &= \sqrt{\frac{3}{5}}(\Omega_{xxz} - \Omega_{yyz}) \frac{C_{32c}}{r^4} \\
H_{\parallel}^{\Phi} &= \Phi_{zzzz} \frac{C_{40}}{r^5} \\
H_{\perp}^{\Phi} &= \sqrt{\frac{4}{5}}(\Phi_{xxzz} - \Phi_{yyzz}) \frac{C_{42c}}{r^5} + \sqrt{\frac{1}{35}}(\Phi_{xxxx} - 6\Phi_{xxyy} + \Phi_{yyyy}) \frac{C_{44c}}{r^5}
\end{aligned}$$

Table 4.2: Explicit spherical tensor expressions for polarizability terms in the LRFM Hamiltonian.

$$\begin{aligned}
H_{\parallel}^{\alpha} &= \frac{\alpha}{2r^4} + (2\alpha_{zz} - \alpha_{xx} - \alpha_{yy}) \frac{C_{20}}{r^4} \\
H_{\perp}^{\alpha} &= \sqrt{\frac{1}{6}}(\alpha_{xx} - \alpha_{yy}) \frac{C_{22c}}{r^4} \\
H_{\parallel}^{\beta} &= \frac{\beta}{6r^5} + \frac{\beta_{zzz} C_{30}}{r^5} \\
H_{\perp}^{\beta} &= \sqrt{\frac{3}{5}}(\beta_{xxz} - \beta_{yyz}) \frac{C_{32c}}{r^5} \\
H_{\parallel}^{\gamma} &= \frac{\gamma}{24r^6} + \frac{\gamma_{zzzz} C_{40}}{r^6} \\
H_{\perp}^{\gamma} &= \frac{2}{\sqrt{5}}(\gamma_{xxzz} - \gamma_{yyzz}) \frac{C_{42c}}{r^6} + \frac{1}{\sqrt{35}}(\gamma_{xxxx} - 6\gamma_{xxyy} + \gamma_{yyyy}) \frac{C_{44c}}{r^6}.
\end{aligned}$$

nf Rydberg states of the nitric oxide molecule, neglecting the contributions of the small dipole moment.

$$\begin{aligned} H^{\text{NO}} &= H^{D_{(n>2)\hbar}} \\ &= \frac{1}{2} Q_{zz} \langle r^{-3} \rangle_{n\ell} \langle C_{20} \rangle_{\ell\lambda} + \frac{1}{2} \langle r^{-4} \rangle_{n\ell} \left[\alpha + \frac{1}{3} (\alpha_{\parallel} - \alpha_{\perp}) \langle C_{20} \rangle_{\ell\lambda} \right]. \end{aligned} \quad (4.7)$$

Standard angular momentum techniques [73] lead to

$$\langle C_{20} \rangle_{\ell\lambda} = -\frac{3\lambda^2 - \ell(\ell + 1)}{2(\ell - 1/2)(\ell + 3/2)}, \quad (4.8)$$

for the angular contribution,¹ therefore the angle-dependent and -independent terms are of opposite sign; we can think of the spherical polarizability α stabilizing the orbitals, making their quantum defects more negative, while the anisotropic core destabilizes or stabilizes orbitals according to their angular distribution. The n -dependence of the polarizability contribution leads to the Rydberg–Ritz term formula

$$T = \frac{2\text{Ry}}{(n - \mu_0 + c_1\epsilon - c_2\epsilon^2)^2}, \quad (4.9)$$

¹Biedenharn and Louck [74] call the zero quadrupole-induced quantum defect for the $f\delta$ orbitals a structural, or non-trivial zero of the $3-j$ symbol, as opposed to those geometrical zeroes where it fails to satisfy the triangle conditions. The next non-trivial zero in the $\langle \ell\lambda 20 | \ell - \lambda \rangle$ series is at $\ell = 48$, $\lambda = 28$. The zeroes will appear as a line in Fano's [75] analytic continuation of the Clebsch–Gordan coefficient to non-integer and non-half-integer values which is used in Stark effect MQDT.

where μ_0 is the notional quantum defect at threshold. Jungen [76] applies the same theory to the nd quantum defects of nitric oxide, but without the success of the nf levels.

We shall now derive the LRFM Hamiltonian matrix elements for the H_2O case. Expanding eqn. (4.6) as far as terms in C_{2m} , we obtain the energy of interaction in the II^F basis between the Rydberg electron and the core in terms of a dipole contribution

$$H^\mu = \mu \frac{C_{10}}{r^2}, \quad (4.10)$$

a quadrupole contribution

$$H^Q = (\mu^2 - Q_{zz}) \frac{C_{20}}{r^3} + \sqrt{\frac{1}{3}} (Q_{xx} - Q_{yy}) \frac{\sqrt{1/2}(C_{22} + C_{2,-2})}{r^3}, \quad (4.11)$$

and a polarizability contribution

$$H^\alpha = \frac{1}{2} \frac{\alpha}{r^4} + (2\alpha_{zz} - \alpha_{xx} - \alpha_{yy}) \frac{C_{20}}{r^4} + (\alpha_{xx} - \alpha_{yy}) \frac{\sqrt{1/2}(C_{22} + C_{2,-2})}{r^4}. \quad (4.12)$$

Using standard angular momentum techniques [73], we can determine the matrix elements of the general operator C_{kq} in Hund's case (b) for the asymmetric top.

$$\begin{aligned}
\langle \ell' \lambda' | C_{kq} | \ell \lambda \rangle &= \frac{(-1)^{\lambda'} \sqrt{(2\ell' + 1)(2\ell + 1)(1 + (-1)^{p_e + p'_e})}}{2((1 + \delta_{\lambda'0})(1 + \delta_{\lambda0}))^{1/2}} \begin{pmatrix} \ell' & k & \ell \\ 0 & 0 & 0 \end{pmatrix} \\
&\times \left[\begin{pmatrix} \ell' & k & \ell \\ -\lambda' & q & \lambda \end{pmatrix} + (-1)^{p_e} \begin{pmatrix} \ell' & k & \ell \\ -\lambda' & q & -\lambda \end{pmatrix} \right].
\end{aligned} \tag{4.13}$$

The properties of 3- j symbols lead to two general selection rules:

$$\Delta\ell = k, \quad \Delta\lambda = \lambda' + \lambda = q. \tag{4.14}$$

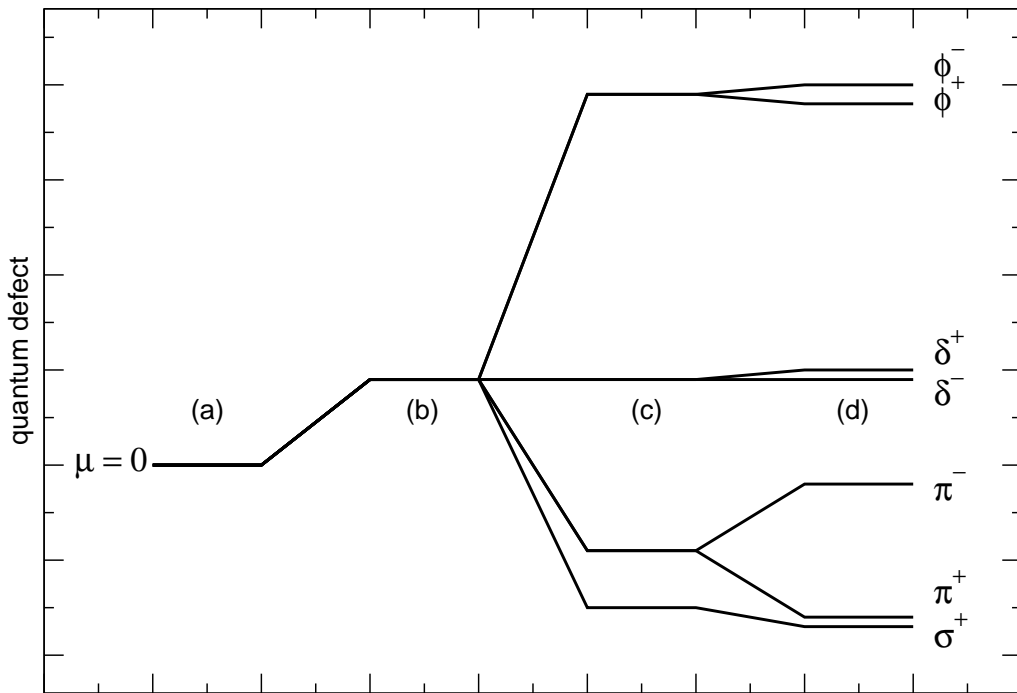
- (i) The first-order dipole mixes orbitals with equal λ and $\Delta\ell = \pm 1$.
- (ii) The second-order dipole mixes $\Delta\ell = \text{even}$, and is diagonal in λ . For terms diagonal in ℓ it reduces to the Watson [70] expression for dipole-induced quantum defects. The off-diagonal terms contribute to p-f mixing. There is no s-d contribution from the second-order dipole because the 3- j symbol vanishes. s-d mixing is therefore a core-induced effect.

(iii) The first-order quadrupole contribution results in λ -mixing of f orbitals of the same symmetry. It is also responsible for pushing apart the two fII orbitals, and contributes to s-d and p-f mixing.

These effects are shown graphically in Fig. 4.1.

Rather than transform \mathbf{K} between the bases shown in Fig. 3.1, we can

Figure 4.1: Schematic depiction of contributions of multipole moments and polarizabilities to the long-range-force-model nf quantum defects of an asymmetric top molecule. (a) No polarizability. (b) Introduction of isotropic polarizability shifts all quantum defects equally. (c) Moments of C_{20} symmetry split quantum defects by a factor proportional to $3\lambda^2 - 12$. (d) Contributions of $C_{22} + C_{2,-2}$ symmetry split $f\pi^\pm$ levels substantially and cause $f\sigma^+ - f\delta^+$ and $f\pi^\pm - f\phi^\pm$ mixing.



transform the relevant operators using the Wigner \mathcal{D} matrix [73] defined as

$$\mathcal{D}_{M'M}^{(J)}(\phi\theta\chi) = e^{-i\phi M'} d_{M'M}^J(\theta) e^{-i\chi M}, \quad (4.15)$$

where $(\phi\theta\chi)$ is the set of Euler angles that describe the transformations between bases in Fig. 3.1 and $d_{M'M}^J$ is a Wigner rotation matrix element.

(i) The first rotation is round the old z to bring the old y into the line of nodes N . It is in the line of nodes already, so $\phi = 0$.

(ii) The second rotation is around the line of nodes N to bring the old z into the new z' . It is a rotation of $\theta = \pi/2$.

(iii) The third rotation is around z' to bring the line of nodes N into the new y' . It is $\chi = \pi/2$.

Applying this matrix to the dipole and quadrupole operators

$$C_{10}^{\text{IIr}} = \sqrt{\frac{1}{2}} (C_{11}^{\text{Ir}} + C_{1,-1}^{\text{Ir}}), \quad (4.16)$$

$$C_{20}^{\text{IIr}} = \sqrt{\frac{3}{8}} (C_{22}^{\text{Ir}} + C_{2,-2}^{\text{Ir}}) - \frac{1}{2} C_{20}^{\text{Ir}}, \quad (4.17)$$

$$\sqrt{\frac{1}{2}} (C_{22}^{\text{IIr}} + C_{2,-2}^{\text{IIr}}) = \sqrt{\frac{1}{8}} (C_{22}^{\text{Ir}} + C_{2,-2}^{\text{Ir}}) + \sqrt{\frac{3}{4}} C_{20}^{\text{Ir}}. \quad (4.18)$$

Table 4.3: Comparison of $\tilde{C}(100) \leftarrow \tilde{X}(000)$ transitions in absorption (Mayhew) and ionization (Glab) spectra.

Transition	E_1/cm^{-1}		Correction/ cm^{-1}
	Mayhew ^a	Glab ^b	
$0_{00} \leftarrow 1_{10}$	83 806.37	83 805	+1.37
$1_{01} \leftarrow 2_{11}$	83 827.25	83 826	+1.25
$1_{11} \leftarrow 1_{01}$	83 840.21	83 843	-2.79
$2_{02} \leftarrow 3_{12}$	83 864.43	83 866	-1.57

^a Ref. [78]. ^b Private communication.

4.2 Fitting

In ref. [36], the spectra are referred to a two-photon spectrum of the \tilde{C} state. However, this is susceptible to predissociative line-broadening [77] which worsens with the number of photons used. A better choice is the one-photon absorption spectrum of the $\tilde{C}(100)$ level obtained by Mayhew [78] using synchrotron radiation. On comparing the two spectra, we find corrections borne out by careful examination of diagrams made by plotting the shifted energies

$$\Delta = \tilde{\nu} - \left(\text{IP} - \frac{\text{Ry}}{n^2} \right) \quad (4.19)$$

with the baselines offset by Ry/n^3 , as in Fig. 1 of ref. [36]. Table 4.3 lists the corrections.

In χ^2 non-linear fitting, we minimize the quantity

$$\chi^2(\mathbf{a}) = \sum_{i=1}^N \left(\frac{y_i - y(x_i; \mathbf{a})}{\sigma_i} \right)^2. \quad (4.20)$$

This is related to the standard deviation

$$\sigma^2 = \frac{1}{N} \sum_{i=1}^N (y_i - y(x_i; \mathbf{a}))^2. \quad (4.21)$$

The probability Q that this χ^2 should appear by chance is given by the complement of the incomplete gamma function

$$Q = \Gamma\left(\frac{N-2}{2}, \frac{\chi^2}{2}\right) / \Gamma(a), \quad (4.22)$$

where N is the number of data points, and

$$\Gamma(a, x) = \int_x^\infty e^{-t} t^{a-1} dt. \quad (4.23)$$

The χ^2 reported in ref. [36] are so high that the fit is meaningless without appealing to other evidence, for example the strong 2_{02} and 2_{20} high- n series in the 0_{00} spectrum.

An important matter is the composition of the \tilde{C} state. The *ab initio* calculations of Lee *et al.* [79] provide an expansion in terms of ℓ but not the

Table 4.4: Lines from Child and Glab [36] used to determine the $p\pi^- - d\sigma^+ - d\delta^+$ composition of the \tilde{C} state.

Energy/cm ⁻¹	Assignment	Integrated intensity
101962–101971	2.469d→6f2 ₀₂	12078.4
101987–102016	2.469p→6d	29987.1
102066–102074	2.469d→6f2 ₂₀	2109.2

λ -composition. We treat the $d\sigma - d\delta$ mixing of the \tilde{C} state by analysing the strengths of the 6f2₀₂ and 6f2₂₀ lines, relying on the case (d) propensity rule

$$K_a^+ = |K_a'' - \lambda''| \quad (4.24)$$

and observe that $d\sigma^+ \rightarrow f2_{02}$ and $d\delta^+ \rightarrow f2_{20}$. We further assume that predissociation affects the integrated intensities of the two f lines equally. Table 4.5 lists the squared transition moments from the \tilde{C} state to the featured lines, calculated by the Numerov–Cooley method. The MQDT code outlined in the theory chapter is then used to calculate ionization cross sections to the lines listed in Table 4.4 starting from the $p\pi^-$, $d\sigma^+$ and $d\delta^+$ states respectively. The system is solved to produce the results in Table 4.6.

The MQDT calculations are carried out for the (100) vibrational level neglecting its interactions with the other vibrational levels. Hence, at the energies involved, we can treat all channels as closed, and use the routine written by Gilbert and used in Vrakking *et al.* [62] to find the zeroes of $|\mathbf{K} - \tan \beta|$. It is described in Appendix A. We optimize the MQDT simula-

Table 4.5: Squared transition moments from the \tilde{C} state to the 6d and 6f states that feature in Child and Glab [36].

Initial state	Final state	R_{if}^2
2.469p π^-	5.86d σ^+	0.61
	5.68d π^+ , 5.30d π^+ ^a	1.89, 1.93
	5.91d π^-	0.34
2.469d σ^+ , d δ^+	5.97f	2.10
	6.00f	1.68
	6.03f	1.28

^a (010) quantum defect from Vrakking *et al.* [62].

Table 4.6: $\ell\lambda$ -composition of the \tilde{C} state.

Orbital	Percentage of \tilde{C} state	
	This work	Lee <i>et al.</i> [79]
s σ^+	—	12.97
p π^-	78.96	77.96
d σ^+	19.22	8.65(d)
d δ^+	1.82	
f π^- , ϕ^-	—	0.41

Table 4.7: *Ab initio* values for multipoles and polarizabilities of H₂O⁺ at the equilibrium geometry.

Multipole	Value/au	Polarizability	Value/au
μ_z	-0.89619		
Q_{xx}	-1.8913	α_{xx}	3.124
Q_{yy}	-0.64381	α_{yy}	6.062
Q_{zz}	-1.7771	α_{zz}	4.216

tions with the Levenberg–Marquardt code in Press *et al.* [80]. A small change in a parameter and hence a quantum defect can result in two lines swapping places, which can confuse the optimization routine. Currently the peaks are identified by energy E and intensity I and tracked with a goodness-of-fit criterion suggested by Jacobson [81]

$$M_{co} = \exp\left(\frac{-(E_c - E_o)^2}{2(\Delta E)^2}\right) \exp\left(\frac{-(I_c - I_o)^2}{2(\Delta I)^2}\right), \quad (4.25)$$

where subscripts c and o indicate ‘calculated’ and ‘observed’ peaks respectively, ΔE and ΔI define how good the match has to be. A ΔE of 5 cm⁻¹ and ΔI of 0.2 are used.

Table 4.7 shows the multipole moments and polarizabilities of the water ion at its equilibrium geometry from a single-point B3LYP/6-311+G** [82–85] calculation [86].

4.3 Results and discussion

Two approaches are used. Firstly, the quantum defects are optimized individually. Secondly, the parameters described above are the subject of optimization. We shall concentrate on the nf lines because (*i*) their energies are expected to depend strongly on the long-range-force model and (*ii*) because they are non-penetrating, they should show weaker linear–bent interactions than appears to be the case for the nd lines as seen in the recent experiments by Glab [87] on the quasilinear Rydberg states of H_2O .

Table 4.8 lists the nf lines used for the two fits. It is taken from the set in [36] with the obvious outliers removed. The next stage would be to add the predicted d–f interaction and to test whether the outliers are better fitted. This would involve some change in the ‘effective’ d quantum defects obtained by Child and Glab [36], and perhaps some reoptimization.

Table 4.8: $\ell = 3$ lines used in the fit. Energies E_{obs} are quoted relative to the (000) 0_{00} level of the ground electronic state of the water molecule. They have been taken from ref. [36] and adjusted as described in Table 4.3. ΔE_{μ} and ΔE_{LRFM} are the differences between experiment and the fits from optimizing quantum defects individually and the long-range-force model parameters respectively. I_{obs} is quoted in arbitrary units

$J''_{K''_a K''_c}$	J'	$E_{\text{obs}}/\text{cm}^{-1}$	$\Delta E_{\mu}/\text{cm}^{-1}$	$\Delta E_{\text{LRFM}}/\text{cm}^{-1}$	I_{obs}
0 ₀₀	1	101970.17	+1.48	+5.24	221
		102788.97	-1.73	+0.77	658
		103317.47	-1.59	+0.15	507
		103680.27	-2.29	-1.05	110
		103939.97	-3.09	-2.09	140
		104132.07	-4.00	-3.41	71
		102071.37	-1.57	-2.37	50
		103403.27	-1.50	-3.82	82
		103763.17	-0.99	-3.44	18
1 ₀₁	2	101933.65	+0.36	+2.65	1460
		103278.95	-2.19	-1.13	838
		103641.85	-3.77	-2.90	791
		103901.25	+3.91	-2.93	427
		104092.95	-4.71	-4.21	147
	1	102847.85	+0.73	-2.67	1579
		103376.75	-0.25	-2.25	1891
		103739.65	-1.54	-3.81	775
		103998.85	-2.23	-3.32	1265
	2	102059.65	+2.34	+4.55	882
		102872.05	+0.22	+0.66	10
		103398.76	-1.34	-1.44	383
		104017.95	-2.07	-2.38	84
		102122.05	+0.06	+1.18	94
		102934.45	-1.87	-1.51	100
1 ₁₁	2	102774.71	-2.79	0.25	8
		103919.71	-3.10	-2.99	4153
		104111.11	-4.11	-4.08	3918
		102859.81	+3.49	+3.50	17

Table 4.8: (*continued*)

$J''_{K''_a K''_c}$	J'	$E_{\text{obs}}/\text{cm}^{-1}$	$\Delta E_{\mu}/\text{cm}^{-1}$	$\Delta E_{\text{LRFM}}/\text{cm}^{-1}$	I_{obs}
		103388.11	+0.65	+1.00	10204
		103750.31	-0.65	-0.62	5828
		102010.91	+3.10	+1.49	347
	1	103345.11	-0.45	-3.20	3030
		103708.11	-2.64	-4.53	1331
		103966.11	-2.75	-3.97	1357
		104158.11	-3.78	-4.53	100
		102816.11	+1.84	-2.15	4
2_{02}	3	101918.43	+3.96	+3.94	1897
		102732.03	+2.59	+2.08	174
		103259.23	-2.54	-0.66	1444
		103622.93	-1.65	-2.20	43

Direct fitting of the quantum defects yields a standard deviation of 2.41 cm^{-1} and $\chi^2 = 250$, whereas fitting to the LRFM parameters yields a standard deviation of 2.87 cm^{-1} and $\chi^2 = 331$. Table 4.9 lists the quantum defects fitted individually to the spectrum, and compares them to the uncorrected values of ref. [36]. For the most part the overall pattern is preserved, but the splitting between the two π^{\pm} states is not only widened but reversed. The quantum defect for $f\delta^-$ remains very small, as we would expect. Table 4.10 compares the LRFM parameters fitted from the spectrum with those calculated *ab initio*. During the preparation of this thesis, it was worrying that the fitted polarizability was very nearly half the calculated value because of the $\alpha/2r^4$ term, but the fitted polarizability is indeed about 8 au instead of 4 au. It is reassuring that the dominant ‘dipole’ [actually

Table 4.9: Quantum defects for the nf states of Rydberg water obtained by fitting to the corrected lines in ref. [36] compared to the uncorrected lines in ref. [36].

$\ell\lambda$	This work	Ref. [36]
$f\sigma^+$	0.0225	0.0228
$f\pi^-$	-0.0026	0.0274
$f\pi^+$	0.0270	0.0143
$f\delta^+$	0.0209	0.0059
$f\delta^-$	0.0012	-0.0093
$f\phi^-$	-0.0229	-0.0105
$f\phi^+$	-0.0343	-0.0245

Table 4.10: Long-range-force model parameters obtained by fitting to the (corrected) nf lines of Child and Glab [36] compared to those obtained *ab initio*

Quantity	V	alue/au
	Fit	<i>Ab initio</i> ^a
Polarizability	8.13	4.47
‘Dipole’	1.82	2.34
‘Off-diagonal quadrupole’ terms	-15.26	-3.78

^a From Table 4.7.

$\mu^2 - Q_{zz} + (2\alpha_{zz} - \alpha_{xx} - \alpha_{yy})$] term is approximately 2 au. The large value of the ‘off-diagonal quadrupole’ term [actually $(Q_{xx} - Q_{yy})/\sqrt{3} + \alpha_{xx} - \alpha_{yy}$] may disguise contributions from interloper states, f-d and f-p couplings, as its inclusion only slightly improves the fit.

4.4 Conclusions

We have developed a model that relates the quantum defects, and hence the ionization spectra, of the Rydberg nf lines of the water molecule to the

long-range properties of the H_2O^+ ion. We have attempted to fit both the individual nf quantum defects and quantities derived from the long-range properties to experimental spectra, with similar results in both cases. Certainly the ‘dipole’ term in the model is close to that calculated *ab initio*.

A *caveat* is, however, in order. We know that the straight lines in Fig. 1 of ref. [36] show that the quantum defects are much smaller than unity. However, the χ^2 values for the fit in Child and Glab [36], and for both of the fits carried out here, are very far from conclusive according to eqn. (4.22). A better way, perhaps, of assessing the value of the fit is to perform Monte Carlo simulations of the data, which are described thoroughly in Press *et al.* [80]. In the bootstrap resampling method, new data sets of the same size as the original are generated by picking entries at random from it, and the estimated parameters are refitted many times. In this way, confidence limits can be extracted. For a two-parameter system with a normal distribution, the points are scattered in the shape of an ellipse. This analysis, while difficult to either depict graphically or indeed interpret for the seven-parameter system described above, is ideally suited to the three-parameter long-range-force model. It would certainly enable us to better assess the reliability of the polarizability and ‘dipole’ terms. While adding d–f and p–f interactions, for example, may marginally improve the fit, we are unlikely to see much better agreement with experiment without a full Renner–Teller treatment.

Chapter 5

Threshold ionization spectroscopy of Rydberg water

The ZEKE experiments of Tonkyn *et al.* [88] and the recent closely-related MATI experiments of Dickinson *et al.* [89] on water show lines that are inexplicable in terms of a dipole transition from pure p states, and difficult to explain notwithstanding the d contribution to the \tilde{C} state of water.

Gilbert and Child [52] observed that even though a channel might be forbidden from the ground state, states within it could borrow intensity from the states in a dipole-allowed channel if the two channels were coupled. This is particularly likely because of the high density of states near an ionization threshold. In that case it was the dipole moment (estimated to be about 1 D), although it could just as easily be another multipole moment [53],

the anisotropic contribution to the polarizability, Coriolis effects, spin–orbit coupling, or indeed the vibrational couplings mentioned in section 3.5 and explored by Chupka and Grant [90].

In this chapter we shall apply MQDT to the MATI spectra of Dickinson *et al.* [38].

5.1 Experiment

Tonkyn *et al.* [88] measure the ZEKE pulsed-field ionization (PFI) spectrum of water between $101\,700\text{ cm}^{-1}$ and $101\,900\text{ cm}^{-1}$. They use a discrimination field F_{disc} of 0.05 V cm^{-1} , and an ionization–extraction field F_{sluice} of $0.3\text{--}1.0\text{ V cm}^{-1}$. The jet-cooled water originates in the $\tilde{X}^1A_1(000)$ vibrational level and is assumed to have a rotational temperature of 15 K .

In Dickinson *et al.* [38] the $(2 + 1')$ MATI spectra of water are recorded *via* the $\tilde{C}^1B_1(000)$ state over the range $101\,700\text{--}102\,300\text{ cm}^{-1}$. They also record less well-resolved spectra *via* the $\tilde{C}^1B_1(010)$ and $\tilde{C}^1B_1(100)$ states that we shall not consider here.

MQDT calculations near threshold must be carried out on a very fine mesh, and are therefore expensive. Whereas on a modern desktop PC a simulation of ionization spectra at around $n = 6$ at a resolution of 0.1 cm^{-1} will take seconds, any simulation of ZEKE/MATI spectra will at least need to run

overnight. For even the crudest approximation to the ZEKE/MATI lineshape (the box in ref. [89], for example), we need to consider the ionization process and the range of energies over which ZEKE/MATI states can be measured. Chupka [91] distinguishes two modes of field ionization.

(i) For the hydrogen atom, the Runge–Lenz vector is an additional constant of motion to the quantum numbers n , ℓ and m_ℓ , and allows Stark levels of differing m_ℓ to cross as the electric field is increased or decreased. The ionization rate increases exponentially with electric field. Chupka [91] quotes limits of $(9n^4)^{-1} E_h$ ($4.5\sqrt{F}$ cm $^{-1}$) and $(4n^4)^{-1} E_h$ ($3.12\sqrt{F}$ cm $^{-1}$) for the reddest and bluest components of each Stark manifold respectively.

(ii) Non-zero quantum defects destroy the hydrogenic degeneracy and if the field changes at a small enough rate, the system will traverse the avoided crossings adiabatically. This results in a very high ionization rate at the classical saddle point $(16n^4)^{-1} E_h$, or $6.12\sqrt{F}$ cm $^{-1}$.

A field of strength F in V cm $^{-1}$ will ionize states down to $3.06\sqrt{F}$ cm $^{-1}$ below threshold diabatically and those down to $6.12\sqrt{F}$ cm $^{-1}$ below threshold adiabatically. We need therefore at most only perform calculations between $6.12\sqrt{F_{\text{sluice}}}$ cm $^{-1}$ and $3.06\sqrt{F_{\text{disc}}}$ cm $^{-1}$ below threshold.

5.2 Theory

A fanciful zero-order model of threshold spectroscopy might assume that:

(i) The populations of the threshold states, which are at the Hund's case (d) limit, reflect the zero-quantum-defect transition moments from the initial state.

(ii) The field ionization process does not mix the zero-order states.

(iii) The lifetimes of the threshold states scale with the principal quantum number as n^3 .

However:

(iv) The presence of a quantum defect affects the relative transition moments from the initial state to the final channels.

(v) Multipole moments on the ion core mix the zero-order channels. For example, the dipole mixes channels with $\Delta\ell = \pm 1$. This effect is seen chiefly in the appearance of 'forbidden' peaks in the ionization spectrum. The chief requirement for a symmetry-allowed dipole coupling between two zero-order channels is that at least one interloper state coincide with the threshold-ionization range. Gilbert and Child [52] show that for rotational ionization in H_2O , this condition is fulfilled. For molecules with smaller rotational constants (this is almost all molecules), the density of interloper states is much higher.

(vi) Stark fields induced by the laser, and by adjacent ions, dilute the zero-order ‘doorway’ states amongst long-lived channels with high angular momentum ℓ . This has a greater effect on the lifetimes of states than on the presence of ‘forbidden’ peaks.

If we take point (iv) into account, then point (v) argues that ZEKE/MATI spectra can be used to probe interactions between electronic channels, or to illuminate the electronic contributions to more general interactions in other spectroscopies.

The measured ionization signal in a ZEKE/MATI experiment comes from what is a closed channel at zero field. We assume that the populations of the high- n Rydberg states stay constant before the ionization process. However, it is not possible to perform an all-channels-closed calculation for energies above the threshold of the lowest-energy channel $|1\rangle$ in the system, as β_1 becomes imaginary. For this reason, Dickinson *et al.* [89, 92], in their treatment of ammonia, treat the pseudocontinuum, the dense collection of states just below threshold, as an actual continuum and calculate the partial ionization cross-section into the newly-open part of a channel with a threshold artificially lowered by 10 cm^{-1} or so. This is the approach we shall use. To resolve the bluest peaks we need a step size of $\sim 10^{-4}\text{ cm}^{-1}$. We smooth the high- n Rydberg series by binning the intensities over a coarse mesh of 0.1 cm^{-1} . This should distinguish the smooth lineshape of a direct peak

from the more complicated structure due to interloper peaks. A realistic ZEKE/MATI lineshape could also be added. Where there are two thresholds close together, both are lowered but the partial ionization cross sections are calculated separately. This situation does not arise in refs. [89] and [92].

The ns and np quantum defects pose a particular problem, since there are no lines in the spectral range treated in ref. [38] that can be unambiguously assigned to an ns or np state. They appear to be predissociated on a timescale faster than that of experiment throughout most of the spectrum. The only known s and p states are those below $93\,000\text{ cm}^{-1}$. In the two-photon spectra of ref. [38], some unassigned bands at $88\,200$ and $89\,300\text{ cm}^{-1}$ are reported. This spacing is roughly that of the bending motion in water. The position would correspond to a quantum defect of roughly 1.16, which suggests it may be the hitherto unseen $4p\ ^1A_2$ state. The multireference configuration-interaction (MRD-CI) predictions of Theodorakopoulos *et al.* [93] have its band origin at $88\,200\text{ cm}^{-1}$. Why have these lines not been observed before? Ashfold and co-workers have taken $(3 + 1)$ resonance-enhanced multiphoton ionization (REMPI) spectra between $84\,000$ and $88\,000\text{ cm}^{-1}$ [94] and above $88\,400\text{ cm}^{-1}$ [95], but not in between. The one-photon spectra reported in Gilbert *et al.* [63] and Mayhew [78] cover some of the range, but any lines found are assignable as d lines. This is not surprising, as the $p \leftarrow p$ transition is dipole forbidden. The $4p\ ^1B_1$ homologue of the \tilde{C} state at near $91\,800\text{ cm}^{-1}$

Table 5.1: Equilibrium diagonal quantum defects used in the ZEKE–MATI calculations. $\mu_{s\Sigma^+}$ and $\mu_{p\Pi^+}$ are from Child [97], $\mu_{p\Pi^-}$ from Bell [98], $\mu_{p\Sigma^+}$ is assigned to the mystery state in ref. [38], and the μ_d from ref. [36].

λ^{p_e}	ℓ		
	s	p	d
σ^+	1.4856	1.16	0.135 63
π^+	—	0.6818	0.704 07
π^-	—	0.647	0.088 79
δ^+	—	—	-0.007 13
δ^-	—	—	-0.006 75

has been reported by Ishiguro *et al.* [96] but not rotationally-resolved before Dickinson *et al.* [38]. Table 5.1 compiles the equilibrium diagonal quantum defects used and their sources.

A possible approach, that could be combined with the method above and that we shall mention in passing, is the construction of the \mathbf{K} matrix entirely in Hund’s case (d). If we replace the case (b) expressions for the angular matrix elements $\langle \ell' \lambda' | C_{kq} | \ell \lambda \rangle$ with their case (d) analogues

$$\begin{aligned}
\langle N^{+'} K^{+'}, p' | C_{kq} | N^+ K^+, p \rangle &= (-1)^{J+K^{+'}+k} \left(1 + (-1)^{k+p+p'+\ell+\ell'} \right) \\
&\times \left[\frac{(2N^{+'} + 1)(2N^+ + 1)(2\ell' + 1)(2\ell + 1)}{4(1 + \delta_{K^{+'}0})(1 + \delta_{K^+0})} \right]^{1/2} \begin{Bmatrix} \ell & \ell' & k \\ N^{+'} & N^+ & J \end{Bmatrix} \\
&\times \begin{pmatrix} \ell' & k & \ell \\ 0 & 0 & 0 \end{pmatrix} \left[\begin{pmatrix} N^+ & k & N^{+'} \\ K^+ & q & K^{+'} \end{pmatrix} + (-1)^{N^{+'}+p'+\ell'} \begin{pmatrix} N^+ & k & N^{+'} \\ K^+ & q & -K^{+'} \end{pmatrix} \right].
\end{aligned} \tag{5.1}$$

From this follow the case (d) selection rules:

$$\Delta p = k + \Delta \ell, \quad \Delta \ell = \Delta N^+ = k = J, \quad \Delta K^+ = q. \tag{5.2}$$

Table 5.2: MATI peaks recorded from the (000) vibrational level of water in ref. [38], in order of magnitude (greatest first). Peaks forbidden by eqn. (3.19) appear in italics

Initial state	$J''_{K''_a K''_c}$	Peaks	Fig. ref.
\tilde{C} , <i>ortho</i> levels	1 ₁₁	1 ₁₁ , 2 ₀₂ , 0 ₀₀ , 2 ₁₁ , 3 ₁₃ /2 ₂₀ , 3 ₂₂ /4 ₀₄	5.1(a)
	3 ₂₂	3 ₁₃ /2 ₂₀ , 2 ₁₁ , 3 ₂₂ /4 ₀₄ , 2 ₀₂ <i>1₁₁</i> , 3 ₃₁ /4 ₂₂ , 4 ₃₁ /5 ₂₄ , 0 ₀₀	5.1(b)
	2 ₂₀	1 ₁₁ , 3 ₁₃ /2 ₂₀ , 2 ₁₁ , 2 ₀₂ , 3 ₂₂ /4 ₀₄ , 0 ₀₀ , 3 ₃₁ /4 ₂₂	5.1(c)
\tilde{C} , <i>para</i> levels	1 ₁₀	1 ₀₁ , 2 ₁₂ , 1 ₁₀ , others	5.2(a)
	2 ₂₁	1 ₀₁ , 2 ₁₂ , 2 ₂₁ , 3 ₂₁ /4 ₁₄ , 3 ₀₃ , 3 ₁₂	5.2(b)

Unlike the diagonal situation described by Jungen and Miescher [37], there is not necessarily an obvious physical interpretation for the Fano eigenchannels.

5.3 Results and discussion

Table 5.2 lists the peaks recorded by Dickinson *et al.* [38], in decreasing order of intensity. The peaks disfavoured by the propensity rule $|N^+ - J''| \leq \ell''$ are marked in italics. Compare the calculated spectra shown in Figs. 5.1 and 5.2. The spectra were calculated with the s, p, and d states described above, and with the f states modelled with the LRFM parameters fitted in chapter 4. No $\Delta\ell \neq 0$ couplings were included.

The first matter is Vrakking's suggestion [99], based on his and Lee's work on nitric oxide, that the laser field (and indeed the discrimination field) may enhance the dipole coupling between, for example, *np* and *nd* threshold

Figure 5.1: Calculated MATI spectra of H₂O recorded *via ortho* rotational levels of the $\tilde{C}(000)$ state. $J''_{K''_a K''_c} =$ (a) 1₁₁, (b) 3₂₂ and (c) 2₂₀.

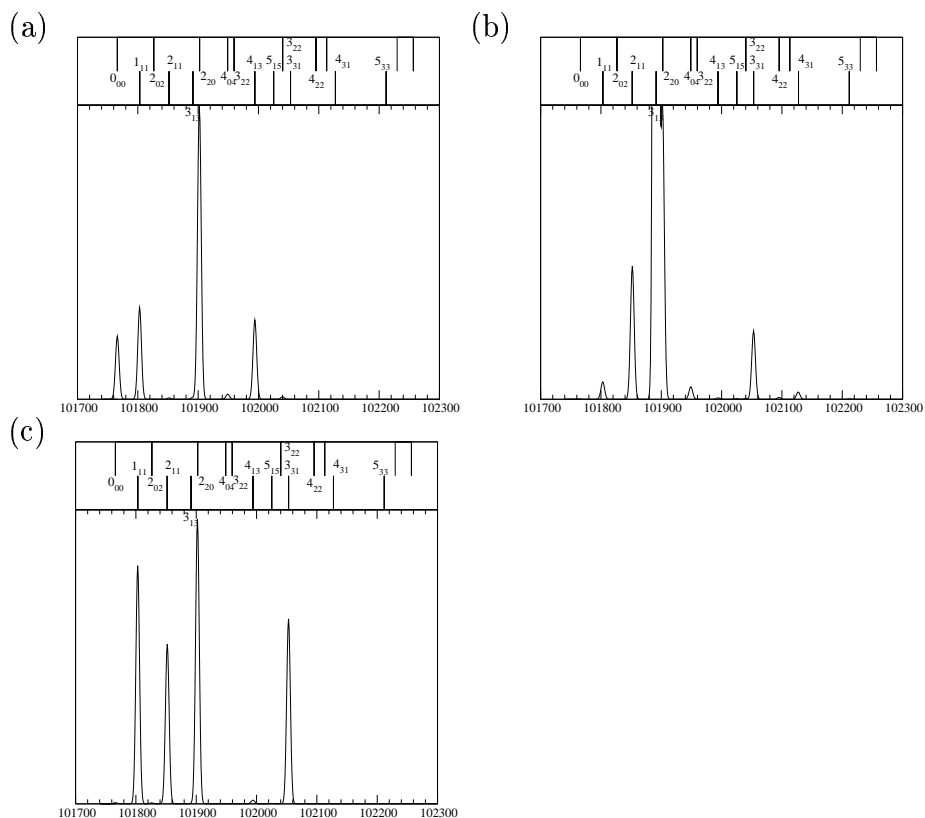
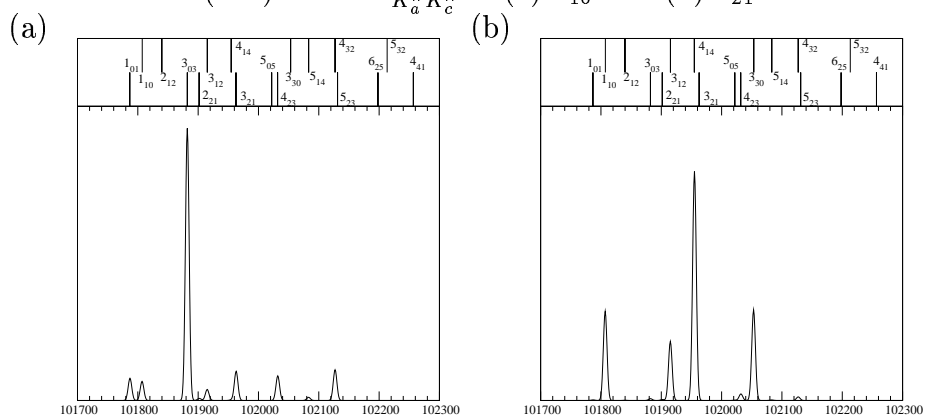


Figure 5.2: Calculated MATI spectra of H₂O recorded *via ortho* rotational levels of the $\tilde{C}(000)$ state. $J''_{K''_a K''_c} =$ (a) 1₁₀ and (b) 2₂₁



channels in water. For the asymmetric top the Stark effect parity rules, those of the electric field, are the same as for the dipole moment [32]

$$\Delta J = 0, \pm 1 \quad (J = 0 \leftrightarrow J = 0), \quad \Delta p = \Delta p^* = \pm 1. \quad (5.3)$$

These couple channels in different parity blocks together, and a test for a significant Stark effect will be peaks from the ‘wrong’ parity block in the MATI spectra. Table 5.3 compares the ‘direct’ and ‘Stark’ parity blocks. Vrakking’s proposed Stark enhancement will only be a weak effect, because it is the second-order Stark coupling that leads back to the original p and p^* , rather than the first-order as in NO. The suggestion is based on his observations of Stark-induced intrachannel f–g coupling. The nf and ng quantum defects are very close, and the effective principal quantum numbers for the coupling channels are therefore almost identical. For a $\Delta\ell = \pm 1$ transition, this leads to radial dipole moments that scale as n^2 . However, interchannel nf – nd or nd – np couplings will have a Δn of at least 30 or 40, and we have seen earlier that, far from scaling as n^2 , the radial dipole moments will scale as $\simeq \Delta n^{-3/2}$. Therefore we conclude that the Stark couplings for nf – nd and nd – np interactions will be vanishingly small, and this is borne out by comparing Tables 5.2 and 5.3.

Now we can consider the ‘forbidden’ peaks. Those with $|N^+ - J''| = \pm 2$

Table 5.3: Parity blocks used to model the MATI experiments. *ortho* levels have $p_r = 0$, *para* $p_r = 1$. The blocks labelled Stark are those accessible in first order from the direct blocks according to the selection rules in eqn. (5.3).

Initial state	$J''_{K''_a K''_c}$	$\{J', p', p^{*f}\}$	
		Direct	Stark
\tilde{C} , <i>ortho</i> levels	1 ₁₁	{0-2, 0, 0}	{0-3, 1, 1}
	2 ₂₀	{1-3, 0, 1}	{0-4, 1, 0}
	3 ₂₂	{2-4, 0, 1}	{1-5, 1, 0}
\tilde{C} , <i>para</i> levels	1 ₁₀	{0-2, 1, 1}	{0-3, 0, 0}
	2 ₂₁	{1-3, 1, 0}	{0-4, 0, 1}

are clearly visible in both the *ortho* and *para* spectra, showing that they are accounted for by the frame transformation. The $|N^+ - J''| = -3$ peak in the $J''_{K''_a K''_c} = 3_{22}$ spectrum is unfortunately absent, but should appear if we treat the long-range effects properly, as it will be mixed with $|N^+ - J''| = -2$ interloper states. The full treatment should also provide nominally-allowed lines that are currently absent or very weak in the simulation, but present in experiment, such as the 2₁₁ line in the $J''_{K''_a K''_c} = 1_{11}$ spectrum.

5.4 Conclusion

The purpose of this chapter has been to explore, by comparing theory and experiment, threshold ionization processes in the water molecule. We have looked at the mixing induced by the long-range properties of the ionic core, the Stark effect induced by the weak electric fields present in the ZEKE and

MATI experiments, and the mixing of ionic states caused by the short-range interaction with the Rydberg electron, and shown that Vrakking's suggested electric field contribution to the threshold dynamics is small. MQDT calculations have shown that some, but not all, of the 'forbidden' lines described by Dickinson *et al.* become 'allowed' when we apply a full mixed case (b)–case (d) treatment incorporating the frame transformation. Other lines, including those allowed by the propensity rule but not visible in the present calculations, will require the $\Delta\ell = \pm 1, \pm 2$ couplings implied by a full LRFM treatment.

Chapter 6

Photoelectron spectroscopy of water

This, unlike the MATI spectroscopy described above, provides information about vibrational autoionization, and hence about the off-diagonal elements of the vibrational reactance matrix $K_{vv'}$. This is calculated by integrating the quantum-defect surface with the vibrational wavefunctions [33, 34] over all vibrational coordinates (eqn. (3.22)). The photoelectron spectra of water measured by Glab and reported below are of particular interest. There has been very little work done on vibrational autoionization from bent triatomic molecules. Grant and co-workers have studied the resonant ionization and ZEKE spectra of the s, p and d states of linear NO₂ [90, 100–102] and HCO [103–107] but not their photoelectron branching ratios. Finally, Pratt [108]

has recently measured the branching ratios from the B $^1E''$ state of ammonia with photoelectron spectroscopy. Further, because they are taken from the relatively non-penetrating nf series of the water molecule, Glab's spectra provide the opportunity to explore how the changes in long-range properties of the ionic core with changing geometry influence the autoionization process.

6.1 Experiment

The experiment is described in detail in Glab *et al.* [109]. Time-of-flight electron kinetic energy spectra are gathered for H₂O ionized by a $2 + 1'$ -photon process *via* the (100) vibrational level of the $\tilde{C} 3p^1B_1$ Rydberg state in a 1 T magnetic bottle spectrometer with a resolution of 28 cm^{-1} and a collection efficiency of around 50%. The electrons, which ionize into the (000) level of the ion with energies around 3000 cm^{-1} , were accelerated into the collection tube by a potential of around -0.5 V . No measurements were taken beyond about 400 cm^{-1} of ionic internal energy, which means that any signals from electrons ionizing into the (010) level (ionization threshold 103174 cm^{-1}) were not recorded. Water vapour at a pressure of the order of 10^{-5} Torr was pumped through the interaction region.

The pump laser for the two-photon $\tilde{C} \leftarrow \leftarrow \tilde{A}$ transition was frequency-doubled in a BBO crystal and produced approximately $50 \mu\text{J}$ per pulse of

light at around 239 nm. The second dye laser, which was tunable in the range 546–556 nm, produced $2\ \mu\text{J}$ per pulse of light. Fig. 6.1 shows the excitation and ionization processes schematically.

The spectra themselves were originally calibrated, as in ref. [109], by waiting for the first peak or shoulder and assigning that to the 0_{00} state. This assignment is often confirmed by the rotational spacings of the H_2O^+ (100) level, but in some cases it has had to be changed.

6.2 Theory

Using the nd quantum defects from Child and Glab [36], and the f quantum defects, d - f and p - d couplings determined from the long-range-force model, the MQDT code then provides partial ionization cross sections at the energies of interest. These are plotted against the threshold energies of the channels with a Gaussian lineshape applied to mimic the detector, and the results are shown along with the experimental data. The couplings between vibrational levels are taken to be proportional to the diagonal quantum defects. As we shall see below, this is reasonable for the (100)–(000) case.

A more sophisticated MQDT–LRFM approach, and one that is not so dependent on fitting, is to use molecular parameters derived from experiment or *ab initio* calculations. As I am unaware of any such experiments on the

Figure 6.1: Experimental scheme for photoelectron spectroscopy of Rydberg water (not to scale).

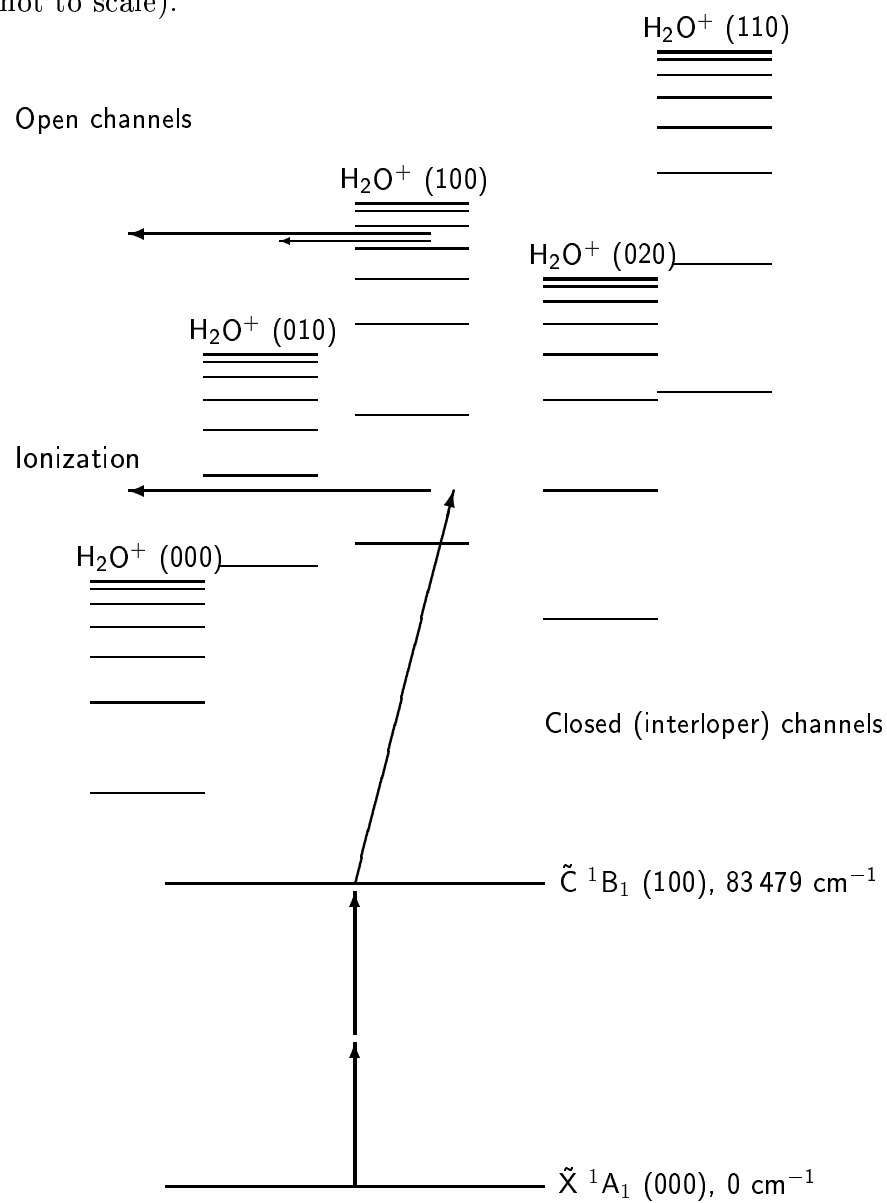
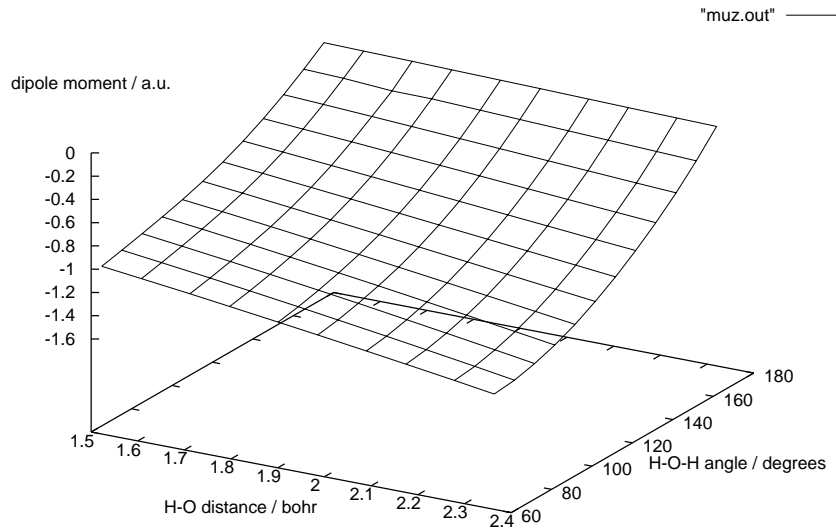


Figure 6.2: Dipole moment surface $\mu(\mathbf{Q})$ calculated *ab initio* for the water ion.



ion, or indeed calculations other than the dipole surface provided by Weis *et al.* [110], as a test of principle we perform single-point B3LYP/6-311+G** [82–85] calculations using code by Frisch *et al.* [86] to provide the multipole moments and polarizabilities of the water ion over a range of values for the bend (θ) and symmetric stretch ($\Delta R = R - R_{\text{eq}}$) coordinates, both of which have A_1 symmetry in C_{2v} . The dipole moment, quadrupole moment and polarizability surfaces are shown in Figs. 6.2–6.4.

We use singular value decomposition (SVD) to expand the 120-point sur-

Figure 6.3: (Above) Quadrupole moment surface $[Q_{xx}(\mathbf{Q}) - Q_{yy}(\mathbf{Q})]$ and (below) quadrupole moment surface $Q_{zz}(\mathbf{Q})$ calculated *ab initio* for the water ion.

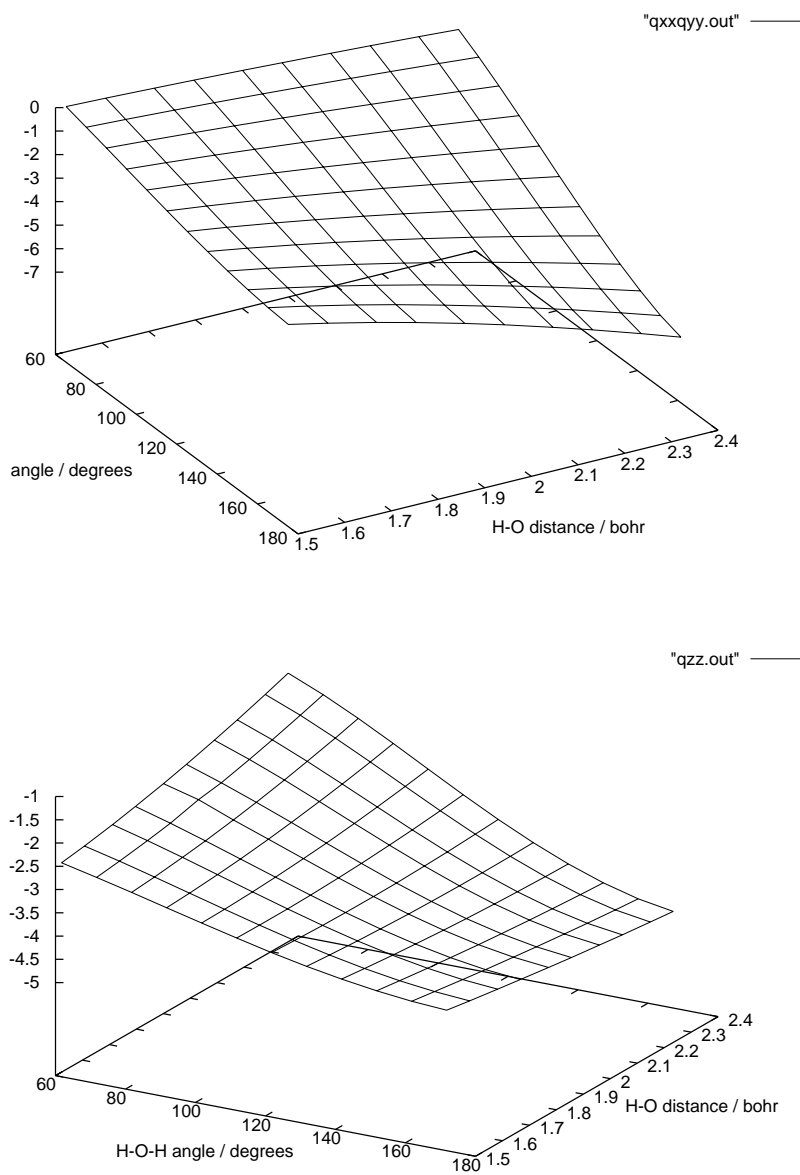


Figure 6.4: *Ab initio*-calculated anisotropic polarizability surface $\alpha(\mathbf{Q})$ for the water ion.

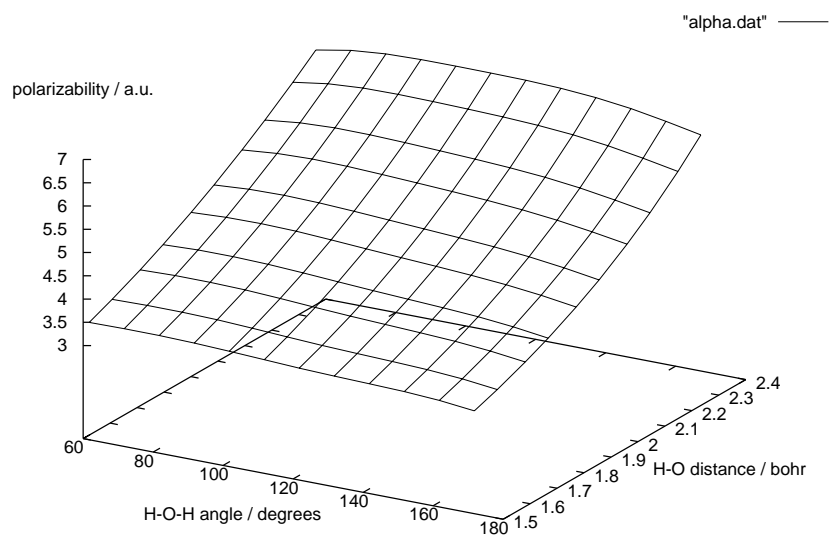
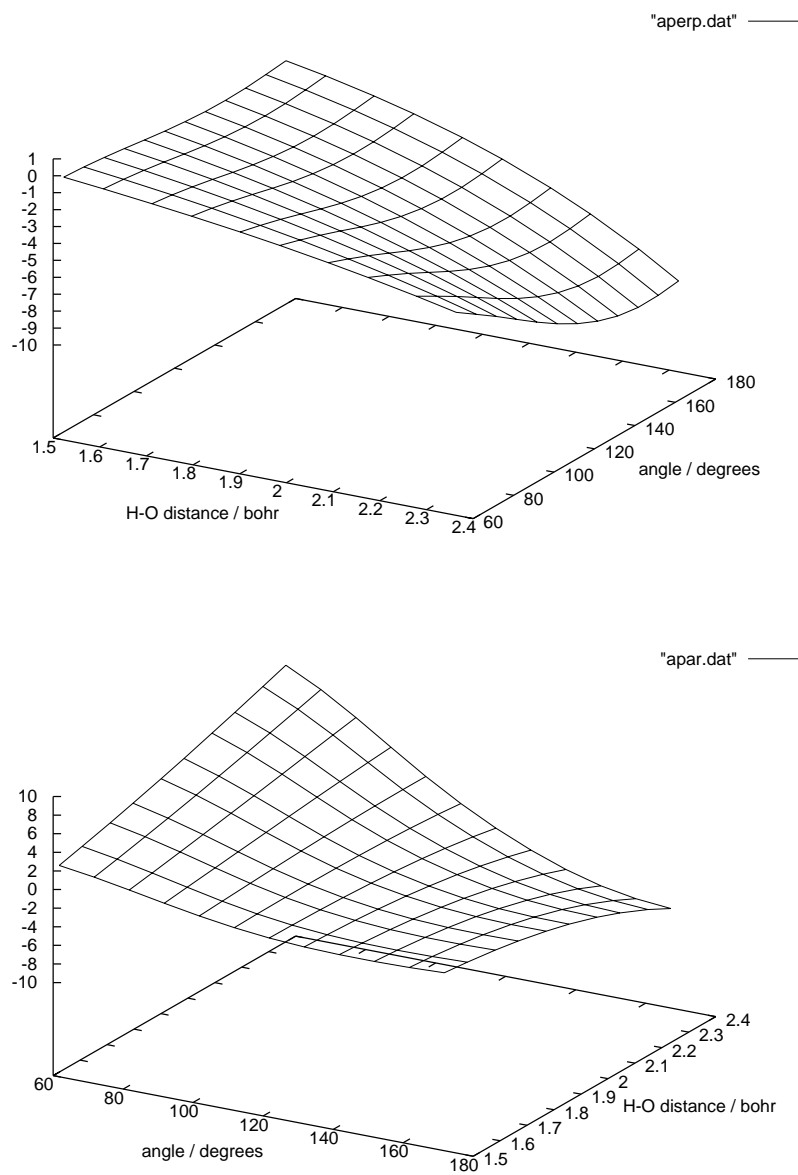


Figure 6.5: *Ab initio*-calculated (above) $[\alpha_{xx}(\mathbf{Q}) - \alpha_{yy}(\mathbf{Q})]$ and (below) $[2\alpha_{zz}(\mathbf{Q}) - \alpha_{xx}(\mathbf{Q}) - \alpha_{yy}(\mathbf{Q})]$ anisotropic polarizability surfaces for the water ion.



faces in

$$\sum_{ij} C_{ij} (\Delta R)^i \cos^j \theta. \quad (6.1)$$

These expressions for the long-range properties of the ionic core can then be combined with the long-range-force equations listed above to produce quantum-defect functions $\mu_{(Q)}$. We then use code by Child [97] to produce the full short-range reactance matrix $K_{\alpha v, \alpha' v'}$ using eqn. (3.22), the H_2O^+ potential energy surface from Brommer *et al.* [111] and the Hamiltonian from Carter *et al.* [112].

The reactance matrices for $v_1 = 0-2$ and $v_2 = 0-2$ are listed in full in an Appendix. Table 6.1 lists the reactance matrix elements that couple the (100) level to ionization and interloper channels for different $n\ell\lambda^{p_e}$ states in the III^{F} representation, which is transformed into the I^{F} representation by the code. The most eye-catching feature is that, for all electronic states, the strongest coupling from the (100) level is not to the ground (000) level but to the interloper (110) level. It is perhaps to be expected from the diatomic vibrational ionization propensity rule $\Delta v = 1$ that the strongest coupling will be the one that involves the smallest change in vibrational energy. This is not an unknown phenomenon: the NO_2 ionization spectra of Campos *et al.* [100] show four window resonances which are tentatively assigned to interactions with the (110) state. They have FWHM of 100, 100, 70 and 20 cm^{-1} and have

effective principal quantum numbers of 9.4, 10.4, 11.4 and 12.4 respectively.

That the $\Delta v_2 = \pm 1$ coupling is particularly strong even for the $f\delta^\pm$ states is surprising if we think of molecular vibrations as harmonic oscillators, given that $\mu_{f\delta^\pm}$ is proportional to the polarizability alone, and Fig. 6.4 shows that α depends chiefly on the stretch and only very slightly on the bend. Less surprising is that $f\pi^+$ and $f\pi^-$, which are strongly split by the quadrupolar and polarizability terms of $C_{22} + C_{2,-2}$ symmetry, show a very large $\Delta v_2 = \pm 1$ coupling, and almost equal (100)–(000) and (100)–(010) values. The $\Delta v_1 = 0$ ionizations are even more disfavoured for the off-diagonal σ – δ and π – ϕ couplings.

Table 6.1: Reactance matrix elements coupling the (100) level to ionization and interloper channels ($v_1v_2v_3$). The top row is the diagonal $K_{(100),(100)}$ element.

		Threshold/cm ⁻¹		Electronic state				Couplings			
		Experiment	Theory [111]	f σ^+	f π^-	f π^+	f δ^\pm	f ϕ^\pm	f $\phi-f\pi$	f $\sigma^+-f\delta^+$	
	(100)	33100	3215.87	0.09980	0.13225	0.02486	0.01413	-0.09287	-0.01161	-0.01639	
	Ionization channels										
	(000)	0.00	0.00	-0.00153	0.00099	-0.00139	-0.00018	0.00151	0.00003	0.00004	
94	(010)	8400	1412.15	-0.00012	0.00097	-0.00111	0.00006	0.00028	-0.00019	-0.00027	
	Interloper channels										
	(020)	2771.27	2777.97	0.00008	-0.00014	0.00023	-0.00005	-0.00020	0.00000	0.00000	
	(110)	4593	4604.56	0.00190	-0.01235	-0.00919	0.00020	-0.00191	-0.00241	-0.00340	
	(120)	5936	5947.92	0.00024	0.00114	0.00134	-0.00020	-0.00077	0.00018	0.00025	
	(200)	6280	6304.18	0.00174	0.00085	0.00185	0.00021	-0.00170	0.00003	0.00004	
	(210)	7639	7667.33	-0.00063	-0.00102	0.00006	0.00000	0.00079	0.00018	0.00025	
	(220)	—	—	-0.00006	0.00006	-0.00013	0.00002	0.00013	-0.00003	-0.00004	

6.3 Results

The simplest case occurs for transitions from the $J''_{K''_a K''_c} = 0_{00}$ rotational level of the \tilde{C} state, which can only be of R-type. We shall therefore concentrate on the 0_{00} lines first. The photoelectron spectra are shown in Fig. 6.6 and referenced according to the notation in Table 6.2. The $nf2_{02}$ series of spectra, GCP3 (not shown, Fig. 3 in Glab *et al.* [109]), **63** and **57** should be straightforward. They form a well-defined case (d) series, and calculations show a strong 2_{02} line and little else. However, they, and the as-yet-unassigned **61** shown a distinctive head-and-shoulders $0_{00}-2_{02}-2_{20}$. This is even more surprising when we consider that the calculated spectrum for **61** shows a strong 3_{13} line, which is evidence of d character. Mercifully, the assignment seems to be correct for **64**, which is reasonably similar to the calculation. The overall agreement is disappointing, considering the success of the method so far in dealing with the wavelength spectra, but we note that as most of the lines considered are above the (010) threshold, ionization into the bend is a competing pathway.

The $J''_{K''_a K''_c} = 1_{11}$ spectra are listed in Table 6.4 and shown in Fig. 6.7. Only for **1** do experiment and calculation approach one another—in **2**, **4** and **6** there is more structure than the calculation predicts.

The spectral assignment is somewhat more difficult, because we now have

Table 6.2: Synopsis of photoelectron spectra recorded by Glab from the 0_{00} level of the \tilde{C} state.

Label	Wavenumber/cm ⁻¹	Case (d) composition	Assignment
GCP3	101969	$2_{02}, 2_{20}/3_{13}, \text{sh } 0_{00}$	$6f2_{02}$
61	103592.0	$0_{00}, 2_{02}, 2_{20}$	^a
64	103686.7	$1_{11}, \text{weak } 2_{11}, 3_{13}, 0_{00}$	9d
63	103940.0	$0_{00}, 2_{02}, 2_{20}$	$10f2_{02}$
55	103951.7	$2_{20}, 1_{11}, 2_{02}, 2_{11}, 0_{00}$	^a
66	104069.4	$3_{22}/4_{04}, 3_{13}$	$10f3_{22}/4_{04}$
57	104132.1	$0_{00}, 2_{02}, 2_{20}$	$11f2_{02}$

^a Not assigned in ref. [36].

Figure 6.6: 0_{00} photoelectron spectra. (a) **61** (b) **64** (c) **63** (d) **55** (e) **57** (f) **66**. The ionic energy is referred to the $(000) 0_{00}$ ground state of the water molecule, for easy comparison with the rotational channel thresholds listed in Table 6.3. Solid lines: experiment. Dashed lines: calculation.

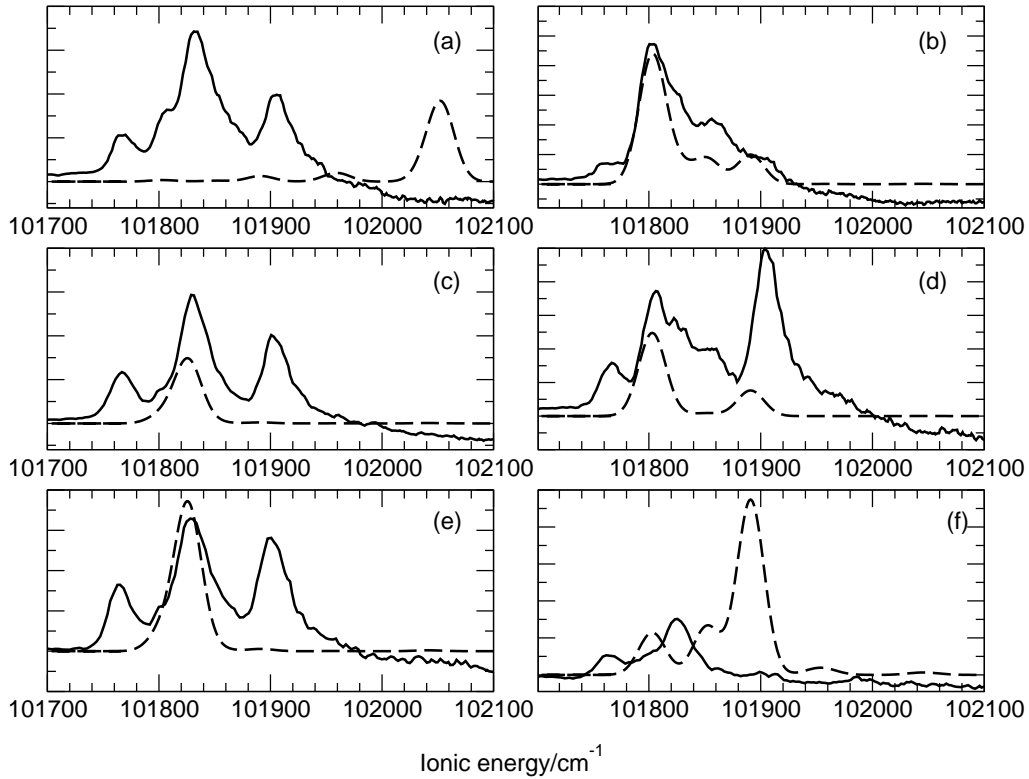


Table 6.3: Rotational ionization thresholds for the (000) level of H_2O^+ . The left-hand pair of columns apply to even- ℓ channels for the 0_{00} and 2_{02} spectra and the right-hand pair of columns to odd- ℓ channels. For the 1_{11} spectra the situation is reversed.

$N_{K_a^+ K_c^+}^+$	Threshold/cm $^{-1}$	$N_{K_a^+ K_c^+}^+$	Threshold/cm $^{-1}$
0_{00}	101766.0	1_{11}	101803.3
2_{02}	101826.5	2_{11}	101851.7
2_{20}	101902.2	3_{13}	101891.5
4_{04}	101948.9	3_{31}	102053.2
3_{22}	101959.7	—	—
4_{22}	102040.4	—	—

overlapping P, Q and R branches. **3**, for example, is a problem. If we take the shoulder at the left-hand end of the spectrum as zero, then we have a pronounced peak visible from the 4_{13} channel, which is closed at 101977 cm^{-1} . Recalibrating the broad peak to the 1_{11} energy lets us assign the other two peaks to 3_{13} and 4_{04} , of which only 4_{04} matches the d assignment or the pure d calculation.

There is a more severe problem with **5**, which appears to be too broad. If we shift the experimental spectrum 60 cm^{-1} to the blue, in order that the blue end of the first hump line up with the calculated spectrum, then the peak at the right-hand end of the spectrum ends up belonging to a closed channel. As it stands, there is rather too much signal to the red of 0_{00} .

The $J_{K_a'' K_c''}'' = 2_{02}$ lines are listed in Table 6.5 and shown in Figs. 6.8 and 6.9. **2.1** appears at first too simple for a d line, but the peak breadth suggests that it consists of at least three lines, of which theory predicts two. It

Table 6.4: Synopsis of photoelectron spectra recorded by Glab from the 1_{11} level of the \tilde{C} state.

Label	Wavenumber/cm ⁻¹	Case (d) composition	Assignment
1(GCP1)	101847	$0_{00}, 2_{02}$	$6d, J' = 0$
2(GCP2)	101967	$1_{11}, 3_{13}, ?$	$6f1_{11}, J' = 2$
3	101977	See text	{200} 6d
4	102013	$1_{11}, 2_{11}, 3_{13}, 4_{13}$	$6f2_{11}, J' = 2$
6	102067	???	$6d^a$
7	102081	$2_{02}, 2_{20}, 4_{22}$	$6d, J' = 1$

Figure 6.7: Selected 1_{11} photoelectron spectra. (a) **1** (b) **2** (c) **3** (d) **4** (e) **6** (f) **7**. Conventions as in Fig. 6.6.

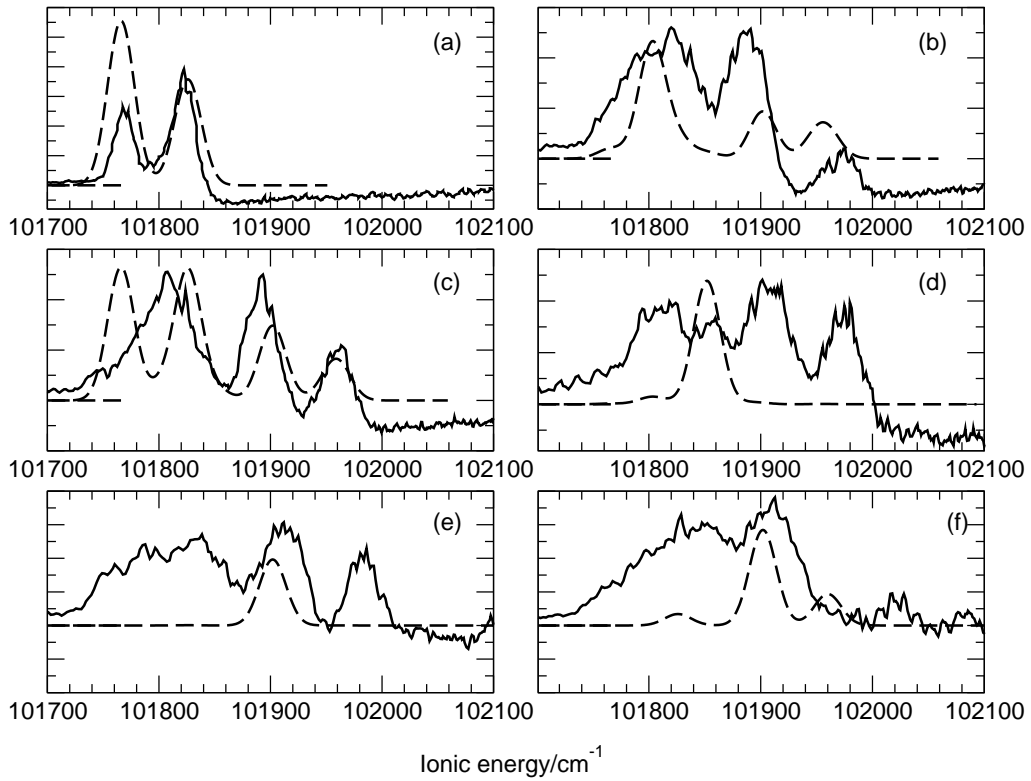


Table 6.5: Synopsis of photoelectron spectra recorded by Glab from the 2_{02} level of the \tilde{C} state.

Label	Wavenumber/cm ⁻¹	Case (d) composition	Assignment
2.1	101879	$1_{11}, 2_{02}, 2_{11}$	$6d\sigma + 1_{11}$
2.2	101920	$1_{11}, 2_{20}$	$6f0_{00}, J' = 3$
2.3	101981.5	$2_{11}, 3_{13}, 4_{13}$	$6d, J' = 2$
2.4	101995	$2_{02}, 2_{20}, 4_{13}$	$6f2_{02}, J' = 3$
2.5	102025	?	$6d^a$
2.6	102030	$2_{02}, 3_{13}, 4_{04}$	$6d^a$
2.7	102049.3	$2_{02}, 2_{20}, 4_{04}, 6_{06}$	$6f2_{20}, J' = 3$
2.8	102073.7	$1_{11}, 4_{04}, 4_{13}, 3_{31}$	$6d, J' = 3$
2.9	102080.6	$1_{11}, 2_{11}$	$6d, J' = 2$
2.10	102095.8	$1_{11}, 3_{13}, 4_{04}, 5_{13}$	$6d, J' = 3$
2.11	102103.5	$2_{20}, 4_{04}$	$6f4_{04}, J' = 1$
2.12	102125.7	$0_{00}, 2_{11}, 3_{22}, 5_{13}$	$6f3_{22}, J' = 1$

^a Not listed in ref. [36].

is hard to align **2.5** with any known ionization threshold, and the calculated spectrum is no help. The general theme of theory predicting fewer lines than in experiment is borne out by the remaining spectra, but there is no discernible pattern.

6.4 Discussion

Clearly the long-range-force parameters obtained by fitting and the implied d-f, p-d and p-f mixings are insufficient to the task. What about the more sophisticated *ab initio* method detailed above? Unfortunately there was not enough time to incorporate its results within the MQDT code, but some general observations can be made. Firstly, the strong coupling to the (110) level

Figure 6.8: 2_{02} photoelectron spectra **2.1–2.6**. Conventions as in Fig. 6.6.

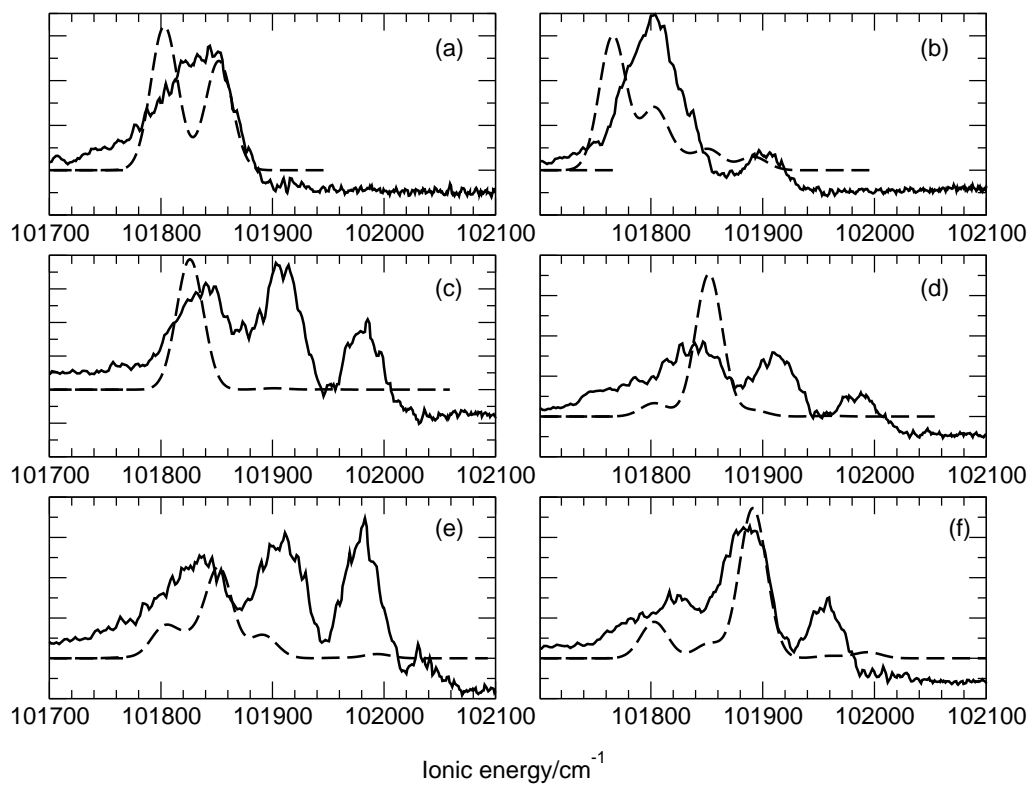
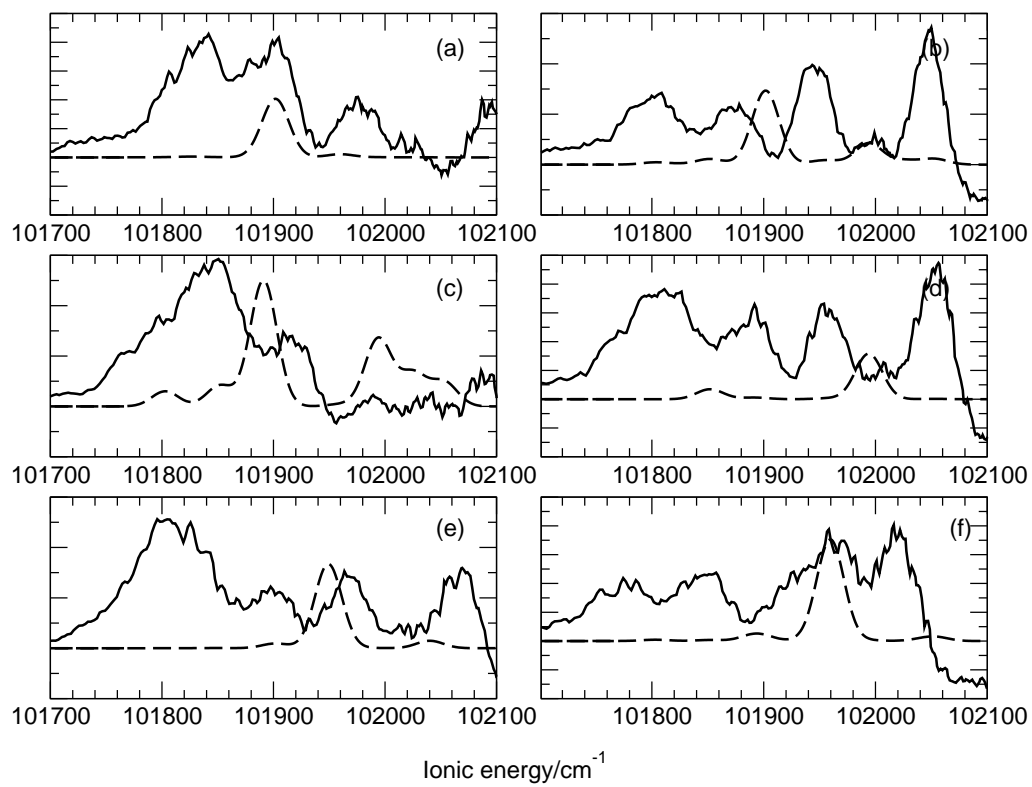


Figure 6.9: 2_{02} photoelectron spectra **2.7–2.12**. Conventions as in Fig. 6.6.



is unlikely to account for all of the anomalous distributions, because its effects are transmitted through lower- n interloper levels. The (110) 5f states will occur to the blue of $101\,970\text{ cm}^{-1}$, and the (110) 6f states to the blue of $103\,310\text{ cm}^{-1}$, with the 5d and 6d states spread around them. Secondly, while the $f\pi^\pm$ states ionize with equal efficiency into the (000) and (010) levels, this depletion is insufficient to account for the additional lines seen in the spectrum. Other possible causes need to be identified.

(i) Interaction with the asymmetric stretch. The multipole and polarizability surfaces have not yet been extended to the asymmetric stretch, though this is a possibility. The asymmetric stretch does not have A_1 symmetry, so would couple together different pairs of states from those described above. However, the magnitude of such couplings is unlikely to be much larger than those from the bend. Dinelli *et al.* [113] use the Birss resonance [114] to derive the rotational constants for the symmetric stretch of the water ion from those measured by microwave spectroscopy for the asymmetric stretch. It takes the general form

$$H^{\text{Birss}} = Z \left[\sqrt{\frac{1}{2}}(J_+ + J_-)J_z + J_z\sqrt{\frac{1}{2}}(J_+ + J_-) \right]. \quad (6.2)$$

Note that the Birss Hamiltonian mixes states of different core parity p^+ . This is because asymmetric top basis states $|N^+K^+, p^+\rangle$ are not, except

for $|N^+0, p^+\rangle$, eigenvalues of \hat{N}_z^+ . However, Dinelli *et al.* [113] find that $Z = 0.442$ and the resonance is therefore an insignificant perturbation of only a few wavenumbers.

(*ii*) Another possibility, first discussed by Giusti-Suzor and Jungen [29] for nitric oxide, is an indirect autoionization mechanism where predissociating states mix with the ionizing states. There is no reason why these couplings should not be stronger than the vibrational couplings and indeed dominate the ionization process. Detailed photoelectron spectra by Zare and co-workers [115, 116] of the Rydberg states of nitric oxide around $n = 15$ show unusual photoelectron distributions not unlike those discussed above. That predissociating states are involved has been demonstrated by Pratt [117] in his measurement of dissociation products in the same spectral region. Calculation of the ionization–dissociation branching ratios in this case has not yet, however, been attempted, though considerable effort has been expended in determining the Rydberg–valence couplings.

In water, the origin is unlikely to be valence states, which in any case are the \tilde{A} and \tilde{B} states much further down the spectrum, but instead Rydberg states belonging to the linear \tilde{A} state of the ion, or indeed the superbent \tilde{B} state. A full Renner–Teller treatment is beyond the scope of this thesis.

(*iii*) Zeeman and Stark coupling due to the 1 T field induced by the environment of the magnetic bottle spectrometer, and the resulting motional

Stark effect. If we assume an effective Stark field of 12 V cm^{-1} , then the calculations described in Appendix A show that at $n = 6$, the $6f2_{02}$ channel in the $J = 1$ manifold is mixed into the $6f2_{20}$ channel by about 3%. At $n = 11$, this mixing has not increased, but merely distributed across the higher- ℓ states.

Pratt [117] discusses the effect of the spectrometer on the 15f lines of nitric oxide. The magnetic field splitting, as seen in Table 9.3 (below), is about a wavenumber per tesla per m_ℓ . This widens each peak to about 6 cm^{-1} across, but is unlikely to affect the intensities.

6.5 Conclusions

The long-range-force model with parameters fitted to the photoionization spectra of Child and Glab has been applied to calculate vibrational autoionization branching ratios of photoelectron spectra for some nd and nf series in Rydberg water and been shown to be inadequate. A full vibrational autoionization long-range-force model has been constructed using *ab initio* multipole moment and polarizability functions, which demonstrates that the short-range electronic symmetries of states affect their vibrational autoionization dynamics. A full explanation of the photoelectron spectra shown awaits a Renner–Teller model for Rydberg water, and possibly more

experimental data.

Chapter 7

Rydberg wave-packet dynamics

Schrödinger attempted to construct electron wave packets in 1926 in order to understand what the quantum mechanical model of the hydrogen atom actually meant [118]. He had already constructed a harmonic oscillator wave packet [119] that he claimed would never run down. However, Lorentz pointed out that

A wave packet can hold together for some time only if its dimensions are large compared to the wave length. Since, however, the wave length... is of the order of magnitude of the Bohr elliptic orbit, there can be no question of having a wave packet that is small compared to the dimensions of such an ellipse... But if we take a wave packet as a model of the electron then by doing so we

block the way to restoring matters. Because it is indeed asking a lot to require that a wave packet should condense itself again once it has lost its shape.

Parker and Stroud [120] in 1986 were the first to suggest the investigation of Rydberg wavepackets. They calculated the power radiated by a Rydberg electron as it accelerates through the core region, a scheme which to the best of my knowledge has never been implemented experimentally. Averbukh and Perelman [121] considered the long-term evolution of an electron wave packet in a Coulomb potential and showed that, contrary to the expectations of Lorentz [118], a dispersed electron wave packet will revive at a time determined by the shapes of the wave packet and the potential. Alber *et al.* [122] then proposed a three-pulse photoionization method for detecting the evolution of Rydberg wavepackets. These have since been superseded by two techniques with very much better signal-to-noise ratios. Noordam *et al.* [123] showed that the optical Ramsey method could be used to determine the autocorrelation function $\text{Auto}(t)$ for a hydrogen atom, being proportional to the total Rydberg population excited by a pair of photons separated by time t , averaged over the Rabi oscillations. The autocorrelation function is the Fourier transform of the lineshape-adapted frequency-domain spectrum.

7.1 Theoretical background

The time evolution of a packet of discrete states ψ_n , each of energy E_n weighted by coefficients c_n is given by

$$\Psi(t) = \sum_n c_n \psi_n e^{-iE_n t}, \quad (7.1)$$

from which we obtain the time autocorrelation function

$$\text{Auto}(t) = \langle \Psi(t) | \Psi(t_0) \rangle = \sum_n |c_n \psi_n|^2 e^{-iE_n(t-t_0)} \quad (7.2)$$

through the orthogonality of ψ_n . For a real calculation, $c_n \psi_n$ is the product of the intensity of the exciting pulse $C(E_n)$ with the oscillator strength f_n of the transition. The zero width of the lines implies a wavepacket that will never leak away from the system, but instead disperse and revive indefinitely. In practice, one would convolute the lines with a detection function $d_{\text{Expt}}(E)$ to model the loss of coherence between the pump and probe photons, and a decay function $d_{\text{Ryd}}(E)$ which incorporates the effects of collisions, stray fields and radiative loss on the Rydberg electron, then replace the sum over states with an integral over energy. The envelope of the autocorrelation spectrum will be the Fourier transform of the product $d_{\text{Expt}}(E)d_{\text{Ryd}}(E)$.

For a continuum wavefunction Ψ_i we again replace the sum with an in-

tegral. The weighting $c_i(E)$ is a continuous function of the intensity of the exciting pulse and the partial cross section σ_i in channel i , so we can write

$$\langle \Psi_i(t) | \Psi_i(t_0) \rangle = \int C(E) \sigma_i(E) e^{-iE(t-t_0)} dE, \quad (7.3)$$

because the continuum wavefunctions are normalized to a delta function of energy $\delta(E - E')$. As the total cross section is an incoherent sum over open channels $\{P\}$:

$$\sigma(E) = \sum_{i \in P} \sigma_i(E), \quad (7.4)$$

the total autocorrelation function will be

$$\langle \Psi(t) | \Psi(t_0) \rangle = \int C(E) \sigma(E) e^{-iE(t-t_0)} dE, \quad (7.5)$$

which is the Fourier transform of the pulse-modulated cross section. In state-selected ionization experiments on molecular Rydberg states, direct excitation of the continua is Franck-Condon forbidden, and we can think of the spectrum as a set of lines corresponding to quasibound Rydberg states which have been convoluted with Fano profiles by the autoionization process. The envelope of the autocorrelation spectrum will now be the Fourier transform of the Lorentzian profile, which is an exponential decay. For the following calculations we will neglect $d_{\text{Expt}}(E)$ and assume that $d_{\text{Ryd}}(E)$ is dominated

by ionization.

Direct integration scales as $O(N^2)$ for N data points, while the fast Fourier transform (FFT) algorithm [80] scales as only $O(N \log_2 N)$. As typical calculations use $N \gg 2^{16}$ points, the savings in the FFT approach will be considerable. The mesh size determines the overall length of the spectrum in time for in atomic units, $\Delta t = 2\pi/\Delta E$. The atomic unit of energy is E_h ($219\,474.63\text{ cm}^{-1}$) and the atomic unit of time is (\hbar/E_h) $2.418\,884 \times 10^{-5}$ ps [124]. A mesh size of 1 cm^{-1} yields a total length of 32.99 ps, and one of 0.01 cm^{-1} 3.299 ns.

7.2 The Ramsey method

Ramsey's separated oscillating fields method first appears in 1949 [125]. The molecules in a beam pass through two or more spatially-separated fields: if they are in phase an absorption lineshape is recorded, if out of phase by $\pi/2$, we see a dispersive lineshape. This led to the invention of the atomic clock, except that usually in an atomic clock there is a single oscillating field which the atoms pass through twice, first upwards, and second downwards under gravity. The optical Ramsey method (ORM), involves the motion of the sample through a pair of fields being replaced with a stationary sample and a pair of pulses generated by splitting a single photon with a Michelson

or Mach–Zehnder interferometer.

Now, if as suggested in Noordam *et al.* [123], we have two well-separated pulses in the function $C(t)$, the amplitude a_n of the hydrogen Rydberg state is

$$a_n(t) = -ie^{-i\omega_n t} D_n \sqrt{\frac{\pi}{2 \ln 2}} \tau_p E_0 e^{-(\Delta_n \tau_p)^2 / 8 \ln^2} (1 + e^{-i\Delta_n \tau_d} e^{i\omega_L \tau_d}), \quad (7.6)$$

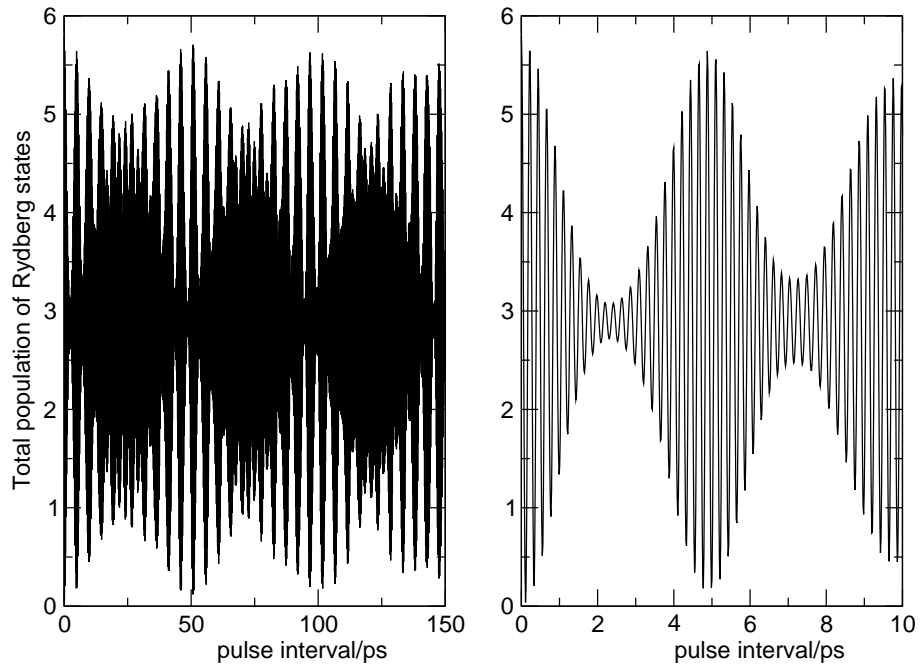
where $\Delta_n = \omega_L + \omega_1 - \omega_n$. If we take the square modulus to obtain the Rydberg population as a function of the delay between the pulses τ_d , we find that it is

$$P(\tau_d) = \sum_n P_n(\tau_d) \propto \sum_n 2 + 2 \cos[(\Delta_n - \omega_L) \tau_d], \quad (7.7)$$

which consists of a fast Rabi term ω_L , or Ramsey fringe, which depends on the mean frequency of the pulse, and a slow term Δ_n , which reflects the time evolution of the wavepacket. Eqn. (7.7) is the result on which the wavepacket experiments are based. Fig. 7.1 shows the total Rydberg population for an $s \rightarrow p(m_\ell = 0)$ transition.

Now assume that the two pulses are of arbitrary polarizations \mathbf{q}_1 and \mathbf{q}_2 . The bold face indicates that the polarizations include the parallel-polarized possibilities $C_{11} \pm C_{1,-1}$. The term in brackets in eqn. (7.6) will now depend explicitly on the combination of pulse polarizations. Further, the space-

Figure 7.1: Total Rydberg population against interval τ_p between first and second pulses. Left: the long-term revival structure superimposed on the Kepler recurrences. Right: the Kepler recurrences superimposed on the Rabi fringes, which are not shown to scale.



fixed projections of the electron angular momentum will acquire different populations according to

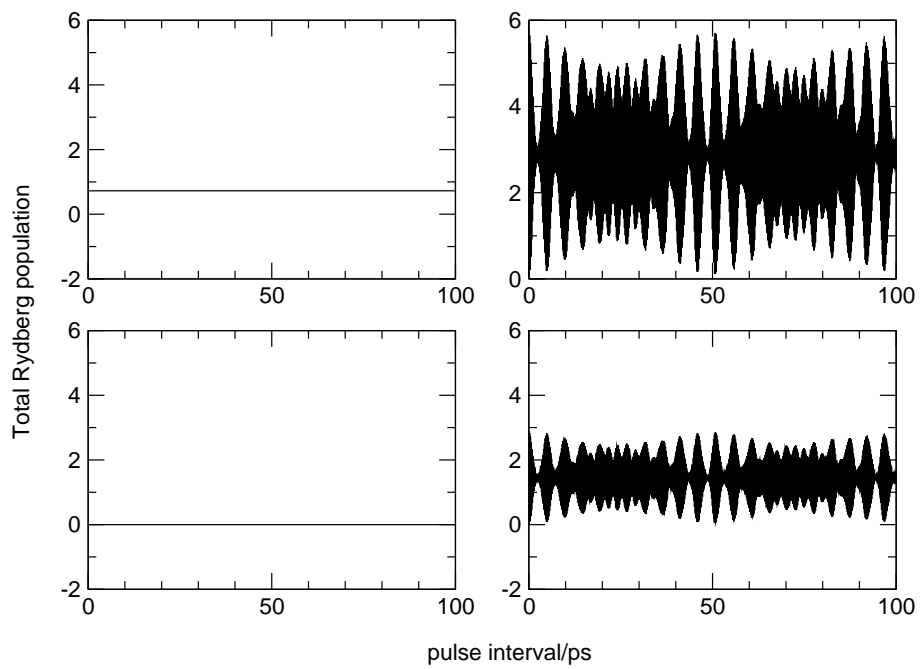
$$a_{nm_\ell}(t) \propto (-1)^{\ell'-m'_\ell} \left[\begin{pmatrix} \ell & 1 & \ell' \\ m_\ell & \mathbf{q}_1 & m'_\ell \end{pmatrix} + \begin{pmatrix} \ell & 1 & \ell' \\ m_\ell & \mathbf{q}_2 & m'_\ell \end{pmatrix} e^{-i\Delta_n\tau_d} e^{-i\omega_L\tau_d} \right]. \quad (7.8)$$

which implies that $P_{nm_\ell}(t) \propto (-1)^{\ell'-m_\ell} \mathfrak{Z}(\mathbf{q}_1)^2 + \mathfrak{Z}(\mathbf{q}_2)^2 + 2\mathfrak{Z}(\mathbf{q}_1)\mathfrak{Z}(\mathbf{q}_2) \cos(\Delta_n - \omega_L)\tau_d$, where \mathfrak{Z} is shorthand for the 3- j symbol in eqn. (7.8). These are plotted in Fig. 7.2 for a variety of combinations of polarization for a $s \rightarrow p$ ($m_\ell = 1$) transition. Where the polarization is identical in both arms, we recover the behaviour in [123]. Where there is a common component (circular then perpendicular or *vice versa*), the variation in the population has the same period but a smaller amplitude, and where we have differing polarizations, even where $\mathbf{q}_1 = \sqrt{1/2}(C_{11} \pm C_{1,-1})$ and $\mathbf{q}_2 = \sqrt{1/2}C_{11} \mp C_{1,-1}$, the Rydberg population remains constant, which shows that the pulse polarization will only be important where an external electric or magnetic field causes J -uncoupling [25, 26].

7.3 Fringes and plateaux

Fringes are regions of frequency-domain spectra dominated by a few widely-spaced intense lines. Often they indicate a resonance between two or more

Figure 7.2: Top left: parallel then perpendicular. Top right: parallel then parallel. Bottom left: circular then circular. Bottom right: perpendicular then perpendicular.



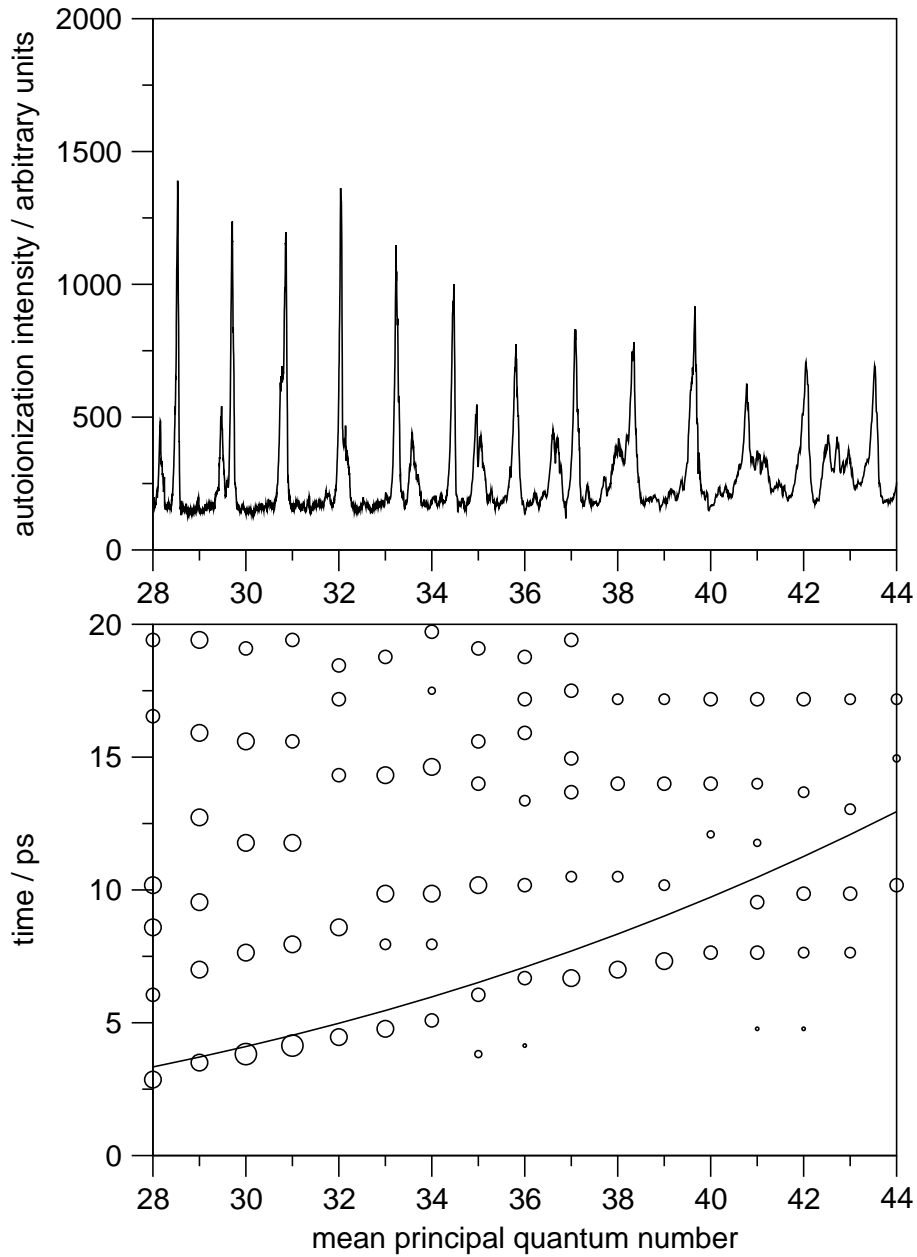
degrees of freedom, such as Fermi resonance between symmetric-stretching and bending modes in triatomic molecules. The wide spacing of strong lines transforms to short recurrence times in the autocorrelation spectrum.

Smith *et al.* [39] measure autocorrelation spectra for Rydberg states of nitric oxide excited *via* the $N' = 0, 1, 3$ and 5 levels of the $3s$ A state. On plotting the first recurrence times against principal quantum number, they find plateaux where the period of the electron matches the rotational period of the ionic core.

The corresponding low-field (10 V cm^{-1}) frequency-domain spectrum measured by Goodgame *et al.* [126] via the $N' = 0$ level shows strong np_0 and nf_2 and weaker np_2 and ns_1 series, and is shown in Fig. 7.3 along with a plot of times of peaks in the autocorrelation functions against principal quantum number. As we can see, the time of the first recurrence does not follow the Kepler time, but instead, for $\bar{n} > 36$, precedes it. This suggests that the plateaux observed are not artefacts of the measurement process, but have are manifestations of the same behaviour as the fringes in the frequency-domain spectrum.

In order to explain this phenomenon, we shall consider the stroboscopic effect, which is a resonance between electronic motion and the rotation of the ionic core in Rydberg states first encountered by Labastie *et al.* [127] in their optical–optical double resonance experiments on the sodium dimer.

Figure 7.3: Above: Nitric oxide (100) ionization spectra recorded by Goodgame *et al.* [126] (Fig. 4) *via* the $N' = 0$ intermediate in a 10 V cm^{-1} field plotted against the principal quantum number for the p0 channel. Below: (○) Plot of times of peaks of autocorrelation functions obtained by Fourier transformation of the frequency-domain spectrum plotted against mean principal quantum number. The size of the circle is proportional to the height of the peak. (Solid line) Kepler recurrence time.



The best way to explain the selection rules for the excitation process is to look at the short-range physics within the core region, as the intermediate state is typically small enough for Born–Oppenheimer dynamics still to hold, and extrapolate to the long-range dynamics by the frame transformation method. The short-range dipole transition moments are given by [20]:

$$\begin{aligned} \mathcal{D}_{N\ell\lambda, N'\ell'\lambda'}^\nu = \mathcal{R} \begin{pmatrix} \ell & 1 & \ell' \\ 0 & 0 & 0 \end{pmatrix} \left[\begin{pmatrix} N & 1 & N' \\ \lambda & \nu & -\lambda' \end{pmatrix} + (-1)^{p+N} \begin{pmatrix} N & 1 & N' \\ -\lambda & \nu & -\lambda' \end{pmatrix} \right] \\ \times \left[\begin{pmatrix} \ell & 1 & \ell' \\ \lambda & \nu & -\lambda' \end{pmatrix} + (-1)^{p+N} \begin{pmatrix} \ell & 1 & \ell' \\ -\lambda & \nu & -\lambda' \end{pmatrix} \right], \end{aligned} \quad (7.9)$$

where \mathcal{R} is the radial term, and summed over laser components ν . The parity terms show that $\Delta p = \Delta N$, so, for instance, from the A $3s\Sigma^+$ state of nitric oxide, $np\Sigma^+$ and $np\Pi^+$ series will be excited for odd ΔN , and $np\Pi^-$ for even ΔN .

Table 7.1 lists the case (b)–(d) couplings implied by eqn. (3.12). We can convert the case (b) transition moment matrix elements in eqn. (7.9) into a Hund’s case (d) basis by summing over laser components ν and final state electron angular momentum projections λ' , and taking the different radial terms \mathcal{R} to be equal (this is equivalent to assuming that they all have the same quantum defect, which is a condition for having reached the Hund’s

case (d) limit), a process we can express as:

$$\mathcal{D}_{N\ell\lambda, N'\ell'N^+} = \sum_{\alpha, \nu} \mathcal{U}_{i\alpha} \mathcal{D}_{N\ell\lambda, N'\ell'\lambda'}^{\nu}. \quad (7.10)$$

This is exact if we choose the long-range mixing coefficients to be $B_{i\rho}$ —if they are $Z_{i\rho}$ then it fails to take into account the difference of $\cos \pi \mu_{\alpha}$ in normalization between the long-range and short-range coefficients $A_{\alpha\rho}$ —again, the effect vanishes if all quantum defects are set equal. We obtain the case (d) transition moments

$$\begin{aligned} \mathcal{D}_{N\ell\lambda, N'\ell'N^+} = & \begin{pmatrix} \ell & 1 & \ell' \\ 0 & 0 & 0 \end{pmatrix} \begin{Bmatrix} N^+ & N' & \ell' \\ 1 & \ell & N \end{Bmatrix} \\ & \times \left[\begin{pmatrix} N^+ & \ell & N \\ 0 & \lambda & -\lambda \end{pmatrix} + (-1)^{p+J} \begin{pmatrix} N^+ & \ell & N \\ 0 & -\lambda & -\lambda \end{pmatrix} \right], \end{aligned} \quad (7.11)$$

the 6- j symbol in which implies the propensity rule

$$|N^+ - N| \leq \ell. \quad (7.12)$$

Take a two-channel system terminating on ionization thresholds E_1^+ and E_2^+ separated by $\Delta E \text{ cm}^{-1}$. We can write the principal quantum number ν_1

Table 7.1: Couplings between short-range and long-range channels in Rydberg states of diatomic molecules implied by equation (3.12). The case (d) channels are labelled with ℓ and N^+ .

Case (b) channels		Case (d) channels
$s\Sigma^+$	\longleftrightarrow	sN
$p\Sigma^+, p\Pi^+$	\longleftrightarrow	$p(N \pm 1)$
$d\Sigma^+, d\Pi^+, d\Delta^+$	\longleftrightarrow	$dN, d(N \pm 2)$
$f\Sigma^+, f\Pi^+, f\Delta^+, f\Phi^+$	\longleftrightarrow	$f(N \pm 1), f(N \pm 3)$
$p\Pi^-$	\longleftrightarrow	pN
$d\Pi^-, d\Delta^-$	\longleftrightarrow	$d(N \pm 1)$
$f\Pi^-, f\Delta^-, f\Phi^-$	\longleftrightarrow	$fN, f(N \pm 2)$

for one channel in terms of the other (ν_2) as

$$\nu_1 = \frac{\nu_2}{\sqrt{1 - \nu_2^2 \Delta E / \text{Ry}}}. \quad (7.13)$$

For stroboscopic fringes to occur, the rotational and electronic spacings of the system should coincide, and this coincidence should persist over several values of ν . For the conditions (a) $\nu_1 - \nu_2 = k$, where k is an integer, and (b) $d\nu_1/d\nu_2 \simeq 1$ to hold simultaneously, one requires

$$2k \ll \nu_2 \ll (\Delta E / \text{Ry})^{-1/2}. \quad (7.14)$$

The last fringe will happen at

$$k_{\max} = \sqrt{250 / \Delta E}, \quad (7.15)$$

Table 7.2: Stroboscopic fringes predicted for the p channels in the nitric oxide $N' = 0, v = 1$ Rydberg series.

k	\bar{n}	\bar{E}/cm^{-1}
1	26.5	76909.2
2	33.4	76967.1
3	38.2	76990.3
4	42.0	77003.3

which leads to the general stroboscopic condition

$$\nu^3 \sim \frac{2k\text{Ry}}{4B(J + \frac{1}{2})}, \quad (7.16)$$

which is valid for $J > 1$. Fig. 7.4 shows the results for nitric oxide and the sodium dimer. For $J = 1 \leftarrow J' = 0$ transitions, only Σ and Π case (b) channels are allowed, which correlate to $N^+ = \ell \pm 1$ channels in case (d). The rotational level spacing therefore being $B(4\ell + 2)$, the $J = 1$ stroboscopic condition is

$$n^3 \sim \frac{2k\text{Ry}}{B(4\ell + 2)}. \quad (7.17)$$

This manifestation of the stroboscopic effect is discussed in Chang *et al.* [71], where it is observed in the np and nf series of the sodium dimer, and Fredin *et al.* [128], where s-d mixing of channels in the $v = 0$ level of nitric oxide results in a complicated resonance instead of a single sharp line.

If we assume that the A $^2\Sigma^+$ intermediate state has pure 3s character, then, ignoring multipole mixing and Rydberg–valence interactions, only np

Figure 7.4: Principal quantum numbers ν at which stroboscopic fringes are expected, plotted against initial rotational angular momentum for NO (Δ) and Na₂ (\circ).

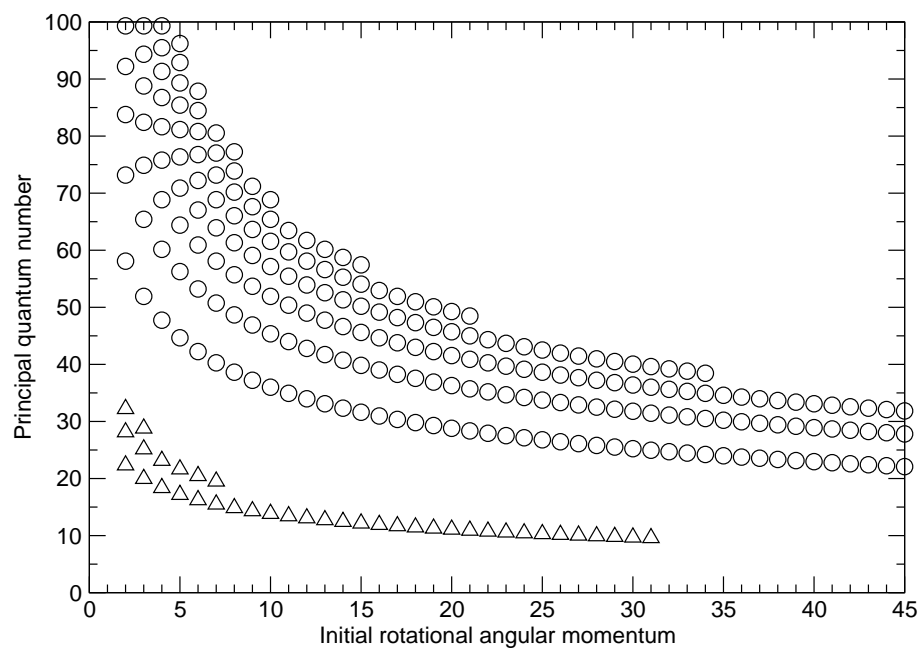
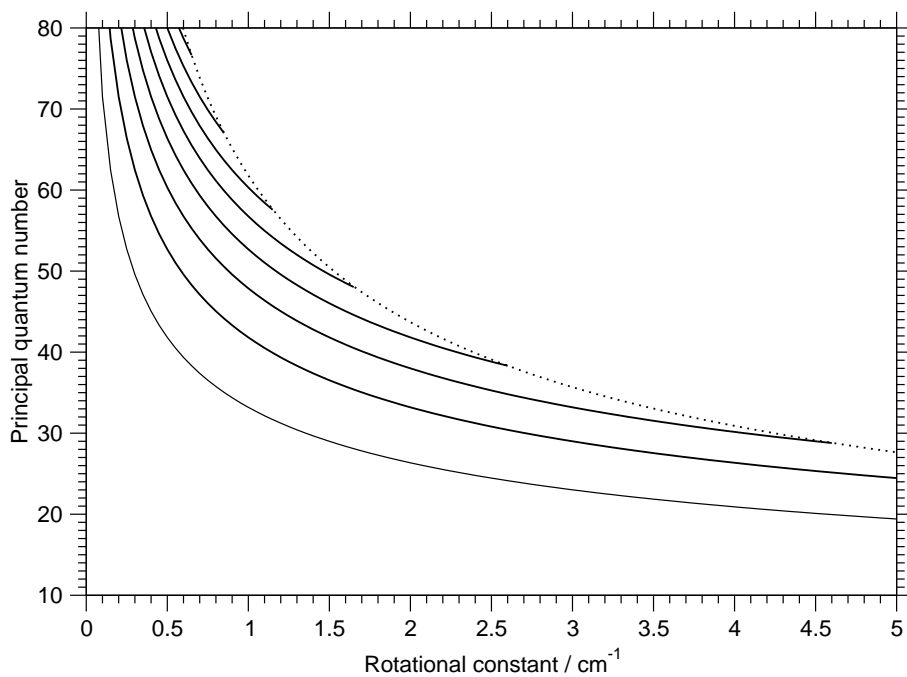


Figure 7.5: Principal quantum numbers ν at which stroboscopic fringes are expected, plotted against rotational constant for $J' = 1$. The dotted line shows k_{\max} as defined in eqn. (7.15).



states will be excited. If our initial state has $N' = 0$, then our short-range channels will be $p\Sigma$ and $p\Pi$ and their long-range counterparts will be $p0$ and $p2$. Eqn. (7.17) predicts stroboscopic returns at the principal quantum numbers listed in Table 7.2. $k_{\max} = 4.6$ for this system, according to eqn. (7.15). The parameters we shall adjust are the quantum defect functions $\mu_{\Sigma}(R)$ and $\mu_{\Pi}(R)$, which we take as a Taylor expansion around the equilibrium ion bond length:

$$\mu(R) = \mu(R_e^+) + \frac{d\mu}{dR}(R - R_e^+). \quad (7.18)$$

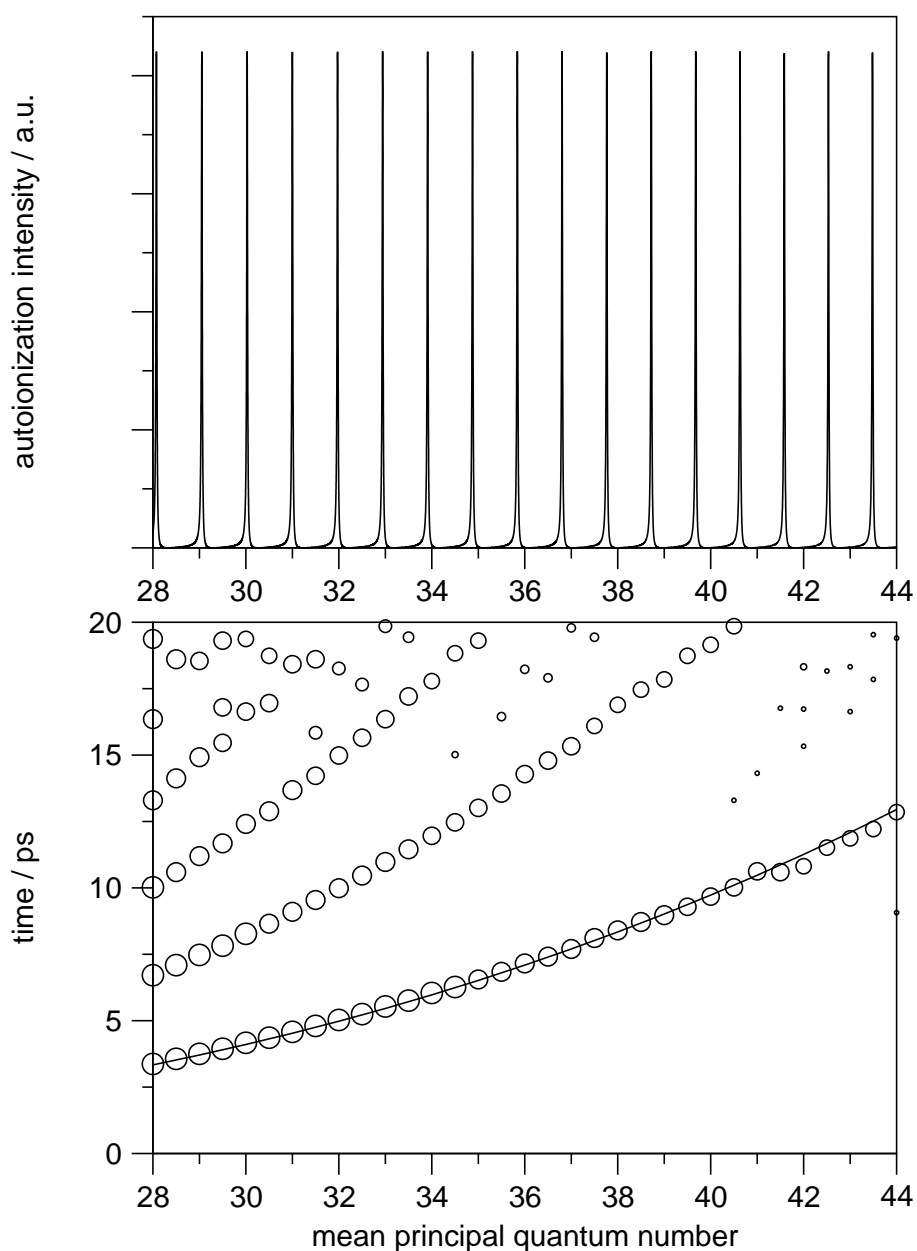
We parameterize the dynamics by the difference between the equilibrium values of the short-range quantum defects:

$$\mu_{\Pi}(R_e^+) = \mu_{\Sigma}(R_e^+) + \Delta\mu. \quad (7.19)$$

There are two extreme cases.

(i) Where $\Delta\mu = 0$, the Hund's case (d) propensity rule (7.12) holds exactly, and a single $np0$ series is excited. In the time domain this shows simple hydrogenic behaviour with classical recurrences at the Kepler times and full revivals near T_{rev} , the exact positions of which depends on $\mu_{\Sigma}(R_e^+)$ [129]. This is shown in Fig. 7.6. Mulliken [7] identifies the special case where the two channels have a common threshold as *accidental pure precession*.

Figure 7.6: Above: Hydrogenic spectrum for a four-channel system where $\Delta\mu = 0$ plotted against principal quantum number. Below: (○) Plot of times of peaks of autocorrelation functions plotted against mean principal quantum number. The size of the circle is proportional to the height of the peak. (Solid line) Kepler recurrence time.



(ii) Where $\Delta\mu = 0.5$, Hund's case (b) behaviour persists throughout the spectrum which consists of two interpenetrating np series with marked modulations in intensity. The intensities are about equal at the stroboscopic points in Table 7.2, and the $np0$ and $np2$ contributions to the lines are about equal. Between the stroboscopic points the spectrum simplifies with most of the intensity appearing in one series, although the composition of the lines is still essentially case (b), with 66% in one pN^+ channel and 33% in the other. Mulliken [7] calls this *inhibited ℓ -uncoupling*, and, using a perturbation theory approach, predicts it for a two-channel case where $\Delta\mu = 0.5$, his argument being that the λ -doubling perturbations on the $n\Sigma$ state from the $n\Pi$ and $(n+1)\Pi$ states will cancel one another out, and that in any case any matrix element between Σ and Π states will vanish as the outermost loops of their radial wavefunctions will be exactly in antiphase. The frequency-domain spectrum and recurrence times are shown in Fig. 7.7.

If we assume a small mixture of d character in the initial state, then we need np and nf channels to describe the spectrum, and for the $N' = 0$ case, we have short-range $p\Sigma$, $p\Pi$, $f\Sigma$, $f\Pi$ and long-range $p0$, $p2$, $f2$ and $f4$ channels. If $\Delta\mu_p = \Delta\mu_f = 0$, there will be two interpenetrating series without the intensity modulation seen above.

In the $np0/np2$ series system in Fig. 7.7, we see plateaux in the first recurrence around $\bar{n} = 31$, $\bar{n} = 36-38$, $\bar{n} = 42$, and $\bar{n} = 46$. There is a strong

Figure 7.7: Above: Frequency-domain ionization spectrum for a four-channel system where $\Delta\mu = 0.5$ plotted against principal quantum number. Below: (○) Plot of times of peaks of autocorrelation functions plotted against mean principal quantum number. The size of the circle is proportional to the height of the peak. (Solid line) Kepler recurrence time.

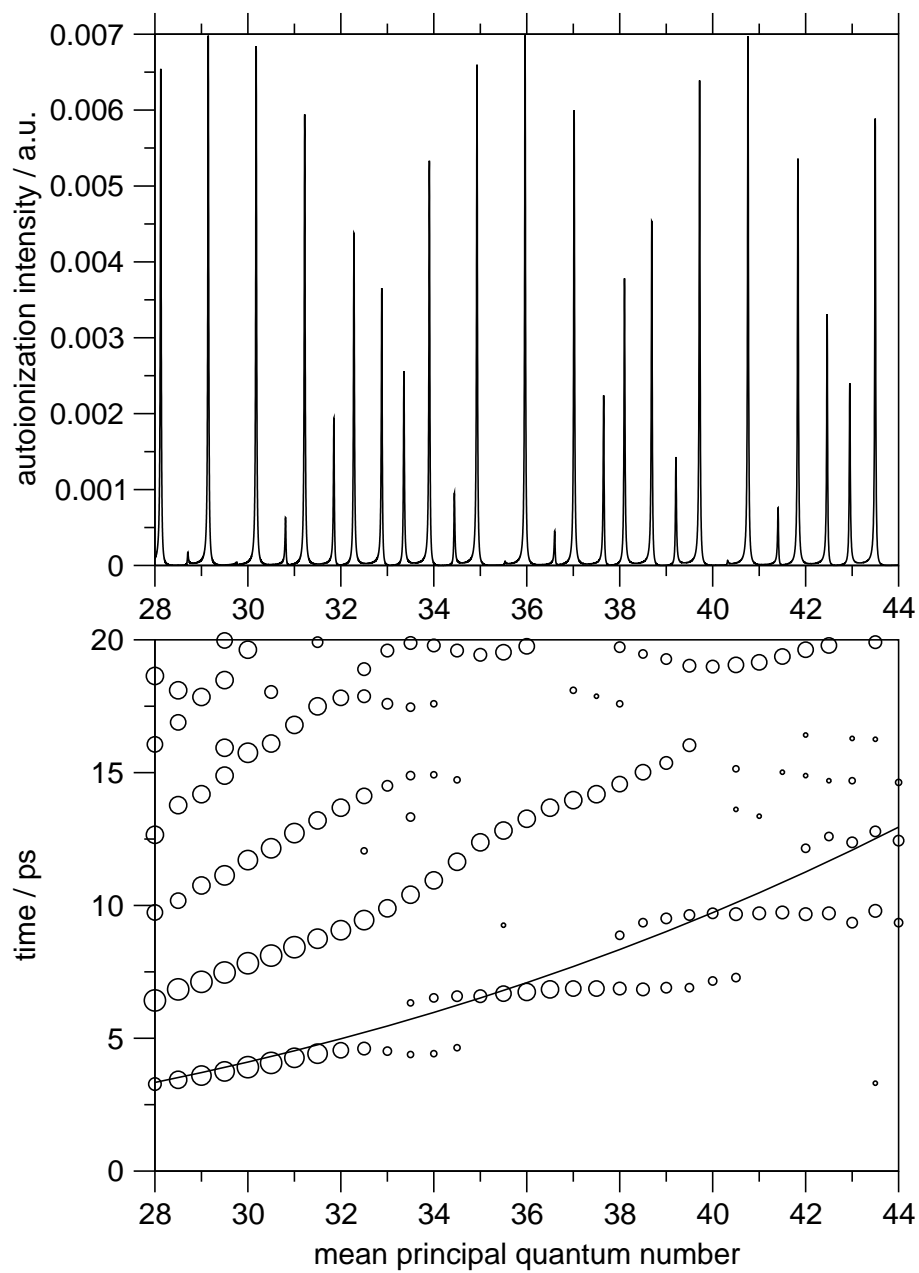
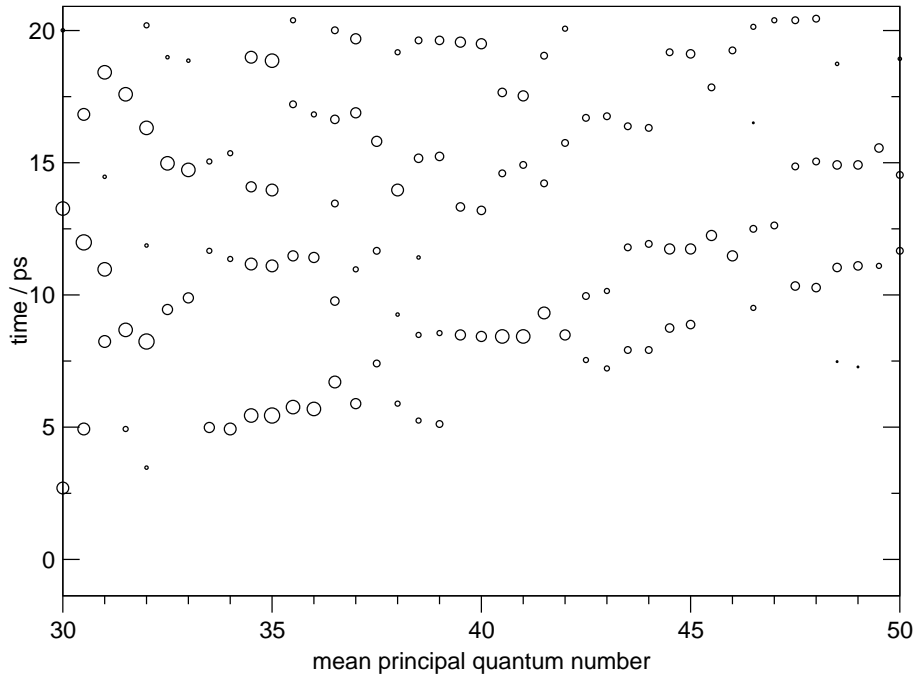


Figure 7.8: (○) Plot of times of peaks of autocorrelation functions plotted against mean principal quantum number. The size of the circle is proportional to the height of the peak. (Solid line) Kepler recurrence time.



and largely unperturbed second recurrence at $2\tau_0$.

By contrast, in the $np0/nf2$ system in Fig. 7.8, the first recurrence time plateaus around $\bar{n} = 32$, $\bar{n} = 34-36$, $\bar{n} = 40$ and $\bar{n} = 44-46$. There is only fragmentary evidence of a revival around $2\tau_0$.

7.4 The phase problem

The experiment measures the modulus of the autocorrelation function but not its phase. This, reminiscent of the phase problem in crystallography,

means that only the spacings and lineshapes of the frequency-domain spectrum can be recovered by Fourier transforming the time-domain spectrum. Crystallography, of course, has the great advantage of the atomic structure of matter. If the phase problem could be overcome, we could obtain frequency-domain resolution a great deal smaller than the width of the laser, and only limited by the coherence time of the sample.

Weinacht *et al.* [130] have demonstrated that it is possible to extract the phase information through a cross-correlation experiment. In a Michelson interferometer, where a beam is split in two, and one beam delayed by an interval τ , the total intensity detected is the autocorrelation function of the field $E(t)$ at different times:

$$\text{Auto}(t) = 2 \int E(t)E(t + \tau) dt + 2 \int |E(t)|^2 dt. \quad (7.20)$$

Compare this with the Rydberg population in equation (7.7). Now consider a known reference field as the second pulse in a cross-correlation experiment:

$$\text{Cross}(t) = 2 \int E(t)E_{\text{ref}}(t + \tau) dt + 2 \int |E(t)|^2 + |E_{\text{ref}}(t)|^2 dt. \quad (7.21)$$

This first term can be Fourier transformed to obtain the phase difference between each frequency component of E and E_{ref} .

One commonly-used technique in crystallography is to take the magnitudes from experiment and apply the phases from a similar known system. Cowtan [131] provides a charming illustration of this with images of a cat and a duck. In the F_o method, the amplitudes are taken from the experiment. A more sophisticated version is denoted $2|F_o| - |F_c|$, where the experimental magnitudes are doubled and the magnitudes of the known system subtracted.

We shall conclude with a brief look at the phase evolution of the hydrogenic autocorrelation functions described above. A more visual quantity than the phase itself is its time derivative. Figs. 7.9–7.11 show $|\text{Auto}(t)|$ and $d[\arg \text{Auto}(t)]/dt$ evaluated at 119.5 cm^{-1} , 59.5 cm^{-1} and 49.5 cm^{-1} below threshold respectively.

(i) In Fig. 7.9 the packet consists of two states, and we see Keplerian behaviour and dispersion-free decay. The rate of change of the phase oscillates between 1 and 0 at the Kepler frequency.

(ii) In Fig. 7.10, a second-order revival is visible near $T_{\text{rev}}/2$. One might naively assume, that since the initial wavepacket has split into two, each out of phase with the other by $\pi/2$, that the rate of change of phase would be double that of the classical case. Instead it diverges.

(iii) In Fig. 7.11, there is enough dispersion for a third-order revival around $T_{\text{rev}}/3$, and the rate of change of the phase is not significantly more interesting.

Figure 7.9: Autocorrelation function and the time derivative of phase of autocorrelation function evaluated at 119.5 cm^{-1} below threshold for the hydrogenic system shown in Fig. 7.6.

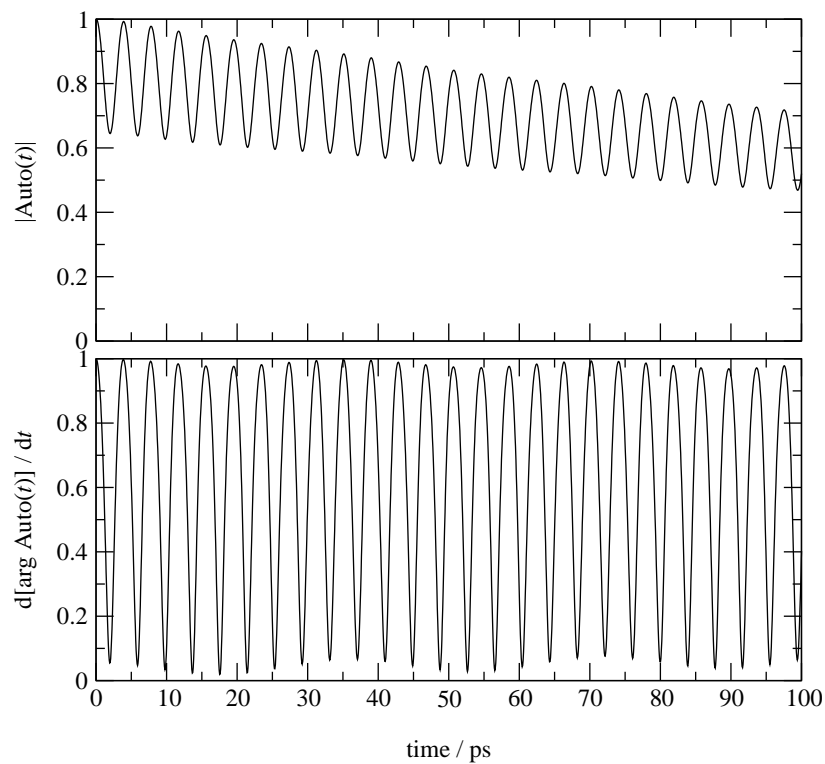


Figure 7.10: Autocorrelation function and the time derivative of phase of autocorrelation function evaluated at 59.5 cm^{-1} below threshold for the hydrogenic system shown in Fig. 7.6.

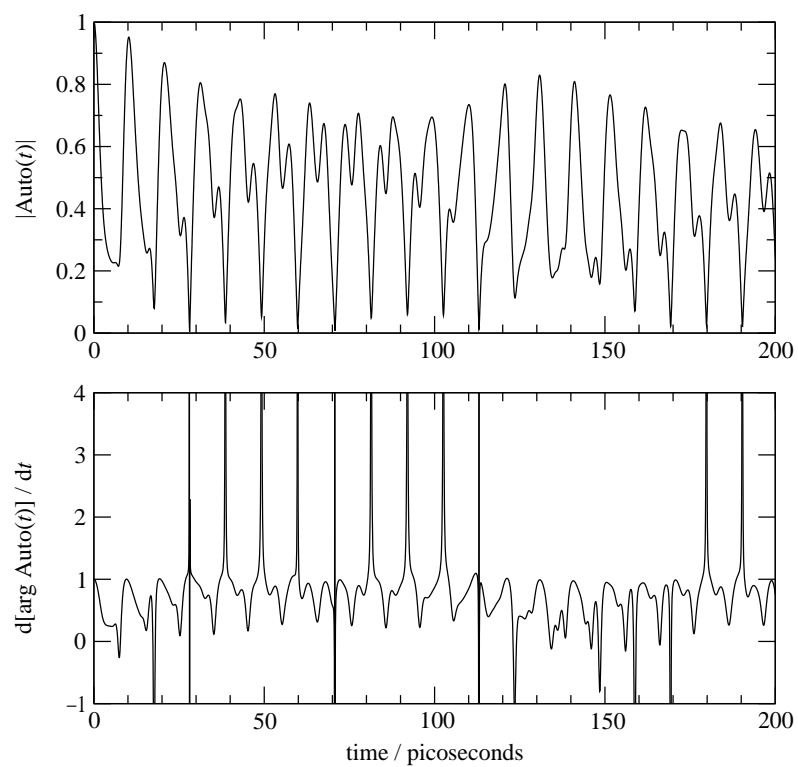
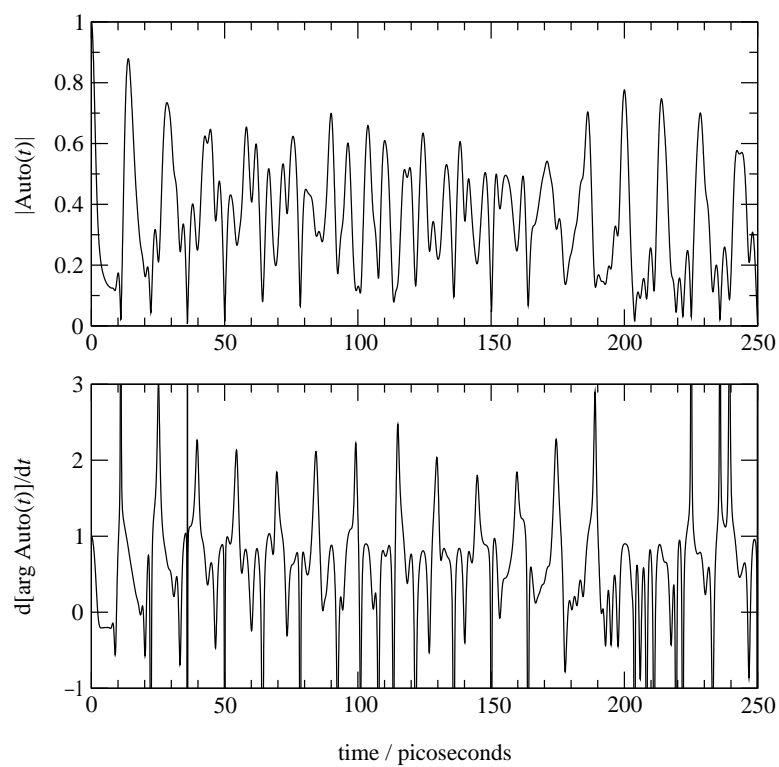


Figure 7.11: Autocorrelation function and the time derivative of phase of autocorrelation function evaluated at 49.5 cm^{-1} below threshold for the hydrogenic system shown in Fig. 7.6.



There seems to be no obvious functional form we can fit to the phase for this simple hydrogenic case; the way to proceed may well be to test the efficiency of $2|F_o| - |F_c|$ maps on model spectra.

7.5 Conclusion

This chapter has given a selective overview of electronic wave-packet experiments. We have applied multichannel quantum defect theory to the Rydberg wave-packet experiments of Fielding and co-workers, with particular reference to the ‘plateau regions’ of the autocorrelation function, where resonance between the electronic and rotational energy spacings of the system is associated with non-hydrogenic behaviour.

o O o

Since the writing of this thesis, it has been shown that this sort of non-hydrogenic behaviour in a two-channel system is quantifiable and arises from the phase difference between the wave packets in the two channels. It turns out to depend not only on the difference in quantum defect between the two channels, but also the difference in ionic core rotational energies. See Smith *et al.* [132].

Chapter 8

Summary

The thesis has dealt with the application of multichannel quantum defect theory (MQDT) to topic in the dynamics of Rydberg molecules, concentrating on two areas:

(i) **The long-range properties of the H_2O^+ ion and their effects on the autoionization, threshold ionization and photoelectron spectra of the Rydberg states of water.** To this end, we have developed a theory relating the quantum defects and reactance matrix elements for $\ell \geq 3$ Rydberg states of an asymmetric top molecule to the multipole moments and polarizabilities of its ionic core. This has been combined with MQDT, which can be used to calculate the energies of Rydberg states, their absorption line strengths, autoionization cross sections and even angular distributions. We have fitted three long-range parameters (which are difficult to obtain by

conventional experimental means) to the REMPI spectra of the nf Rydberg states of water by Child and Glab, and found that the fit is almost as good as that obtained fitting the seven nf quantum defects to the same data. We have also calculated these parameters *ab initio* in order to construct a reactance matrix which could predict the dynamics of the ionization process and hence the vibrational and rotational distributions in photoelectron spectra, such as those measured by Glab. The empirical parameters have been used to calculate rotational distributions and found inadequate, without even qualitative agreement with experiment. More qualitative agreement, using the same simple model, has been found in the treatment of Dickinson *et al.*'s MATI spectra of water.

(ii) Rydberg wave packet dynamics in the nitric oxide molecule.

Here a model incorporating MQDT has been constructed for simulation of the autocorrelation experiments of Fielding and co-workers, in order to try to explain the 'plateau' phenomenon, where the wave packets deviate from simple hydrogenic behaviour. The stroboscopic effect, where at certain energies long-range Rydberg systems exhibit short-range behaviour, and its effects on the plateau phenomenon, have been investigated.

Chapter 9

Appendices

9.1 Spherical harmonics and multipoles

The general spherical harmonic is defined by

$$C_{kq} = (-1)^q \sqrt{\frac{(k-q)!}{(k+q)!}} P_k^q(\cos \theta) e^{iq\phi}, \quad (9.1)$$

$$C_{k,-q} = (-1)^q C_{kq}(\theta\phi)^*, \quad (9.2)$$

where P_k^q is the associated Legendre polynomial defined in terms of the Legendre polynomial by

$$P_k^q(\cos \theta) = (-1)^q \sin^q \theta \frac{d^q P_k(\cos \theta)}{d(\cos \theta)^q}. \quad (9.3)$$

The Legendre polynomial, should you need it, can be obtained from the generating function

$$g(x, t) = (1 - 2tx + t^2)^{-1/2} = \sum_{n=0}^{\infty} t^n P_n(x). \quad (9.4)$$

A general Cartesian second rank tensor T_{ij} decomposes into

$$T_{ij} = \frac{1}{3}\delta_{ij}T^t + T_k^a + T_{ij}^s, \quad (9.5)$$

where

(i) $T^t = T_{ii}$ transforms as $Y_{00}(\theta\phi)$.

(ii) $T_k^a = \frac{1}{2}(T_{ij} - T_{ji})$ is antisymmetric, first rank, has zero trace, and transforms as $Y_{1m}(\theta\phi)$.

(iii) $T_{ij}^s = \frac{1}{2}(T_{ij} + T_{ji}) - \frac{1}{3}\delta_{ij}T^t$ is symmetric, second rank, and transforms as $Y_{2m}(\theta\phi)$.

9.2 Useful expressions

First, we quote some useful angular-momentum results from Brink and Satchler [61]. The integral of C_{kq} with two other spherical harmonics $Y_{\ell\lambda}$ and $Y_{\ell'\lambda'}$ over all angles (θ, ϕ) is a well-known result in angular momentum theory.

Table 9.1: Converting between cartesian and spherical tensor multipole moments from Price *et al.* [133]

$M_{00}=q$	
$M_{10}=\mu_z$	
$M_{11c}=\mu_x$	$M_{11s}=\mu_y$
$M_{20}=Q_{zz}$	
$M_{21c}=\sqrt{4/3}Q_{xz}$	$M_{21s}=\sqrt{4/3}Q_{yz}$
$M_{22c}=\sqrt{1/3}(Q_{xx} - Q_{yy})$	$M_{22s}=\sqrt{4/3}Q_{xy}$
$M_{30}=\Omega_{zzz}$	
$M_{31c}=\sqrt{3/2}\Omega_{xzz}$	$M_{31s}=\sqrt{3/2}\Omega_{yzz}$
$M_{32c}=\sqrt{3/5}(\Omega_{xxz} - \Omega_{yyz})$	$M_{32s}=2\sqrt{3/5}\Omega_{xyz}$
$M_{33c}=\sqrt{1/10}(\Omega_{xxx} - 3\Omega_{xyy})$	$M_{33s}=\sqrt{1/10}(3\Omega_{xxy} - \Omega_{yyy})$
$M_{40}=\Phi_{zzzz}$	
$M_{41c}=\sqrt{8/5}\Phi_{xzzz}$	$M_{41s}=\sqrt{8/5}\Phi_{yzzz}$
$M_{42c}=\sqrt{4/5}(\Phi_{xxzz} - \Phi_{yyzz})$	$M_{42s}=\sqrt{16/5}\Phi_{xyzz}$
$M_{43c}=\sqrt{8/35}(\Phi_{xxxz} - 3\Phi_{xyyz})$	$M_{43s}=\sqrt{8/35}(\Phi_{xxyz} - \Phi_{yyyz})$
$M_{44c}=\sqrt{1/35}(\Phi_{xxxx} - 6\Phi_{xxyy} + \Phi_{yyyy})$	$M_{44s}=\sqrt{16/35}(\Phi_{xxxy} - \Phi_{xyyy})$

$$\langle \ell' \lambda' | C_{kq} | \ell \lambda \rangle = (-1)^{\lambda'} \sqrt{(2\ell' + 1)(2\ell + 1)} \begin{pmatrix} \ell' & k & \ell \\ 0 & 0 & 0 \end{pmatrix} \begin{pmatrix} \ell' & k & \ell \\ -\lambda' & q & \lambda \end{pmatrix} \quad (9.6)$$

which for the symmetrized spherical harmonic functions defined above becomes

$$\begin{aligned} \langle \ell' \lambda' | C_{kq} | \ell \lambda \rangle &= \frac{(-1)^{\lambda'} \sqrt{(2\ell' + 1)(2\ell + 1)} (1 + (-1)^{p_e + p'_e})}{2((1 + \delta_{\lambda'0})(1 + \delta_{\lambda 0}))^{1/2}} \begin{pmatrix} \ell' & k & \ell \\ 0 & 0 & 0 \end{pmatrix} \\ &\times \left[\begin{pmatrix} \ell' & k & \ell \\ -\lambda' & q & \lambda \end{pmatrix} + (-1)^{p_e} \begin{pmatrix} \ell' & k & \ell \\ -\lambda' & q & -\lambda \end{pmatrix} \right]. \end{aligned} \quad (9.7)$$

The integral over all space of three Wigner \mathcal{D} functions is

$$\begin{aligned}
& \int \mathcal{D}_{M'_1 M_1}^{(J_1)}(\alpha\beta\gamma) \mathcal{D}_{M'_2 M_2}^{(J_2)}(\alpha\beta\gamma) \mathcal{D}_{M'_3 M_3}^{(J_3)}(\alpha\beta\gamma) \, d\Omega \\
& = 8\pi^2 \begin{pmatrix} J_1 & J_2 & J_3 \\ M'_1 & M'_2 & M'_3 \end{pmatrix} \begin{pmatrix} J_1 & J_2 & J_3 \\ M_1 & M_2 & M_3 \end{pmatrix}, \tag{9.8}
\end{aligned}$$

where $d\Omega = \sin\beta \, d\alpha \, d\beta \, d\gamma$. The contraction formula for rotation matrices is

$$[\mathcal{D}_{cc'}^C(\alpha\beta\gamma)]^* \begin{pmatrix} A & B & C \\ a' & b' & c' \end{pmatrix} = \sum_{ab} \begin{pmatrix} A & B & C \\ a & b & c \end{pmatrix} \mathcal{D}_{aa'}^A(\alpha\beta\gamma) \mathcal{D}_{bb'}^B(\alpha\beta\gamma), \tag{9.9}$$

and the 3- j contraction formula is

$$\begin{aligned}
& \sum_{\alpha\beta\gamma} (-1)^{A+B+C+\alpha+\beta+\gamma} \begin{pmatrix} A & B & c \\ \alpha & -\beta & \gamma' \end{pmatrix} \begin{pmatrix} B & C & a \\ \beta & -\gamma & -\alpha' \end{pmatrix} \begin{pmatrix} C & A & b \\ \gamma & -\alpha & \beta' \end{pmatrix} \\
& = \begin{pmatrix} a & b & c \\ \alpha' & \beta' & \gamma' \end{pmatrix} \left\{ \begin{matrix} a & b & c \\ A & B & C \end{matrix} \right\}, \tag{9.10}
\end{aligned}$$

In order to calculate the matrix elements of C_{kq} for Hund's case (d) basis states $|N^+K^+\rangle$, we write them as a sum over the case (b) matrix elements in eqn. (9.6)

$$\begin{aligned}
\langle N^{+'}K^{+'} | C_{kq} | N^{+}K^{+} \rangle &= \sqrt{(2N^{+'} + 1)(2N^{+} + 1)} \\
\times \sum_{\lambda, \lambda', K, K'} &\begin{pmatrix} \ell' & N^{+'} & J \\ \lambda' & K^{+'} & -K' \end{pmatrix} \begin{pmatrix} \ell & N^{+} & J \\ \lambda & K^{+} & -K \end{pmatrix} \langle \ell \lambda' | \langle JMK' | C_{kq} | JMK \rangle | \ell \lambda \rangle \\
&= \sqrt{(2N^{+'} + 1)(2N^{+} + 1)(2\ell' + 1)(2\ell + 1)} \begin{pmatrix} \ell' & k & \ell \\ 0 & 0 & 0 \end{pmatrix} \\
&\quad \times \sum_{\lambda, \lambda', K, K'} (-1)^{K+K'+\lambda'} \delta_{KK'} \begin{pmatrix} \ell' & k & \ell \\ -\lambda' & q & \lambda \end{pmatrix} \\
&\quad \times \begin{pmatrix} \ell' & N^{+'} & J \\ \lambda' & K^{+'} & -K' \end{pmatrix} \begin{pmatrix} \ell & N^{+} & J \\ \lambda & K^{+} & -K \end{pmatrix}. \quad (9.11)
\end{aligned}$$

Eqn. (9.10) reduces the expression to

$$\begin{aligned}
\langle N^{+'}K^{+'} | C_{kq} | N^{+}K^{+} \rangle &= (-1)^{J+K^{+}+k} \sqrt{(2\ell' + 1)(2\ell + 1)} \begin{pmatrix} \ell' & k & \ell \\ 0 & 0 & 0 \end{pmatrix} \\
&\times \sqrt{(2N^{+'} + 1)(2N^{+} + 1)} \begin{pmatrix} N^{+} & N^{+'} & k \\ K^{+} & K^{+'} & q \end{pmatrix} \left\{ \begin{matrix} N^{+} & N^{+'} & k \\ \ell' & \ell & J \end{matrix} \right\}, \quad (9.12)
\end{aligned}$$

which when symmetrized properly for the asymmetric top becomes

$$\begin{aligned}
\langle N^{+'}K^{+'}, p' | C_{kq} | N^{+}K^{+}, p \rangle &= (-1)^{J+K^{+'}+k} \left(1 + (-1)^{k+p+p'+\ell+\ell'} \right) \\
&\times \sqrt{\frac{(2N^{+'} + 1)(2N^{+} + 1)(2\ell' + 1)(2\ell + 1)}{4(1 + \delta_{K^{+'}0})(1 + \delta_{K^{+}0})}} \left\{ \begin{matrix} \ell & \ell' & k \\ N^{+'} & N^{+} & J \end{matrix} \right\} \\
&\times \begin{pmatrix} \ell' & k & \ell \\ 0 & 0 & 0 \end{pmatrix} \left[\begin{pmatrix} N^{+} & k & N^{+'} \\ K^{+} & q & K^{+'} \end{pmatrix} + (-1)^{N^{+'}+p'+\ell'} \begin{pmatrix} N^{+} & k & N^{+'} \\ K^{+} & q & -K^{+'} \end{pmatrix} \right]. \quad (9.13)
\end{aligned}$$

9.3 Change of origin

If the dipole moment measured from an arbitrary origin is

$$\mu_z^O = \langle 0 | \sum_a e_a a_z | 0 \rangle, \quad (9.14)$$

then moving to $(0, 0, z)$ will result in a new dipole moment

$$\mu_z^Z = \langle 0 | \sum_a e_a (a_z - z) | 0 \rangle = qz. \quad (9.15)$$

For the quadrupole moment

$$\begin{aligned} \Theta_{zz}^Z &= \sum_a e_a \left[\frac{3}{2} (a_z - z)^2 - \frac{1}{2} (a_x^2 + a_y^2 + (a_z - z)^2) \right] \\ &= \sum_a e_a \left[\left(\frac{3}{2} a_z^2 - \frac{1}{2} a^2 \right) - 2a_z z + z^2 \right] \\ &= \Theta_{zz}^O - 2\mu_z^O z + qz^2, \end{aligned} \quad (9.16)$$

which shows that the quantity $Q_{zz} - \mu_z^2$ is invariant to changes of origin. The Na^+ ion has no multipole moment higher than the charge measured from the nucleus, but at $z a_0$ away, the first few multipole moments become

$$q = +1, \quad \mu_z = -qz, \quad \Theta_{zz} = +qz^2, \quad \Omega_{zzz} = -qz^3. \quad (9.17)$$

For the general case, Stone [72] quotes a result in Brink and Satchler [61] on the addition of spherical harmonics:

$$R_{LM}(\mathbf{a} + \mathbf{b}) = \sum_{\ell_1 \ell_2} \sum_{m_1 m_2} \delta_{\ell_1 + \ell_2, L} (-1)^{L+M} \sqrt{\frac{(2L+1)!}{(2\ell_1)!(2\ell_2)!}} \quad (9.18)$$

$$\times R_{\ell_1 m_1}(\mathbf{a}) R_{\ell_2 m_2}(\mathbf{b}) \begin{pmatrix} \ell_1 & \ell_2 & L \\ m_1 & m_2 & -M \end{pmatrix},$$

therefore

$$R_{\ell k}(\mathbf{r} - \mathbf{c}) = \sum_{\ell'=0}^{\ell} \sum_{k'=-\ell'}^{\ell'} \sqrt{\binom{\ell+k}{\ell'+k'} \binom{\ell-k}{\ell'-k'}} R_{\ell' k'}(\mathbf{r}) R_{\ell-\ell', k-k'}(-\mathbf{c}), \quad (9.19)$$

which means that

$$Q_{\ell k}^C = \sum_{\ell'=0}^{\ell} \sum_{k'=-\ell'}^{\ell'} \sqrt{\binom{\ell+k}{\ell'+k'} \binom{\ell-k}{\ell'-k'}} Q_{\ell' k'}^O R_{\ell-\ell', k-k'}(-\mathbf{c}). \quad (9.20)$$

Therefore $Q_{\ell k}$ will be invariant under arbitrary changes of origin if and only if $Q_{\ell' k'} = 0$ for all $\ell' < \ell$.

9.4 Expectation values of r^n

For $\langle r^{-k} \rangle$ where $k > 2$, the expectation values scale with n as quantum defects plus terms in powers of ϵ .

$$\langle r^2 \rangle_{n\ell} = \frac{1}{2}n^2[n^2 - 3\ell(\ell + 1) + 1] \quad (9.21)$$

$$\langle r \rangle_{n\ell} = \frac{1}{2}[3n^2 - \ell(\ell + 1)] \quad (9.22)$$

$$\langle r^{-1} \rangle_{n\ell} = n^{-2}, \quad (9.23)$$

$$\langle r^{-2} \rangle_{n\ell} = [n^3(\ell + \frac{1}{2})]^{-1}, \quad (9.24)$$

$$\langle r^{-3} \rangle_{n\ell} = [n^3\ell(\ell + \frac{1}{2})(\ell + 1)]^{-1}, \quad (9.25)$$

$$\langle r^{-4} \rangle_{n\ell} = \frac{3 - \ell(\ell + 1)n^{-2}}{2n^3(\ell - 1)\ell(\ell + \frac{1}{2})(\ell + 1)(\ell + \frac{3}{2})}, \quad (9.26)$$

$$\langle r^{-5} \rangle_{n\ell} = \frac{5n^2 - 3\ell(\ell + 1) + 1}{2n^5(\ell - 1)(\ell - \frac{1}{2})\ell(\ell + \frac{1}{2})(\ell + 1)(\ell + \frac{3}{2})(\ell + 2)(\ell + \frac{5}{2})} \quad (9.27)$$

These equations are taken from the work of Bockasten [59], who points out that the negative and positive powers of r are connected through

$$\langle r^{-(k+2)} \rangle_{n\ell} = \left(\frac{2}{n}\right)^{2k+1} \frac{(2\ell - k)!}{(2\ell + k + 1)!} \langle r^{k-1} \rangle, \quad (9.28)$$

where $\ell \geq \frac{1}{2}k$. Drachman [134] notes that the energy dependence in $\langle r^{-6} \rangle$ can be eliminated through the equality

$$\frac{-1}{n^2} \langle r^{-6} \rangle = \frac{-11}{5} \langle r^{-7} \rangle + \frac{3}{10} [(2\ell + 1)^2 - 36] \langle r^{-8} \rangle. \quad (9.29)$$

9.5 Root finding

The code by Gilbert in Vrakking *et al.* [62] seeks energies E at which $|\mathbf{K} - \tan \boldsymbol{\beta}(E)| = 0$, that is to say, it looks for the vector \mathbf{x} where

$$\mathbf{A}\mathbf{x} = 0. \quad (9.30)$$

We can partition the $n \times n$ matrix \mathbf{A} such that

$$(\mathbf{A}^{(n-1) \times n} | \mathbf{y}) \begin{pmatrix} x_1/x_n \\ \dots \\ 1 \end{pmatrix} = 0, \quad (9.31)$$

which can be rewritten as

$$(\mathbf{A}^{(n-1) \times (n-1)}) \begin{pmatrix} x_1/x_n \\ \dots \\ x_{n-1}/x_n \end{pmatrix} + \mathbf{y} = 0, \quad (9.32)$$

which we can then solve for \mathbf{x}' in

$$\mathbf{A}^{(n-1) \times (n-1)} \frac{1}{x_n} \mathbf{x}' = -\mathbf{y}, \quad (9.33)$$

then normalize. The rank of a matrix is the maximum number of independent rows or columns. The implicit pivoting in lower–upper decomposition forces the smallest diagonal elements to the bottom of the matrix. We can then determine the rank by counting the number of non-zero diagonal elements.

9.6 The Stark effect

9.6.1 Theory

We describe a simple Coriolis-coupled top treatment of an asymmetric top Rydberg molecule subject to electric or magnetic fields. Table 9.2 lists some useful quantities. The Hamiltonian is

$$\mathcal{H} = \text{IP} + \mathcal{H}^{\text{rot}} + \sum_{\alpha} \langle i|\alpha\rangle \mathcal{H}^{\text{el}} \langle \alpha|j\rangle + \mathcal{H}^{\text{Zeeman}} + \mathcal{H}^{\text{Stark}}. \quad (9.34)$$

Table 9.3 lists the rotational and electronic matrix elements.

(i) For core-penetrating s, p and d orbitals, we take the quantum defects in the equation

$$\mathcal{H}^{\text{el}} = \frac{-\text{Ry}}{(n - \mu_{\alpha})^2}. \quad (9.35)$$

(ii) For orbitals with $\ell \geq 3$, we assume that the quantum defects are best treated by a perturbative molecular polarization or long-range force model.

Table 9.2: We express magnetic field strengths in T, electric fields in V cm⁻¹, and energies in cm⁻¹. These are the necessary conversion factors.

Effect	ν -dependence	Scaling
Linear Zeeman	—	0.942 cm ⁻¹ T ⁻¹
Quadratic Zeeman	ν^4	4.002×10^{-6} cm ⁻¹ T ⁻²
Stark effect	ν^2	1.129×10^{-3} V

Table 9.3: Comparison of Coriolis-coupled asymmetric top models. The rotational Hamiltonians include Watson-type distortion constants (not shown).

	This work	Gilbert <i>et al.</i> [63]
\mathcal{H}^{rot}	$A^+ N_a^{+2} + B^+ N_b^{+2} + C^+ N_c^{+2}$	$AT + \frac{1}{2}B(S - T - W)$ $+ \frac{1}{2}C(S - T + W)$
\mathcal{H}^{el}	$\sum_{\alpha} \langle i \alpha \rangle [-Ry/(n - \mu_{\alpha})^2] \langle \alpha j \rangle$ ($\ell < 3$) $\sum_{\alpha} \langle i \alpha \rangle H_{\alpha}^{\text{LRFM}} \langle \alpha j \rangle$ ($\ell \geq 3$)	X_{α}

These case (b) matrix elements are converted into case (d) by a frame transformation obtained by Child and Jungen [32] using standard angular momentum algebra. We assume that the total angular momentum J is a good quantum number in the body-fixed frame, but that this restriction is lifted by the Zeeman and Stark effects. Table 9.3 compares this Hund's case (d) model with the Hund's case (b) model used in Gilbert *et al.* [63].

A similar approach has been applied to alkali metal atoms [51], Rydberg states of xenon [135], molecular hydrogen [136], and most recently by Goodgame *et al.* [126] to Rydberg states of nitric oxide. The extra degrees of freedom in the quantum numbers K_a^+ and K_c^+ make the asymmetric top problem intrinsically more complicated.

The Zeeman effect Hamiltonian is

$$\begin{aligned}\mathcal{H}^{\text{Zeeman}} &= \alpha \ell_z B_z + \frac{1}{8} \alpha^2 B_z^2 r^2 \sin^2 \theta \\ &= \alpha \ell_z B_z + \frac{1}{24} \alpha^2 B_z^2 r^2 (2 - C_{20}).\end{aligned}\tag{9.36}$$

Only M_J and the parity of J remain good quantum numbers. From the size of the Bohr magneton, $2.5426 \times 10^{-4} \text{cm}^{-1} \text{T}^{-1}$, we see that the effect of the N_z^+ operator on a Rydberg molecule will be vanishingly small for the fields in a magnetic bottle spectrometer.

For the Stark effect Hamiltonian

$$\mathcal{H}^{\text{Stark}} = FrC_{10},\tag{9.37}$$

the selection rules $\Delta J = 0, \pm 1$, $\Delta N^+ = \Delta M_J = 0$ and $\Delta \ell = \pm 1$ apply. The perturbation is diagonal in n in the absence of a quantum defect.

In the cases listed above, M_J is a good quantum number. After Wigner–Eckart reduction, the geometric parts of the matrix elements for the linear Zeeman and Stark Hamiltonians imply a selection rule of $\Delta M_J = \pm 1$, and those for the quadratic Zeeman effect $\Delta M_J = 0, \pm 2$.

We follow the convention in Edmonds [137] and Zare [73] instead of Brink and Satchler [61]. The treatment is based on Knight and Wang [135].

From the Wigner–Eckart theorem the space-fixed rigid rotor case (d)

matrix elements of the spherical harmonic C_{kq} are

$$\langle i' | C_{kq} | i \rangle = (-1)^{J-M_J} \begin{pmatrix} J & k & J' \\ -M_J & q & M'_J \end{pmatrix} \langle N^{+'} \ell' J' || \mathbf{C}^k || N^+ \ell J \rangle, \quad (9.38)$$

where

$$\begin{aligned} \langle N^{+'} \ell' J' || \mathbf{C}^k || N^+ \ell J \rangle &= \delta_{N^+ N^{+'}} (-1)^{\ell+N^++J'+k} \sqrt{(2J'+1)(2J+1)} \\ &\times \begin{Bmatrix} \ell & J & N^+ \\ J' & \ell & k \end{Bmatrix} \langle \ell' || \mathbf{C}^k || \ell \rangle, \end{aligned} \quad (9.39)$$

and

$$\langle \ell || \mathbf{C}^k || \ell' \rangle = \sqrt{(2\ell+1)(2\ell'+1)} (-1)^\ell \begin{pmatrix} \ell & k & \ell' \\ 0 & 0 & 0 \end{pmatrix}. \quad (9.40)$$

9.6.2 Results

Fig. 9.1 shows a preliminary calculation for $n = 6$. The approximations include the neglect of quantum defects in the Stark matrix elements, truncating the basis set at $J = 2$ and $\ell = 5$, and neglecting the contributions of states with $n \neq 6$ apart from the 7s and 7p, with which we replace the 6s and 6p states (see Table 9.4). We see a graceful downward slope in the the levels observed in Child and Glab [36] interrupted by avoided crossings, some of which are very small and are only obvious on the map because of the presentation. In the case of the hydrogen atom, crossings are allowed

Figure 9.1: Simple $n = 6$ Coriolis-coupled top calculation for $M_J = 0$. The levels observed in Child and Glab's $J' = 1 \leftarrow 0_{00}$ spectra are marked in solid lines; the rest in dashed.

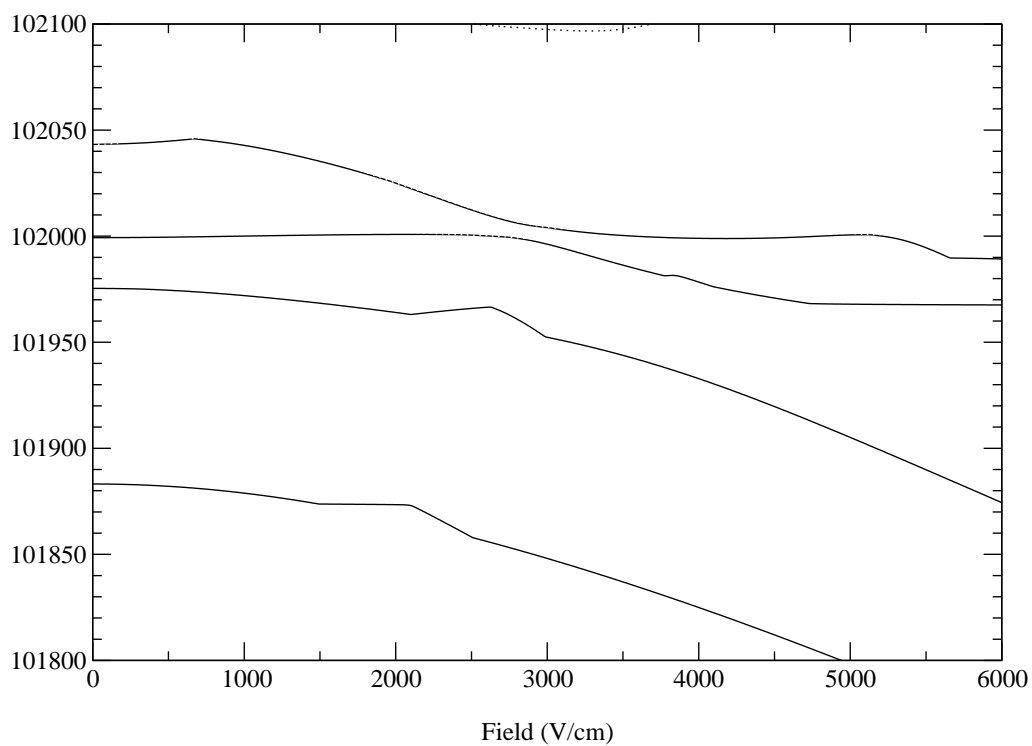


Table 9.4: States and zero-field energies (E_0) used in simple Stark-effect calculation (Fig. 9.1). Bold states are those in ref. [36]. Case (d) labels listed only for $\ell = 0$ and $\ell \geq 3$.

E_0/cm^{-1}	$n\ell$	J'	Case (d) label	E_0/cm^{-1}	$n\ell$	J'	Case (d) label
101780	7s	2	1 ₁₁	102011	6g	2	2 ₁₁
101874	6d	2	—	102043	6f	1	2₂₀
101883	6d	1	—	102043	6f	2	2 ₂₀
101919	6d	0	—	102048	6g	2	3 ₁₃
101952	7p	1	—	102057	6g	1	3 ₁₃
101975	6f	1	2₀₂	102058	6d	2	—
101975	6f	2	2 ₀₂	102065	7p	2	—
101988	6d	2	—	102093	6d	2	—
101999	6d	1	—	102109	6f	0	3 ₂₂

because the Runge–Lenz vector is a classical constant of the motion and a good quantum number.

The Wigner–Eckart theorem places no selection rules on K_a^+ and K_c^+ . Were the Stark effect perfectly diagonal in the core states, as in nitric oxide, the selection rules on p and p^* would forbid it altogether.

9.7 Full long-range-force model nf reactance matrix for water

These reactance matrix elements are calculated in the ‘dipole’ basis for the asymmetric top. The elements are listed in the order (000), (010), (020), (100), (110), (120), (200), (210), (220).

f sigma

0.09953	-0.00186	-0.00033	-0.00153	0.00043	0.00004	0.00010	-0.00004	0.00000
-0.00186	0.09967	-0.00254	-0.00012	0.00147	0.00055	-0.00004	-0.00006	-0.00003
-0.00033	-0.00254	0.09854	0.00008	0.00042	0.00175	0.00006	0.00002	-0.00007
-0.00153	-0.00012	0.00008	0.09980	0.00190	0.00024	0.00174	-0.00063	-0.00006
0.00043	0.00147	0.00042	0.00190	0.09982	-0.00266	-0.00004	0.00160	0.00070
0.00004	0.00055	0.00175	0.00024	-0.00266	0.09832	0.00000	0.00011	0.00201
0.00010	-0.00004	0.00006	0.00174	-0.00004	0.00000	0.09818	0.00247	0.00024
-0.00004	-0.00006	0.00002	-0.00063	0.00160	0.00011	0.00247	0.09781	-0.00305
0.00000	-0.00003	-0.00007	-0.00006	0.00070	0.00201	0.00024	-0.00305	0.09457

f phi plus/minus

-0.09261	0.00193	0.00085	0.00151	-0.00058	-0.00010	-0.00009	0.00006	0.00001
0.00193	-0.09202	0.00234	0.00028	-0.00145	-0.00068	0.00004	0.00005	0.00004
0.00085	0.00234	-0.09023	-0.00020	-0.00066	-0.00183	-0.00005	-0.00002	0.00008
0.00151	0.00028	-0.00020	-0.09287	-0.00191	-0.00077	-0.00170	0.00079	0.00013
-0.00058	-0.00145	-0.00066	-0.00191	-0.09213	0.00243	0.00022	-0.00156	-0.00087
-0.00010	-0.00068	-0.00183	-0.00077	0.00243	-0.08999	-0.00010	-0.00035	-0.00212
-0.00009	0.00004	-0.00005	-0.00170	0.00022	-0.00010	-0.09128	-0.00254	-0.00082
0.00006	0.00005	-0.00002	0.00079	-0.00156	-0.00035	-0.00254	-0.09011	0.00308
0.00001	0.00004	0.00008	0.00013	-0.00087	-0.00212	-0.00082	0.00308	-0.08612

f pi minus

0.13179	0.01228	-0.00114	0.00099	0.00087	-0.00013	-0.00005	0.00009	-0.00001
0.01228	0.13603	-0.01749	0.00097	-0.00075	-0.00124	-0.00006	0.00000	-0.00005
-0.00114	-0.01749	0.13125	-0.00014	-0.00022	-0.00136	0.00003	-0.00002	-0.00005
0.00099	0.00097	-0.00014	0.13225	-0.01235	0.00114	0.00085	-0.00102	0.00006
0.00087	-0.00075	-0.00022	-0.01235	0.13651	-0.01746	-0.00032	-0.00054	-0.00113
-0.00013	-0.00124	-0.00136	0.00114	-0.01746	0.13042	0.00023	0.00032	-0.00184
-0.00005	-0.00006	0.00003	0.00085	-0.00032	0.00023	0.13430	0.01375	-0.00146
0.00009	0.00000	-0.00002	-0.00102	-0.00054	0.00032	0.01375	0.13658	-0.01649
-0.00001	-0.00005	-0.00005	0.00006	-0.00113	-0.00184	-0.00146	-0.01649	0.12328

f pi plus

0.02490	0.00919	-0.00148	-0.00139	-0.00022	0.00017	0.00010	0.00002	-0.00001
0.00919	0.02116	0.01323	-0.00111	0.00152	-0.00041	-0.00001	-0.00009	0.00001
-0.00148	0.01323	0.02399	0.00023	0.00036	0.00133	0.00007	0.00005	-0.00006
-0.00139	-0.00111	0.00023	0.02486	-0.00919	0.00134	0.00185	0.00006	-0.00013
-0.00022	0.00152	0.00036	-0.00919	0.02091	0.01304	-0.00035	0.00194	-0.00007
0.00017	-0.00041	0.00133	0.00134	0.01304	0.02449	0.00021	0.00043	0.00127
0.00010	-0.00001	0.00007	0.00185	-0.00035	0.00021	0.02035	-0.00968	0.00163
0.00002	-0.00009	0.00005	0.00006	0.00194	0.00043	-0.00968	0.01769	0.01156
-0.00001	0.00001	-0.00006	-0.00013	-0.00007	0.00127	0.00163	0.01156	0.02583

f delta plus/minus

0.01409	-0.00017	0.00019	-0.00018	-0.00002	-0.00002	0.00001	0.00000	0.00000
-0.00017	0.01443	-0.00037	0.00006	0.00017	0.00000	-0.00001	-0.00001	0.00000
0.00019	-0.00037	0.01460	-0.00005	-0.00006	0.00015	0.00001	0.00001	0.00000
-0.00018	0.00006	-0.00005	0.01413	0.00020	-0.00020	0.00021	0.00000	0.00002
-0.00002	0.00017	-0.00006	0.00020	0.01446	-0.00039	0.00007	0.00019	0.00000
-0.00002	0.00000	0.00015	-0.00020	-0.00039	0.01459	-0.00004	-0.00009	0.00017
0.00001	-0.00001	0.00001	0.00021	0.00007	-0.00004	0.01393	0.00024	-0.00023
0.00000	-0.00001	0.00001	0.00000	0.00019	-0.00009	0.00024	0.01425	-0.00032
0.00000	0.00000	0.00000	0.00002	0.00000	0.00017	-0.00023	-0.00032	0.01423

f phi--pi coupling

```
-0.01154 0.00241 -0.00020 0.00003 -0.00016 0.00004 0.00000 0.00002 0.00000
0.00241 -0.01231 0.00338 -0.00019 0.00003 -0.00023 0.00001 -0.00001 0.00001
-0.00020 0.00338 -0.01134 0.00000 -0.00006 -0.00006 0.00000 0.00001 0.00000
0.00003 -0.00019 0.00000 -0.01161 -0.00241 0.00018 0.00003 0.00018 -0.00003
-0.00016 0.00003 -0.00006 -0.00241 -0.01238 0.00335 -0.00004 0.00010 -0.00020
0.00004 -0.00023 -0.00006 0.00018 0.00335 -0.01118 0.00001 0.00002 -0.00013
0.00000 0.00001 0.00000 0.00003 -0.00004 0.00001 -0.01224 -0.00266 0.00026
0.00002 -0.00001 0.00001 0.00018 0.00010 0.00002 -0.00266 -0.01267 0.00316
0.00000 0.00001 0.00000 -0.00003 -0.00020 -0.00013 0.00026 0.00316 -0.01013
```

f sigma--delta coupling

```
-0.01630 0.00340 -0.00028 0.00004 -0.00023 0.00005 0.00000 0.00003 -0.00001
0.00340 -0.01738 0.00477 -0.00027 0.00005 -0.00033 0.00001 -0.00002 0.00002
-0.00028 0.00477 -0.01602 0.00000 -0.00008 -0.00008 0.00000 0.00001 0.00000
0.00004 -0.00027 0.00000 -0.01639 -0.00340 0.00025 0.00004 0.00025 -0.00004
-0.00023 0.00005 -0.00008 -0.00340 -0.01749 0.00474 -0.00005 0.00015 -0.00028
0.00005 -0.00033 -0.00008 0.00025 0.00474 -0.01579 0.00002 0.00003 -0.00019
0.00000 0.00001 0.00000 0.00004 -0.00005 0.00002 -0.01728 -0.00376 0.00037
0.00003 -0.00002 0.00001 0.00025 0.00015 0.00003 -0.00376 -0.01789 0.00447
-0.00001 0.00002 0.00000 -0.00004 -0.00028 -0.00019 0.00037 0.00447 -0.01431
```

Bibliography

- [1] M. Born and J. R. Oppenheimer, *Ann. Phys. (Leipzig)*, 1927, **84**, 457.
- [2] J. M. Raimond, M. Brune, and S. Haroche, *Rev. Mod. Phys.*, 2001, **73**, 1565.
- [3] T. Uzer, E. A. Lee, D. Farrelly, and A. F. Brunello, *Contemp. Phys.*, 2000, **41**, 1.
- [4] C. H. Greene, A. S. Dickinson, and H. R. Sadeghpour, *Phys. Rev. Lett.*, 2000, **85**, 2458.
- [5] B. E. Granger, E. L. Hamilton, and C. H. Greene, *Phys. Rev. A*, 2001, **64**, 042508.
- [6] C. Sandorfy and L. S. Lussier, in *Photophysics and Photochemistry in the Vacuum Ultraviolet, NATO ASI Series C*, ed. S. P. McGlynn, G. L. Findley and R. H. Huebner, D. Reidel, Dordrecht, The Netherlands, 1985.

- [7] R. S. Mulliken, *J. Am. Chem. Soc.*, 1964, **86**, 3183.
- [8] R. S. Mulliken, *Acc. Chem. Res.*, 1976, **9**, 7.
- [9] T. H. Dunning, *J. Chem. Phys.*, 1971, **55**, 716.
- [10] G. Herzberg, *Molecular Spectra and Molecular Structure, I. Spectra of Diatomic Molecules*, Van Nostrand, Princeton, NJ, 1950.
- [11] D. R. Hartree, *Proc. Cambridge Philos. Soc.*, 1928, **24**, 89.
- [12] D. R. Hartree, *Proc. Cambridge Philos. Soc.*, 1928, **24**, 111.
- [13] D. R. Hartree, *Proc. Cambridge Philos. Soc.*, 1928, **24**, 426.
- [14] D. R. Hartree, *Proc. Cambridge Philos. Soc.*, 1929, **25**, 310.
- [15] J. Hargreaves, *Proc. Cambridge Philos. Soc.*, 1929, **25**, 315.
- [16] D. R. Bates and A. Damgaard, *Philos. Trans. R. Soc. London, Ser. A*, 1949, **242**, 101.
- [17] R. S. Mulliken, *J. Am. Chem. Soc.*, 1966, **88**, 1849.
- [18] R. S. Mulliken, *J. Am. Chem. Soc.*, 1969, **91**, 4615.
- [19] M. J. Seaton, *Rep. Prog. Phys.*, 1983, **46**, 167.
- [20] U. Fano, *Phys. Rev. A*, 1970, **2**, 353.

- [21] D. A. Harmin, *Phys. Rev. A*, 1981, **24**, 2491.
- [22] D. A. Harmin, *Phys. Rev. A*, 1982, **26**, 2656.
- [23] D. A. Harmin, *Phys. Rev. A*, 1984, **30**, 2413.
- [24] K. Sakimoto, *J. Phys. B: At. Mol. Phys.*, 1986, **19**, 3011.
- [25] K. Sakimoto, *J. Phys. B: At. Mol. Phys.*, 1989, **22**, 2727.
- [26] T. S. Monteiro and K. T. Taylor, *J. Phys. B: At. Mol. Opt. Phys.*, 1989, **22**, L191.
- [27] T. S. Monteiro and K. T. Taylor, *J. Phys. B: At. Mol. Opt. Phys.*, 1990, **23**, 427.
- [28] A. Giusti, *J. Phys. B: At. Mol. Phys.*, 1980, **13**, 3867.
- [29] A. Giusti-Suzor and Ch. Jungen, *J. Chem. Phys.*, 1984, **80**, 986.
- [30] S. C. Ross and Ch. Jungen, *Phys. Rev. A*, 1994, **49**, 4364.
- [31] Ch. Jungen and S. C. Ross, *Phys. Rev. A*, 1997, **55**, R2503.
- [32] M. S. Child and Ch. Jungen, *J. Chem. Phys.*, 1990, **93**, 7756.
- [33] C. H. Greene and Ch. Jungen, *Adv. At. Mol. Phys.*, 1985, **21**, 51.
- [34] Ch. Jungen and S. T. Pratt, *J. Chem. Phys.*, 1997, **106**, 9529.

- [35] X. Tong, S. Ullrich, C. E. H. Dessent, and K. Müller-Dethlefs, *Phys. Chem. Chem. Phys.*, 2002, **4**, 3578.
- [36] M. S. Child and W. L. Glab, *J. Chem. Phys.*, 2000, **112**, 3754.
- [37] Ch. Jungen and E. Miescher, *Can. J. Phys.*, 1969, **47**, 1769.
- [38] H. Dickinson, S. R. Mackenzie, and T. P. Softley, *Phys. Chem. Chem. Phys.*, 2000, **2**, 4669.
- [39] R. A. L. Smith, J. R. R. Verlet, E. D. Boléat, V. G. Stavros, and H. H. Fielding, *Faraday Discuss.*, 2000, **115**, 63.
- [40] M. Abramowitz and I. A. Stegun, *Handbook of Mathematical Functions*, Dover, New York, 1972.
- [41] C. H. Greene, A. R. P. Rau, and U. Fano, *Phys. Rev. A*, 1982, **26**, 2441.
- [42] J. Hargreaves, *Proc. Cambridge Philos. Soc.*, 1929, **25**, 75.
- [43] A. C. Allison and A. Dalgarno, *J. Chem. Phys.*, 1971, **55**, 4342.
- [44] G. Simons, *J. Chem. Phys.*, 1974, **60**, 645.
- [45] I. Martín and G. Simons, *J. Chem. Phys.*, 1975, **62**, 4799.
- [46] I. Martín and G. Simons, *Mol. Phys.*, 1976, **32**, 1017.

- [47] B. A. Zon, *Phys. Lett. A*, 1995, **203**, 373.
- [48] B. A. Zon, *Sov. Phys. JETP*, 1992, **75**, 19.
- [49] V. E. Chernov, D. L. Dorofeev, and B. A. Zon, *J. Phys. B: At. Mol. Opt. Phys.*, 1999, **32**, 967.
- [50] C. Greene, U. Fano, and G. Strinati, *Phys. Rev. A*, 1979, **19**, 1485.
- [51] M. L. Zimmerman, M. G. Littman, M. M. Kash, and D. Kleppner, *Phys. Rev. A*, 1979, **20**, 2251.
- [52] R. D. Gilbert and M. S. Child, *Chem. Phys. Lett.*, 1991, **187**, 153.
- [53] M. Bixon and J. Jortner, *Mol. Phys.*, 1996, **89**, 373.
- [54] B. Numerov, *Publ. Obs. Central Astrophys. Russ.*, 1933, **2**, 188.
- [55] J. W. Cooley, *Math. Comput.*, 1961, **15**, 363.
- [56] J. K. Cashion, *J. Chem. Phys.*, 1963, **39**, 1872.
- [57] R. J. Le Roy, *LEVEL 7.4: A Computer Program for Solving the Radial Schrödinger Equation for Bound and Quasibound Levels*, University of Waterloo Chemical Physics Research Report CP-642R³, University of Waterloo, 2001.
- [58] Ch. Jungen, private communication, 2001.

- [59] K. Bockasten, *Phys. Rev. A.*, 1974, **9**, 1087.
- [60] P. F. O'Mahony and K. T. Taylor, *Phys. Rev. Lett.*, 1986, **57**, 2931.
- [61] D. M. Brink and G. R. Satchler, *Angular Momentum*, Oxford, 2nd ed., 1968.
- [62] M. J. Vrakking, Y. T. Lee, R. D. Gilbert, and M. S. Child, *J. Chem. Phys.*, 1993, **98**, 1902.
- [63] R. D. Gilbert, M. S. Child, and J. W. C. Johns, *Mol. Phys.*, 1991, **74**, 473.
- [64] P. R. Bunker and P. Jensen, *Molecular Symmetry and Spectroscopy*, National Research Council of Canada, Ottawa, 2nd ed., 1998.
- [65] D. Dill, *Phys. Rev. A*, 1972, **6**, 160.
- [66] R. S. Berry, *J. Chem. Phys.*, 1966, **45**, 1228.
- [67] G. Herzberg and Ch. Jungen, *J. Mol. Spectrosc.*, 1972, **41**, 425.
- [68] I. Waller, *Z. Phys.*, 1926, **38**, 635.
- [69] E. E. Eyler and F. M. Pipkin, *Phys. Rev. A*, 1983, **27**, 2462.
- [70] J. K. G. Watson, *Mol. Phys.*, 1994, **81**, 277.

- [71] E. S. Chang, J. Li, J. Zhang, C.-C. Tsai, J. Bahns, and W. C. Stwalley, *J. Chem. Phys.*, 1999, **111**, 6247.
- [72] A. J. Stone, *The Theory of Intermolecular Forces*, Clarendon Press, Oxford, 1996.
- [73] R. N. Zare, *Angular Momentum*, Wiley, New York, 1988.
- [74] L. C. Biedenharn and J. D. Louck, *The Racah–Wigner Algebra in Quantum Theory*, Addison-Wesley, Reading, MA, 1981.
- [75] U. Fano, *Phys. Rev. A*, 1981, **24**, 619.
- [76] Ch. Jungen, *J. Chem. Phys.*, 1970, **53**, 4168.
- [77] M. N. R. Ashfold, J. M. Bayley, and R. N. Dixon, *Chem. Phys.*, 1984, **84**, 35.
- [78] C. A. Mayhew *The High Resolution Spectra of the Group VI Dihydrides and Deuterides in the Vacuum Ultraviolet*, PhD thesis, Imperial College, University of London, 1984.
- [79] M.-T. Lee, K. Wang, V. McKoy, and L. E. Machado, *J. Chem. Phys.*, 1992, **97**, 3905.
- [80] W. H. Press, B. P. Flannery, S. A. Teukolsky, and W. T. Vetterling, *Numerical Recipes in FORTRAN*, Cambridge University Press, 1986.

- [81] M. Jacobson PhD thesis, Massachusetts Institute of Technology, 1999.
- [82] A. D. Becke, *Phys. Rev. A*, 1988, **38**, 3098.
- [83] A. D. Becke, *J. Chem. Phys.*, 1993, **98**, 5648.
- [84] C. Lee, W. Yang, and R. G. Parr, *Phys. Rev. B*, 1988, **37**, 785.
- [85] S. H. Vosko, L. Wilk, and M. Nusair, *Can. J. Phys.*, 1980, **58**, 1200.
- [86] M. J. Frisch, G. W. Trucks, H. B. Schlegel, P. M. W. Gill, B. G. Johnson, M. A. Robb, J. R. Cheeseman, T. Keith, G. A. Petersson, J. A. Montgomery, K. Raghavachari, M. A. Al-Laham, V. G. Zakrzewski, J. V. Ortiz, J. B. Foresman, J. Cioslowski, B. B. Stefanov, A. Nanayakkara, M. Challacombe, C. Y. Peng, P. Y. Ayala, W. Chen, M. W. Wong, J. L. Andres, E. S. Replogle, R. Gomperts, R. L. Martin, D. J. Fox, J. S. Binkley, D. J. Defrees, J. Baker, J. P. Stewart, M. Head-Gordon, C. Gonzalez, and J. A. Pople, *Gaussian 94, Revision D.4*, Gaussian, Inc., Pittsburgh PA, 1995.
- [87] W. L. Glab, *J. Chem. Phys.*, 2002, **117**, 9316.
- [88] R. G. Tonkyn, R. Wiedmann, E. R. Grant, and M. G. White, *J. Chem. Phys.*, 1991, **95**, 7033.

- [89] H. Dickinson, D. Rolland, and T. P. Softley, *Philos. Trans. R. Soc. London, Ser. A*, 1997, **355**, 1585.
- [90] W. A. Chupka and E. R. Grant, *J. Phys. Chem. A*, 1999, **103**, 6127.
- [91] W. A. Chupka, *J. Chem. Phys.*, 1993, **98**, 4520.
- [92] H. Dickinson, D. Rolland, and T. P. Softley, *J. Phys. Chem. A*, 2001, **105**, 5590.
- [93] G. Theodorakopoulos, I. D. Petsalakis, and M. S. Child, *J. Phys. B: At. Mol. Opt. Phys.*, 1996, **29**, 4543.
- [94] M. N. R. Ashfold, J. M. Bayley, and R. N. Dixon, *Can. J. Phys.*, 1984, **63**, 1806.
- [95] M. N. R. Ashfold and J. M. Bayley, *J. Chem. Soc., Faraday Trans.*, 1984, **86**, 213.
- [96] E. Ishiguro, M. Sasanuma, H. Masuko, Y. Morioda, and M. Nakamura, *J. Phys. B: At. Mol. Phys.*, 1978, **11**, 993.
- [97] M. S. Child, *Philos. Trans. R. Soc. London, Ser. A*, 1997, **355**, 1623.
- [98] S. Bell, *J. Mol. Spectrosc.*, 1965, **16**, 205.
- [99] M. J. J. Vrakking and Y. T. Lee, *J. Chem. Phys.*, 1995, **102**, 8818.

- [100] F. X. Campos, Y. Jiang, and E. R. Grant, *J. Chem. Phys.*, 1990, **93**, 2308.
- [101] F. X. Campos, Y. Jiang, and E. R. Grant, *J. Chem. Phys.*, 1990, **93**, 7731.
- [102] H. Matsui, J. M. Behm, and E. R. Grant, *J. Phys. Chem. A*, 1997, **101**, 6717.
- [103] E. E. Mayer and E. R. Grant, *J. Chem. Phys.*, 1995, **103**, 10513.
- [104] E. E. Mayer, E. Zückerman, I. Zhang, H. G. Hedderich, J. Behm, and E. R. Grant, *Philos. Trans. R. Soc. London, Ser. A*, 1997, **355**, 1569.
- [105] E. E. Mayer, H. G. Hedderich, and E. R. Grant, *J. Chem. Phys.*, 1998, **108**, 1886.
- [106] E. E. Mayer, H. G. Hedderich, and E. R. Grant, *J. Chem. Phys.*, 1998, **108**, 8429.
- [107] J. D. Robinson, R. J. Foltynowicz, and E. R. Grant, *J. Chem. Phys.*, 2000, **112**.
- [108] S. T. Pratt, *J. Chem. Phys.*, 2002, **117**, 1055.
- [109] W. L. Glab, M. S. Child, and S. T. Pratt, *J. Chem. Phys.*, 1998, **109**, 3062.

- [110] B. Weis, S. Carter, P. Rosmus, H.-J. Werner, and P. J. Knowles, *J. Chem. Phys.*, 1989, **91**, 2818.
- [111] M. Brommer, B. Weis, B. Follmeg, P. Rosmus, S. Carter, N. C. Handy, H.-J. Werner, and P. J. Knowles, *J. Chem. Phys.*, 1993, **98**, 5222.
- [112] S. Carter, N. C. Handy, and B. T. Sutcliffe, *Mol. Phys.*, 1983, **49**, 745.
- [113] B. M. Dinelli, M. W. Crofton, and T. Oka, *J. Mol. Spectrosc.*, 1988, **127**, 1.
- [114] F. W. Birss, *Mol. Phys.*, 1976, **31**, 491.
- [115] H. Park, D. J. Leahy, and R. N. Zare, *Phys. Rev. Lett.*, 1996, **76**, 1591.
- [116] H. Park and R. N. Zare, *J. Chem. Phys.*, 1997, **106**, 2239.
- [117] S. T. Pratt, *J. Chem. Phys.*, 1998, **108**, 7131.
- [118] ed. K. Przibram, *Letters on Wave Mechanics*, Philosophical Library, New York, 1967.
- [119] E. Schrödinger, *Naturwissenschaften*, 1926, **14**, 664.
- [120] J. Parker and C. R. Stroud, Jr., *Phys. Rev. Lett.*, 1985, **56**, 716.
- [121] I. Sh. Averbukh and N. F. Perelman, *Phys. Lett. A*, 1989, **139**, 449.
- [122] G. Alber, H. Ritsch, and P. Zoller, *Phys. Rev. A*, 1986, **34**, 1058.

- [123] L. D. Noordam, D. I. Duncan, and T. F. Gallagher, *Phys. Rev. A*, 1992, **45**, 4734.
- [124] I. Mills, T. Cvitaš, K. Homann, N. Kallay, and K. Kuchitsu, *Quantities, Units and Symbols in Physical Chemistry*, Blackwell Science, Oxford, second ed., 1993.
- [125] N. F. Ramsey, *Phys. Rev.*, 1949, **76**, 996.
- [126] A. L. Goodgame, H. Dickinson, S. R. Mackenzie, and T. P. Softley, *J. Chem. Phys.*, 2002, **116**, 4922.
- [127] P. Labastie, M. C. Bordas, B. Tribollet, and M. Broyer, *Phys. Rev. Lett.*, 1984, **52**, 1681.
- [128] S. Fredin, D. Gauyacq, M. Horani, Ch. Jungen, and G. Lefevre, *Mol. Phys.*, 1987, **60**, 825.
- [129] J. Wals, H. H. Fielding, and H. B. van Linden van den Heuvell, *Phys. Scr., T*, 1995, **58**, 62.
- [130] T. C. Weinacht, J. Ahn, and P. H. Bucksbaum, *Phys. Rev. Lett.*, 1998, **80**, 5508.
- [131] K. Cowtan, <http://www.yorvic.york.ac.uk/~cowtan/fourier/coeff.html>, University of York, accessed 23rd September 2001.

- [132] R. A. L. Smith, V. G. Stavros, J. R. R. Verlet, H. H. Fielding, D. Townsend, and T. P. Softley, *J. Chem. Phys.*, 2003, **119**, in press.
- [133] S. L. Price, A. J. Stone, and M. Alderton, *Mol. Phys.*, 1984, **52**, 987.
- [134] R. J. Drachman, *Phys. Rev. A*, 1982, **26**, 1228.
- [135] R. D. Knight and L. G. Wang, *Phys. Rev. A*, 1985, **32**, 896.
- [136] H. H. Fielding and T. P. Softley, *Chem. Phys. Lett.*, 1991, **185**, 199.
- [137] A. R. Edmonds, *Angular Momentum in Quantum Mechanics*, Princeton University Press, Princeton, New Jersey, 1974.